Symmetry Breaking Effects in Low-Dimensional Quantum Systems

SYMMETRY BREAKING EFFECTS IN LOW-DIMENSIONAL QUANTUM SYSTEMS

A Dissertation Presented

by

KE WANG

Submitted to the Graduate School of the
University of Massachusetts Amherst in partial fulfillment
of the requirements for the degree of

DOCTOR OF PHILOSOPHY

September 2022

Department of Physics

SYMMETRY BREAKING EFFECTS IN LOW-DIMENSIONAL QUANTUM SYSTEMS

A Dissertation Presented

by

KE WANG

Approved as to style and content by:

Tigran Sedrakyan, Chair

Nikolay Prokof'ev, Member

Boris Svistunov, Member

Owen Gwilliam, Member

Anthony Dinsmore, Department Chair
Department of Physics

ABSTRACT

SYMMETRY BREAKING EFFECTS IN LOW-DIMENSIONAL QUANTUM SYSTEMS

SEPTEMBER 2022

KE WANG

Ph.D., UNIVERSITY OF MASSACHUSETTS AMHERST

Directed by: Professor Tigran Sedrakyan

Quantum criticality in low-dimensional quantum systems is known to host exotic behaviors. In quantum one-dimension (1D), the emerging conformal group contains infinite generators, and conformal techniques, e.g., operator product expansion, give accurate and universal descriptions of underlying systems. In quantum two-dimension (2D), the electronic interaction causes singular corrections to Fermi-liquids characteristics. Meanwhile, the Dirac fermions in topological 2D materials can greatly enrich emerging phenomena. In this thesis, we study the symmetry-breaking effects of low-dimensional quantum criticality. In 1D, we consider two cases: time-reversal symmetry (TRS) breaking in the Majorana conformal field theory (CFT) and the absence of conformal symmetry in the $z = 2$ Lifshitz criticality. In both cases, universal features of quantum criticality exhibit exotic behaviors, e.g., the finite-size amplitude and entanglement entropy. In 2D, we study the effect of a weak perpendicular magnetic field on the doped graphene. We establish the chiral symmetry breaking mechanism induced by the field and explore its many-body consequences, e.g., thermodynamics and magnetoresistance.

ACKNOWLEDGEMENTS

First and foremost, I would like to thank my supervisor, Prof. Tigran Sedrakyan, for his help and support. During my Ph.D., he gave excellent guidance about how I shall enter into the research areas and provided crucial suggestions for my academic career. Without his support, the thesis would have been impossible to accomplish. I want to thank Prof. Mikhail E. Raikh from the University of Utah for the amazing collaboration and discussions with him. I also appreciate helpful suggestions from Prof. Boris Svistunov, the academic advisor in my early Ph.D. I have learned and benefited significantly from taking classes and discussing with Prof. Nikolay Prokof'ev and Prof. Romain Vasseur. I also appreciate insightful discussions and valuable suggestions from my colleagues: Jin Zhang, Zhiyuan Yao, Kun Chen, Utkarsh Agrawal, and Javier Lopez Piqueres.

I am fortunate to make many great friends in Amherst, especially Guanghui Zhou and Christopher Amey. In the first and second years of graduate-student life, it is enjoyable to chat about physics/non-physics and have food with Guanghui. He also gave me a lot of support when I bought a car and applied for a postdoc position. Christopher, who was my officemate for two years, gave many valuable suggestions and taught me about American culture. Finally, I would like to thank my good friends from the University of Massachusetts: Xiansheng Cai, Tao Wang, Mingzhu Cui, Yueh-Chun Wu, Reddy Nareddy-Vahini, and Hansveer Singh.

Finally, I acknowledge all support from my family. I owe most to my parents, who have been supporting my education since I was a child. I would like to thank my wife, Qiaoshan Lin, for her accompanies during my Ph.D. She always stands behind and supports me. Without their care, support and love, I cannot make it far.

TABLE OF CONTENTS

LIST OF FIGURES

Figure **Page**

INTRODUCTION

Low-dimensional quantum systems exhibit exotic behaviors and have attracted much attention in the last several decades[1, 2, 3, 4, 5, 6, 7, 8, 9]. One specialty of quantum 1D is the failure of the Fermi-Liquid theory. The failure originates from the total nesting properties of the Fermi surface and is observed by the ultraviolet and infrared divergence of perturbative Feynman diagrams. The other specialty of quantum 1D is the emerging two-dimensional conformal symmetry group. The group substantially constrains behaviors of quantum systems since the 2D conformal group contains infinite generators. Thus the symmetry analysis can give accurate and universal data describing the underlying quantum theory, e.g., via the operator product expansion (OPE) technique. The properties of quantum 2D electronic systems can be described by the non-analytical corrections to Fermi-liquid characteristics. Non-analyticities originate from the backscattering process in interacting electronic systems. The backscattering manifests itself in the $k = 2k_F$ polarization operator in quantum many-body physics, and its static component possesses a singularity, which is the discontinuity at the derivative. This discontinuity, known as the Kohn anomaly, leads to the Friedel oscillations as the signature of the Fermi surface. The singularity of the polarization operator plays an important role in renormalizing the electron-electron interaction and causes singular corrections to Fermi-liquid characteristics.

Topology plays an important role in modern condensed matter physics[10, 11, 12, 13, 14, 15, 16, 17, 18, 19, 20, 21, 22]. Back in 1980s, it was found that the topological invariant, the Chern number, describes the quantized conductance in quantum Hall effects[12]. Topology, as the global feature of physical systems, manifest itself in many

different concrete forms. The definition of an invariant is usually up to two factors: dimension and symmetry. For example, the $\mathbb{Z}_2$ Pfaffian invariant is constructed in the Kitaev chain and this invariant ensures emergence of Majorana boundary modes[14]. This is the case in one-dimension and with particle-hole symmetry. The winding number $\mathbb{Z}$ invariant is realized in the Su-Schrieffer–Heeger (SSH) model[23]. This is one dimensional situation with chiral symmetry. Other famous examples are Chern insulators[13] (two dimensions, no symmetry) and topological insulators[20] (two dimensions, time-reversal symmetry). The pioneering work of Kitaev[24] shows that all different cases of non-interacting fermions can be unified into a singe mathematical framework, algebraic K-theory[25]. In the theory, physical systems are treated as irreducible representations of Clifford algebra[26]. It uncovers the deep correlation between the dimension, symmetries and topology via Bott periodicity[27].

The interplay of topology and many-body effects greatly enriches emerging phenomena. For example, in the monolayer graphene, the Dirac fermions with the quantized Berry phase can be realized near the half-filling[28]. The fate of Coulomb interaction in the topological material is unlike in the conventional 2D Fermi liquids. There are two reasons: (1) the Fermi surface consists of discrete points instead of a continuous circle. This leads to the vanishing density of states at the Fermi surface (points). Thus the interaction is not screened and has a long-range nature[29]. (2) The interacting theory has a coupling constant $\alpha \sim 1$ instead of $1/137$ since the Fermi velocity is only around $1/100$ of the speed of light[30]. The interaction has a non-perturbative nature due to $\alpha \sim 1$ coupling constant. The interacting theory in the graphene is considered to be an example of non-Fermi liquids[31].

The exotic properties of low-dimensional systems and the emergence of new topological phenomena motivate us to study the topological phenomena in low-dimensional systems. In quantum 1D, we study exotic behaviors of the system around two types of criticalities in topological chains. One criticality is described by the bulk Majorana

CFT and the boundary Majorana modes. The other criticality is not described by CFT theory but separates two topologically different CFTs. The consideration of two types of criticalities serves as Part I of the thesis. In quantum 2D, we study the effects of a weak perpendicular magnetic field on Dirac electrons. We establish the mechanism of the semi-classical chiral symmetry breaking (CSB) induced by the magnetic field and thoroughly explore its many-body effects on Dirac electrons. The study of CSB is presented in Part II of the thesis.

The thesis is organized into five chapters. Part I consists of Chapters 1 and 2. In Chapter 1, we show that the boundary Majorana fermions and the time-reversal symmetry breaking field can change the universal amplitude $\pi/24$ of CFT in a boundary renormalization group flow. In Chapter 2, we establish the universal features of $z = 2$ Lifshitz criticality, where the conformal symmetry is absent. The second part consists of Chapters 3, 4 and 5. In Chapter 3, we establish the mechanism of chiral-symmetry breaking (CSB) and present a new form of Friedel oscillations in graphene. In Chapter 4, we explore the consequences of this symmetry breaking for the interaction effects in graphene, including quasiparticle lifetime, ballistic zero-bias anomaly, and thermodynamic characteristics of graphene. In Chapter 5, we further explore the effect of CSB on the transport properties of graphene.

PART I: SYMMETRY BREAKING EFFECTS IN TOPOLOGICAL CHAINS

CHAPTER 1

CRITICALITY IN MAJORANA CHAINS AND TIME-REVERSAL SYMMETRY BREAKING EFFECTS

The text of this chapter has been adapted from Ref [32].

1.1 Introduction

Finite-size corrections to the ground state energy in 1+1D conformal field theories[1, 2, 3] (CFT) have been shown to be universal and were studied in various systems since mid 1980s. Recently, it has been shown[33] that the finite size corrections to the ground-state energy across topological phase transitions can differentiate between different topological and topologically trivial phases. These include transitions within phases classified by the group $\mathbb{Z}$ of topological invariants (from phase characterized by topological index n to the phase characterized by index $(n-1)$), or transitions from phases with the $\mathbb{Z}$ indices and phases with $\mathbb{Z}_2$ indices. Importantly, it has been shown that the finite-size scaling function is universal for all five topological symmetry classes in 1+1D (AIII, BDI, CII, D, DIII), tabulated according to Cartan's classification of symmetric spaces[34, 14, 35, 36]

Although the fact of distinct universality of the scaling function across a continuous phase transition between phases characterized by $\mathbb{Z}$ and/or $\mathbb{Z}_2$ index classification is amazing, the question arises whether these scaling properties survive in the presence of tricriticality. Different scaling properties can be expected for example when there is a tricritical point in the phase diagram separating three different phases: a topologically ordered phase[37], a time-reversal symmetry protected topological (SPT)

phase[15, 16, 17, 18, 19, 20, 21, 22], and a trivial phase. Such a situation shows up if the transition between phases is accompanied by the time-reversal symmetry (TRS) breaking. Examples include transitions between topological phases belonging to the BDI class classified via $\mathbb{Z}$ index and the TRS broken phase belonging to the D class classified via $\mathbb{Z}_2$ index.

In this chapter, we answer this question through confining our focus on coupled 1+1D Kitaev-Majorana superconducting wires [38, 39, 40, 41, 42, 43, 44, 45] (throughout this article referred to as Majorana chains) from the abovementioned symmetry classes. The transition from a BDI phase to a D phase is characterized by a generic TRS breaking field, which we denote by B and which will be specified for all models considered in this work. The universal properties around tricriticality between BDI, D, and trivial phases are described by the low-energy excitations around the Fermi surface, which we will discuss here in detail.

For a 1+1D critical quantum system, the CFT predicts a universal finite size scaling of the ground state energy with open boundary conditions,[3]

$$E(N) = N\epsilon + b - \frac{c}{N}\frac{\pi}{24} + \mathcal{O}(N^{-2}), \tag{1.1}$$

where c is the central charge[1, 46] of the CFT, $E(N)$ is the ground state energy of the system with size N, ϵ is average bulk energy, b is the boundary energy.

Around topological quantum phase transition in $1+1$D, the CFT result Eq.(1.1) is generalized to[33]

$$E(N, m) = N\epsilon(m) + b(m) - \frac{c}{N} f(Nm) + \mathcal{O}(N^{-2}), \tag{1.2}$$

where $f(Nm)$ is shown to be a universal function of its argument for five different symmetry classes. This is achieved in the double scaling limit, when $N \to \infty$, $m \to 0$,

while $w = Nm$ is kept constant. This result is derived from $1 + 1$D Majorana field theory, which describes the critical phases of free fermion models.

While the finite-size scaling across the topological quantum phase transition is now well understood, we will show that the situation is different around the tricriticality, where there are two extra Majorana edge modes near the Fermi surface. There are two categories of states determining the low-energy sector: (i) The states described by the 1+1D massive (with the excitation gap, m) bulk Majorana field theory (MFT). (ii) A boundary Hamiltonian describing an even number of localized Majorana edge modes with localization lengths ξ. Once the TRS breaking field is introduced, it can drive the boundary RG flow[47] from the tricriticality (gapless SPT phase)[48, 49] to the criticality without edge modes (gapless trivial phase). Such non-trivial boundary effects can exhibit themselves in the scaling properties of finite size corrections to the ground state energy. This is the effect that we are going to explore here.

In this chapter, we derive the finite size scaling function around the tricriticality, which is strongly influenced by the TRS breaking field, B. We show that the result Eq.(1.2) is generalized to

$$E = N\epsilon + b - \frac{c}{N} f(Nm, \alpha\sqrt{N}B) + \mathcal{O}(N^{-2}). \tag{1.3}$$

where $E = E(N, m, B)$ is the ground state energy that now also depends on B, $c = 1/2$, and $\alpha(\xi)$ is a function of the localization length of the Majorana edge modes, ξ, at the tricriticality. The function $\alpha(\xi)$ depends on the details of the lattice model, but $\alpha(0) \equiv 1$ for all of them. The finite size scaling function $f(w, g)$ is now a function of two variables: $w = Nm$ and $g = \alpha\sqrt{N}B$. Under two simultaneous double-scaling[50] limits: a) $N \to \infty$, $m \to 0$ with $w = const$ and b) $N \to \infty$, $B \to 0$, with $g = const$, the function $f(w, g)$ is a universal function of w and g. This is the main result and will be obtained below both, analytically and numerically. We will also

discuss the implications of the new emergent scale on the numerical simulations of many-body systems with TRS breaking.

The universality of the double-scale function $f(w, g)$ is shown for a parent Hamiltonian representing a pair of coupled Majorana chains (discussed in Sect.(1.2)), with three different symmetry breaking fields B:

(i) We consider two Majorana chains coupled to each other with a complex pairing-potential $\Delta_v = \Delta_v^R + i\Delta_v^I$,[41] along the *vertical* rungs. The TRS breaking field, in this case, is identified with $B \equiv \Delta_v^I/(2t)$, where t is the nearest-neighbor hopping parameter. In this model, the function $\alpha(\xi)$ is found to be $\alpha(\xi) = \sqrt{\coth(1/2\xi)}$. The Hamiltonian of the model, its solution, along with the detailed analysis of the ground state energy is discussed in Sect.(1.3.1).

(ii) We consider coupled Majorana chains in a uniform external magnetic field[42]. The Flux can be realized by complex hopping $te^{i\theta/2}$ along the *horizontal* chains. The TRS breaking field in this case is identified with $B = \frac{1}{2}\sin(\theta/2)$. This model is analysed in Sect.(1.3.2).

(iii) We study coupled Majorana chains in the presence of a staggered magnetic flux, $\pm\theta$, threading square plaquettes of the lattice. The Flux can be realized by alternating complex hopping $t_v e^{\pm i\theta/2}$ along the *vertical* rungs. In this model, $\alpha(\xi) = \sqrt{\tanh(1/2\xi)}$. The TRS breaking field in this case is identified with $B = t_v \sin(\theta/2)/(2t)$, This model is analysed in Sect.(1.3.3).

The scaling of finite-size correction to the ground state energy in all three models under consideration is shown to obey the universal behavior determined by function $f(w, g)$. Particular cases corresponding to $w = 0$ (critical phase) and finite $w = 2$ (gapped phase) are shown in Figs. (1.1) and (1.2) respectively.

Although $f(0, 0) = \pi/24$, which directly follows from CFT calculations, the scaling function $f(0, g)$ exhibits nontrivial behavior. Interestingly enough, this function,

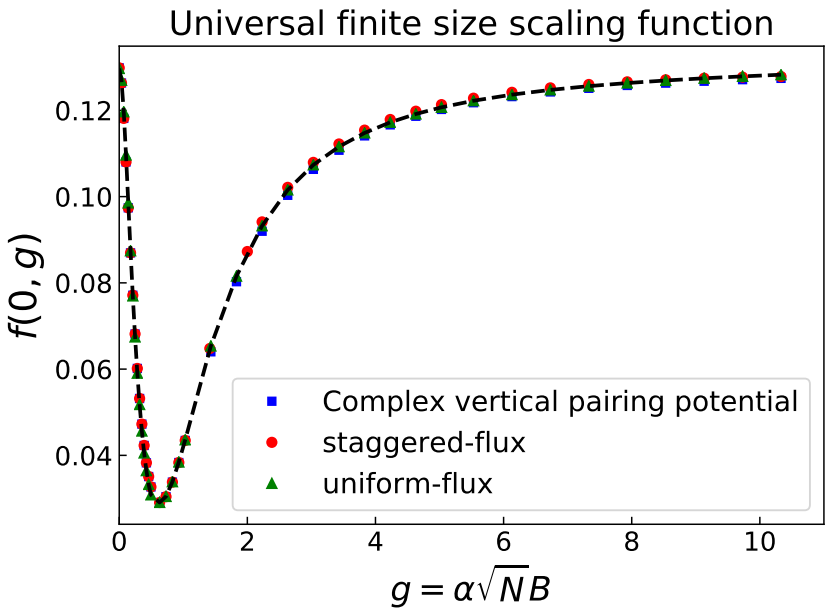

Figure 1.1: (Color online) Universal finite size scaling function $f(w = 0, g)$ plotted at criticality, $w = 0$, versus g. The function is nonmonotonic and exhibits a strong g-dependence. It starts decreasing from the Ising CFT value, $f(0, 0) = \pi/24$, and undergoes a minimum at $g = 0.5$. At $g \gg 1$, it gradually converges to the CFT result, $f(0, g \to \infty) = \pi/24$.

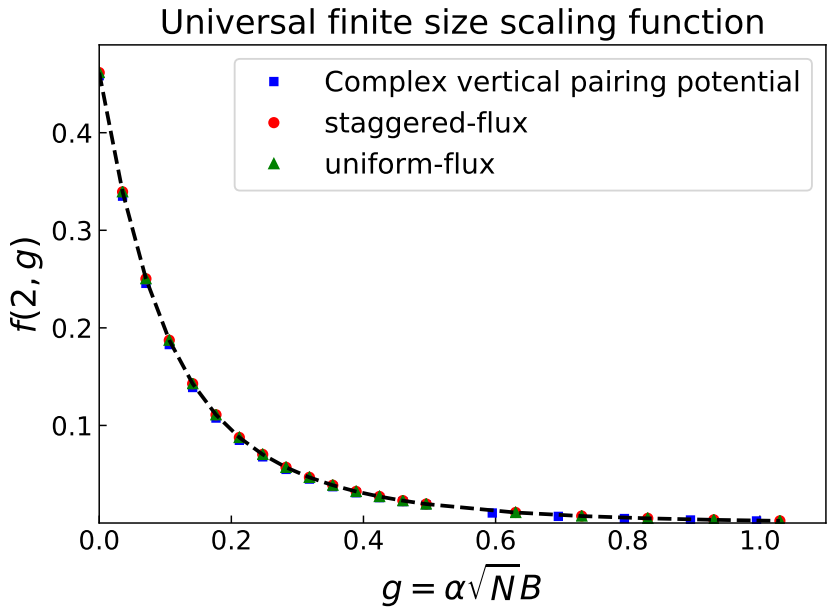

Figure 1.2: (Color online) The universal finite size scaling function $f(w, g)$ is plotted vs. g at $w = 2$ (gapped phase) for three models with different origin of TRS breaking field, B.

plotted in Fig.(1.1), appears to be nonmonotonic and strongly g dependent. The small and large g asymptotes are found to be

$$f(0,g) \simeq \begin{cases} \frac{\pi}{24} + \frac{1}{\sqrt{\pi}} g^2 \log g, & g \ll 1 \\ \frac{\pi}{24} - \frac{\gamma}{g^2}, & g \gg 1. \end{cases} \tag{1.4}$$

Here γ is a constant, numerical value of which is found to be $\gamma \approx 0.24$.

To complete the theoretical picture, we derive the low-energy effective theory describing the symmetry-breaking effect. The theory enables one to analytically uncover the scale, g, which describes physics around the tricriticality, and extract the asymptotic behavior of the finite size scaling function, f. We start with the full-symmetry parent Hamiltonian from BDI class and find its phase diagram in Sect.(1.2). In Sect.(1.3), we define three different symmetry-breaking models where Majorana tri-

critical points emerge. In Sect.(1.4), we numerically show the emergence of g in finite-size scaling function and plot $f(w, g)$ in several different cases. In Sections (1.5) and (1.6), we derive the low-energy theory near the tricriticality and provide its solution. We also show the universal behavior of the boundary entropy in all three models.

1.2 Parent Hamiltonian from BDI symmetry class

In this section, we write down the "parent" Hamiltonian with T, P, and TP symmetries. We show that this model can support three different phases. These are (i) a trivial gapped phase; (ii) a topologically ordered phase supporting two boundary Majorana modes; (iii) symmetry protected topological phase supporting four boundary Majorana modes. At the end of this section, we analytically derive the low-energy effective theory describing the finite-size scaling effect around special critical points which belong to the XY universality class.

We start with two identical Majorana chains with full symmetries of the BDI class:

$$H = H_1 + H_2 + H_{\text{interchain}} \tag{1.5}$$

where H_1 and H_2 are two Hamiltonians, each representing a 1+1D chain. The $H_{\text{interchain}}$ describes coupling between two chains that has the form of interleg hopping and pairing:

$$\begin{aligned} H_m &= -\sum_j \mu \hat{a}^\dagger_{j,m}\hat{a}_{j,m} - \sum_j (t\hat{a}^\dagger_{j+1,m}\hat{a}_{j,m} + h.c.) \\ &+ \sum_j (\Delta \hat{a}_{j,m}\hat{a}_{j+1,m} + h.c.), \quad m = 1, 2 \end{aligned} \tag{1.6}$$

$$H_{\text{interchain}} = \sum_j (-t_v \hat{a}^\dagger_{j,1}\hat{a}_{j,2} + \Delta_v \hat{a}_{j,1}\hat{a}_{j,2} + h.c.). \tag{1.7}$$

Here $\hat{a}^{(\dagger)}_{j,m}$ are fermion annihilation (creation) operators, index $j = 1 \ldots L$ labels the position of a fermion, index m labels the chains, μ is the chemical potential for each of the chains, Δ (Δ_v) is the intrachain (interchain) pairing potential, and t (t_v) is the intrachain (interchain) hopping parameter. One can safely set pairing Δ to be real since its complex phase can be absorbed into fermion operators. In the presence of TRS (and obviously PHS) symmetry, t, t_v and Δ_v are all real.

To obtain the single-particle spectrum, one may introduce the momentum-space fermion operators

$$\hat{a}_{k,m} = \frac{1}{\sqrt{N}} \sum_j \hat{a}_{j,m} e^{ikj} \tag{1.8}$$

where the lattice constant is set to be unity. Then H can be represented in the momentum space as

$$\begin{aligned} H &= \frac{1}{2} \sum_k \hat{\psi}^\dagger_k h(k) \hat{\psi}_k, \qquad \text{with} \\ h(k) &= (-2t \cos k - \mu)\sigma_z \otimes \mathbf{1}_2 + 2\Delta \sin k \sigma_y \otimes \mathbf{1}_2 - t_v \sigma_z \otimes \tau_x + \Delta_v \sigma_y \otimes \tau_y \end{aligned} \tag{1.9}$$

where $\hat{\psi}^\dagger_k = (\hat{a}^\dagger_{k,1}, \hat{a}_{-k,1}, \hat{a}^\dagger_{k,2}, \hat{a}_{-k,2})$, $\boldsymbol{\sigma}$ are Pauli matrices in Nambu space and $\boldsymbol{\tau}$ are Pauli matrices in the space of $m = 1, 2$ Majorana chains. The time reversal symmetry is seen from the commutativity of the anti-unitary operator T with the Hamiltonian, $THT^{-1} = H$, where T acts on spinless fermions as $T\hat{a}_{j,i}T^{-1} = \hat{a}_{j,i}$. Similarly, the particle-hole-symmetry is implied by the operator $P = \tau_x K \otimes \mathbf{1}_2$ in BdG-formalism, where K is the operator of complex conjugation. Thus, one may show that $Ph(-k)P^{-1} = -h(k)$, where $h(k)$ is the k-space hamiltonian in Eq.(1.10).

Diagonalization of $h(k)$ is achieved through the Bogoliubov transformation, yielding the single-particle excitation spectrum

$$E_s(k) = \sqrt{\xi_1(k) + 2s\xi_2(k)} \tag{1.10}$$

where $\xi_1 = (2\Delta \sin k)^2 + (2t\cos k + \mu)^2 + t_v^2 + \Delta_v^2$, $\xi_2 = \sqrt{4\Delta^2 \sin^2 k \Delta_v^2 + \Delta_v^2 t_v^2 + (2t\cos k + \mu)^2 t_v^2}$ and $s = \pm$. Given the spectrum, one can obtain the phase boundaries (critical lines in the phase space of model parameters) by solving the equation, $E_s(k) = 0$, for some k. This yields

$$(2t\cos k + \mu)^2 + \Delta_v^2 - t_v^2 \;=\; 0, \quad (2t\cos k + \mu)\sin k = 0. \tag{1.11}$$

One can further simplify Eqs. (1.11) to obtain the phase boundaries (where the spectral gap closes) at $k = 0; \pi$ as

$$\Delta_v^2 + (2t \pm \mu)^2 \;=\; t_v^2. \tag{1.12}$$

The third phase boundary corresponds to momenta solving the equation $\cos k = \pm\mu/2t$, and parameters satisfying the condition

$$t_v^2 + \frac{\Delta^2}{t^2}(2t + \mu)(2t - \mu) \;=\; \Delta_v^2, \tag{1.13}$$

where $2w > \mu$.

In this work, we are interested in characterizing the topological states via the edge Majorana modes (and thus, we do not explicitly evaluate the topological quantum numbers from the bulk wavefunctions). Since a number of stable edge modes characterize topological phases, below, we will calculate the localization lengths of Majorana modes from the lattice Hamiltonian.

Let us adopt the following notations for Majorana fermion operators

$$c_{2j-1,m} \;=\; \hat{a}_{j,m} + \hat{a}_{j,m}^\dagger, \quad c_{2j,m} = \frac{\hat{a}_{j,m} - \hat{a}_{j,m}^\dagger}{i}$$

where anticommutator $\{c_{j,m}, c_{l,n}\} = 2\delta_{j,l}\delta_{m,n}$. Using these notations, the Hamiltonian can thus be represented in the Majorana basis. The intra-chain part is given by

$$H_m = \frac{i}{2}\sum_j \{-\mu c_{2j-1,m}c_{2j,m} + (\Delta + t)c_{2j,m}c_{2j+1,m} + (\Delta - t)c_{2j-1,m}c_{2j+2,m}\}. \quad (1.14)$$

The interchain part is written as

$$H_{\text{interchain}} = \frac{i}{2}\sum_j (\Delta_v - t_v)c_{2j-1,1}c_{2j,2} + (\Delta_v + t_v)c_{2j,1}c_{2j-1,2}. \quad (1.15)$$

Using the Majorana representation of the Hamiltonian, we can diagonalize it and find the Majorana zero energy states that are localized at the boundaries of the chain. We show that the question of the existence of Majorana zero-energy states reduces to the estimation of the localization length $\xi_\pm$. The latter is found from the wavefunction that decays into the bulk exponentially as $\exp\{-x/\xi_\pm\}$, with

$$\xi_\pm^{-1} = \ln \frac{2t}{\mu \pm \sqrt{t_v^2 - \Delta_v^2}}. \quad (1.16)$$

Here, if the argument of the logarithm is negative, $\xi_\pm^{-1}$ obtains a complex phase, $i\pi$, indicating an oscillatory wavefunction. Thus,

- (i) if $\xi_+ > 0$ and $\xi_- > 0$, the system is in the gapped phase with four localized zero-energy Majorana modes.
- (ii) if $\xi_+ > 0 (\xi_+ < 0)$ and $\xi_- < 0 (\xi_- > 0)$, the system is in the gapped phase with two localized zero-energy Majorana modes.
- (iii) if $\xi_+ < 0$ and $\xi_- < 0$, the system is in the trivially gapped phase with no localized zero-energy Majorana modes.

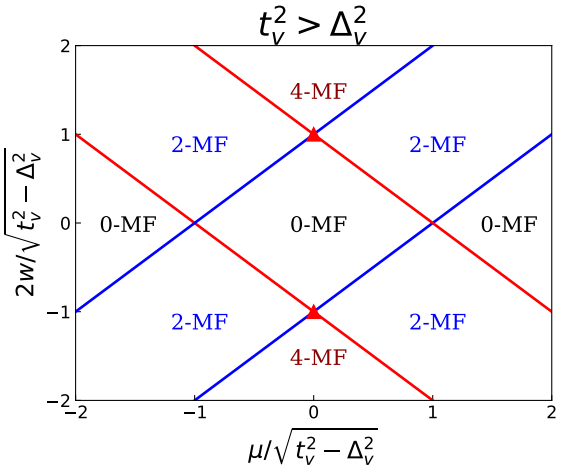

Figure 1.3: (Color online) Phase Diagram for Parent Hamiltonian from BDI symmetry class. n-MF represents gapped phase with n localized zero-energy Majorana modes. There are three different phases 0-MF, 2-MF and 4-MF. Critical points in the phase diagram are Ising universality with central charge $c = 1/2$, but intersection points of two critical lines are XY-universality with central charge $c = 1$. Two special intersection points located at $(0, \pm 1)$ are emphasized as red triangle points. Two relevant perturbations μ and $2w$ will drive the system away from the criticality: tuning μ opens a gap to 2-MF; tuning $2w$ opens a gap to 4-MF or 0-MF.

These three different phases are shown on the phase diagram Fig. (1.3) in the space of rescaled energies w and μ. Throughout this section, we will adopt the notation "n-MF" to represent the gapped phase with n localized zero-energy Majorana modes (below we will deal with cases with $n = 0, 2, 4$).

The critical lines (or, in other words, the phase boundaries) in the phase diagram Fig. (1.3) belong to the Ising universality class with central charge $c = 1/2$. The exceptions are the intersection points of two critical lines, which belong to the XY universality with central charge $c = 1$. Two relevant perturbations, given by the change of critical μ and $2w$, will drive the system away from criticality. Tuning of parameter μ opens a gap and drives the system into 2-MF state. Tuning of $2w$ opens a gap, and the system finds itself either in 4-MF or 0-MF state.

One can calculate the finite size corrections to the ground state energy around the XY criticality. To this end, we define two masses $m_{\pm}$

$$m_{\pm} = \frac{2t \pm \mu - \sqrt{t_v^2 - \Delta_v^2}}{2t}. \tag{1.17}$$

The magnitudes of m_+ and m_- are the spectral gaps measured at $k = 0$ and $k = \pi$ respectively. Interestingly, the low-energy effective theory around the criticality is given by a direct sum of two massive Majorana field theories:

$$H_{\text{low}} = \sum_{s=\pm} \frac{iv_F}{2} \int dx \eta_s^T \begin{pmatrix} \partial & m_s \\ -m_s & -\partial \end{pmatrix} \eta_s, \tag{1.18}$$

where $\eta_{\pm}$ is a two-component Majorana field operator. To evaluate the finite-size scaling function corresponding to a single copy of Majorana field from Eq. (1.18), one may double the number of degrees of freedom in Majorana field theory above and form a $1+1$D massive Dirac field. Then one will recover the finite-size scaling function, $f_D(w)$ (defined in Eq. (1.2)), for $1+1$D Dirac field theory.

In the present situation, for low-energy Hamiltonian Eq. (1.18), we obtain that finite size scaling function $\tilde{f}$ becomes function of two masses, $w_+ = Nm_+$ and $w_- = Nm_-$:

$$\tilde{f}(w_+, w_-) = \frac{1}{2}\{f_{\text{D}}(w_+) + f_{\text{D}}(w_-)\}, \tag{1.19}$$

where the factor $1/2$ eliminates the double counting of degrees of freedom in Dirac field theory, as the latter is equivalent to the direct sum of two Majorana field theories.

Instead of plotting $\tilde{f}(w_+, w_-)$ in a 3D space as a 2D surface parametrized by two scales w_+, w_-, we chose $|w_+| = |w_-| = w$ and plot $\tilde{f}(w, w)$ vs w. This plot will bear all the necessary information about the naure of the phases as follows:

- i) From definition of masses in Eq.(1.17), we see that if $(w_+, w_-) = (w, w)$ with $w > 0$, then both masses are positive and the system is in the 4-MF phase.

Below we will use the notation $f_4(w) \equiv \tilde{f}(w,w)$, for the finite size scaling function in the 4-MF phase.

- ii) If $(w_+, w_-) = (w, -w)$ (or $(-w, w)$), $w > 0$, then one of the masses is positive (indicating the existence of two localized Majorana modes)while the other is negative (indicating a trivial boundary). In this case one has the 2-MF phase. Below we will use the notation $f_2(w) \equiv \tilde{f}(w,-w) = \tilde{f}(-w,w)$ for the finite size scaling function in 2-MF phase.

- iii) Finally, when $(w_+, w_-) = (-w, -w)$, $w > 0$, one obtains a trivial 0-MF phase. The corresponding finite size scaling function is denoted as $f_0(w) \equiv \tilde{f}(-w,-w)$.

Thus we obtain three finite size scaling functions, f_0, f_2 and f_4, of a single variable w. These functions are depicted in Fig. (1.4). We see that f_4 is has a pronounced maximum at the topological 4-MF phase; f_2 exhibits a less pronounced maximum in the 2-MF phase; and f_0 is a featureless decaying function in the trivial 0-MF phase. The inset to Fig. (1.4) shows the small w behavior of f_2 suggesting that it is completely regular and $df_2/dw|_{w=0} = 0$. The latter property is expected from Eq.(1.19).

Properties of $\tilde{f}(w_+, w_-)$ follow from the fact that we have a direct sum of non-interacting Hamiltonians at intersections of two critical lines in Fig. 1.3. The same procedure is straightforwardly generalized to more complex situations, where one has N intersecting critical lines, each represented by a central charge c_i, $i = 1 \ldots N$, (e.g., if there are many coupled Majorana chains). In this case the finite size scaling function becomes multi-variable, and equal to $\tilde{f}(w_1, w_2, ..., w_n) = \sum_{i=1}^{N} c_i f_D(w_i) / \sum_i^N c_i$.

1.3 Models with broken time-reversal symmetry

In the above section, we discussed and solved models whose parameters are real, and whose Hamiltonian operators preserve time-reversal symmetry (TRS). In this

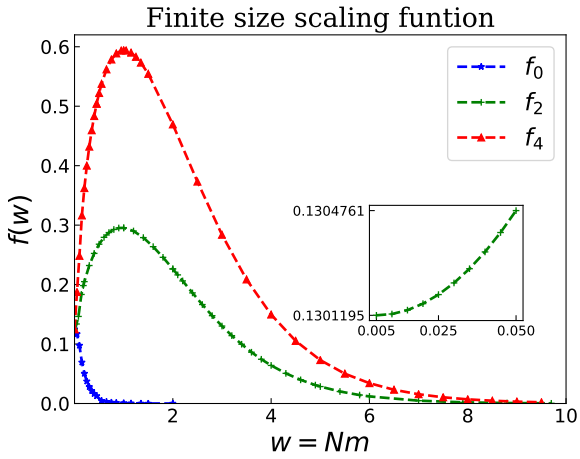

Figure 1.4: (Color online) Finite size scaling functions, $f_n(w)$, for $n = 0, 2, 4$ around the criticality marked by the (red) triangle in Fig.1.3. Inset: The behavior of f_2 at small $w \ll 1$. The finite size scaling function clearly distinguishes all three different phases around the criticality.

section, we will consider two-leg ladder models, where the TRS is explicitly broken. This can be achieved, e.g., through endowing a *complex* phase to model parameters in such a way that it cannot be gauged out. We introduce three different TRS breaking models and prove the existence of Majorana tricriticality between topologically ordered, SPT, and trivial phases in each of them. Consequently, we trace the evolution of the single-particle spectrum with varying the TRS breaking field, B, around the tricriticality.

1.3.1 Model I: Ladder with complex vertical pairing potential

The complex phase of the pairing potential, Δ, in the single Majorana chain, can be gauged out (through absorbing it into fermion operators). However, if one starts with the parent Hamiltonian Eq. (1.5) and introduces complex phases to Δ and Δ_v, then only one of these two phases can be gauged out (the complex phases of Δ and Δ_v cannot be simultaneously absorbed into fermion operators). Below we will work in the gauge where Δ is real while Δ_v is a complex number: $\Delta_v = |\Delta_v|e^{i\theta} = \Delta_v^R + i\Delta_v^I$. The parameter θ is thus the phase difference between Δ and Δ_v. The corresponding

Hamiltonian reads

$$\begin{aligned} H_{\text{interchain}} &= \frac{i}{2}\sum_j (\Delta_v^R - t_v) c_{2j-1,1} c_{2j,2} + \frac{i}{2}\sum_j (\Delta_v^R + t_v) c_{2j,1} c_{2j-1,2} \\ &+ \frac{i}{2}\sum_j \Delta_v^I (c_{2j-1,1} c_{2j-1,2} - c_{2j,1} c_{2j,2}) \end{aligned} \tag{1.20}$$

In this model, the TRS breaking field B is identified with $B \equiv \Delta_v^I/2t$, as the vertical complex pairing terms, $\propto c_{m,1}c_{m,2}$, do break the TRS.

The Hamiltonian, H, is represented in momentum space as follows

$$H = \frac{1}{2}\sum_k \hat{\psi}_k^\dagger h(k) \hat{\psi}_k, \tag{1.21}$$

$$\begin{aligned} h(k) &= (-2t\cos k - \mu)\sigma_z \otimes \mathbf{1}_2 + 2\Delta \sin k \sigma_y \otimes \mathbf{1}_2 \\ &- t_v \sigma_z \otimes \tau_x + \Delta_v^R \sigma_y \otimes \tau_y - \Delta_v^I \sigma_x \otimes \tau_y. \end{aligned} \tag{1.22}$$

Complex Δ_v^I completely changes the structure of the single-particle excitation spectrum. We apply the Bogoliubov transformation to diagonalize $h(k)$ to get the spectrum $E_s(k)$ as

$$E_s(k) = \sqrt{\xi_1^p(k) + 2s\xi_2^p(k)}, \quad \xi_1^p = (2\Delta \sin k)^2 + (2t\cos k + \mu)^2 + t_v^2 + |\Delta_v|^2$$

and $\xi_2^p = \sqrt{4\Delta^2 \sin^2 k (\Delta_v^R)^2 + |\Delta_v|^2 t_v^2 + (2t\cos k + \mu)^2 t_v^2}$, $s = \pm$. As the next step, we proceed with the identification of the 0-MF, 2-MF, and 4-MF phases. This can be achieved by following the procedure outlined for the parent Hamiltonian in Sec. 1.2: upon solving the equation $E_s(k) = 0$, one obtains

$$\begin{aligned} (2t\cos k + \mu)^2 + |\Delta_v|^2 - t_v^2 &= 0 \\ (\Delta_v^I \sin k)^2 + (2t\cos k + \mu)^2 \sin^2 k &= 0. \end{aligned} \tag{1.23}$$

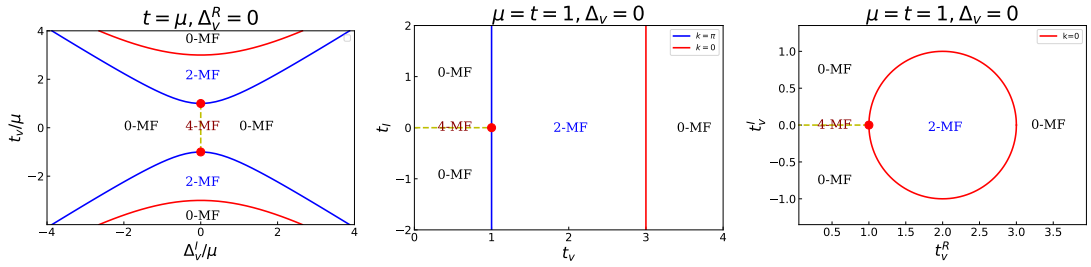

(a) Complex vertical pairing potential

(b) Uniform Flux

(c) Staggered Flux

Figure 1.5: (Color online) Phase diagrams of (a) Model I, (b) Model II, and (c) Model III. All three phase diagrams support the tricriticality, marked by a bold (red) dot. It separates 4-MF, 2-MF and 0-MF phases. In all three diagrams, the 4-MF phase resides on the dashed (yellow) line. It is smoothly connected to 0-MF when the field B is added, while 2-MF is robust to TRS-breaking perturbation.

Then the phase boundaries of the phase diagram are given in terms of parameters $|\Delta_v|$, t, μ, and t_v satisfying the equation

$$|\Delta_v|^2 + (2t \pm \mu)^2 \quad = \quad t_v^2. \tag{1.24}$$

Along these boundaries, the spectral gap closes at momenta $k = 0, \pi$.

As the next step, we diagonalize the Hamiltonian (1.5) with $H_{\text{interchain}}$ given by Eq. (1.20) in the Majorana basis with open boundary conditions. Subsequently we numerically analyse the eigenvalues of the Hamiltonian and obtain complete information on the zero-energy boundary modes. The phase diagram is plotted in Fig (1.5a) in the space of rescaled parameters w_v and Δ_v^I. All three different phases, namely 4-MF, 2-MF and 0-MF phases exist in this phase diagram:

- The 4-MF, is an SPT phase characterized by the $\mathbb{Z}_2^T$ quantum number. It can be smoothly connected to the topologically trivial phase without closing a gap in the presence of the TRS-breaking field. Thus the 4-MF SPT phase resides only on the dashed (yellow) line of the diagram, while to the left/right of it, the TRS is broken, and the phase is trivial.

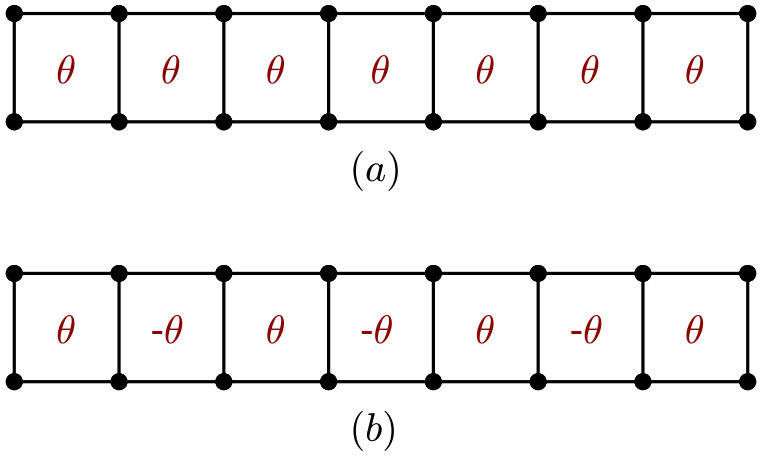

Figure 1.6: (Color online) Parent model in the presence of an external TRS breaking flux field. (a) Uniform magnetic field. (b) Staggered magnetic field.

- The 2-MF phase is topologically ordered. It is robust to TRS breaking perturbation, and the Majorana modes are immune to B.
- The 0-MF phase is topologically trivial.

1.3.2 Model II: Ladder in a uniform magnetic field

The ladder model has square plaquettes that can be threaded by magnetic fluxes and around which a fermion can rotate. In this subsection, we will consider a model that corresponds to the parent Hamiltonian (1.5) in the presence of an external constant magnetic field. Thus each square plaquette of the ladder is penetrated uniformly by the flux, θ, as shown in Fig. (1.6)a. The gauge field, which generates the uniform flux, couples to fermion hoppings along the links. For simplicity, we chose to work in the gauge where the complex phase is added to the intra-chain hopping, t: $te^{i\theta/2}$ in

H_1 and $te^{-i\theta/2}$ in H_2. The Hamiltonian of Model II is thus given by Eq. (1.5), where $H_{\text{iterchain}}$ is unchanged and

$$\begin{aligned} H_1 &= \sum_j \mu \hat{a}^\dagger_{j,m}\hat{a}_{j,m} + (\Delta \hat{a}_{j,m}\hat{a}_{j+1,m} + h.c.) - (te^{i\theta/2}\hat{a}^\dagger_{j+1,m}\hat{a}_{j,m} + h.c.) \\ H_2 &= \sum_j \mu \hat{a}^\dagger_{j,m}\hat{a}_{j,m} + (\Delta \hat{a}_{j,m}\hat{a}_{j+1,m} + h.c.) - (te^{-i\theta/2}\hat{a}^\dagger_{j+1,m}\hat{a}_{j,m} + h.c.). \end{aligned} \quad (1.25)$$

Here the intra-chain terms $H_{1,2}$ reduce to the parent Eq.(1.6) at $\theta = 0$. We remind the reader that the uniform flux θ breaks the TRS and thus the TRS breaking field B here is identified with $B \equiv \frac{1}{2}\sin(\theta/2)$. The momentum space representation of the Hamiltonian in the Majorana basis helps to trace the modification of i) the boundary modes, and ii) of the bulk spectrum.

The phase diagram of the uniform-flux model under consideration contains three different phases: a trivial 0-MF phase, a topologically ordered 2-MF phase, and an SPT 4-MF phase that is situated on a line. All three phases come together, giving rise to a tricritical point. The two phase boundaries of the model are given by the equation

$$(2t_R \pm \mu)^2 = t_v^2 - \Delta_v^2 \quad (1.26)$$

where $t_R = t\cos\theta/2$. It is clear that t_I does not influence the phase boundary equation in any way. The phase diagram in the space of parameters t_I and t_v is shown in Fig. 1.5b.

1.3.3 Model III: Ladder in a staggered magnetic field

One can break the TRS also by introducing a staggered magnetic field, instead of the uniform magnetic flux discussed in the previous section. Here we consider a staggered θ flux threading each of the square plaquettes of the ladder, whose signs

are alternating. An example of a certain lattice segment with fluxes is shown in Fig. 1.6b. The staggered disposition of the sign of θ implies doubling of the unit cell, the net flux through which is zero. The corresponding single particle Hamiltonian, based on the parent model 1.5, can be written in gauge where alternating complex phases are attached to vertical interchain hopping parameters: $t_v \to t_v e^{\pm i\theta/2}$ with alternating signs. Thus, the full Hamiltonian is still given by Eq. (1.5), with the interchain Hamiltonian being

$$H_{\text{interchain}} = -\sum_{j=2n-1} t_v e^{i\theta/2} \hat{a}^\dagger_{j,1} \hat{a}_{j,2} - \sum_{j=2n} t_v e^{-i\theta/2} \hat{a}^\dagger_{j,1} \hat{a}_{j,2} + \sum_j \Delta_v \hat{a}_{j,1} \hat{a}_{j,1} + h.c. \quad (1.27)$$

where the staggered field θ breaks the TRS. Thus, we identify the TRS breaking field B here with $B \equiv t_v \sin(\theta/2)/(2t)$.

As the next step, we study bulk and boundary spectra of the model. To derive the bulk spectrum, we perform Fourier transformation in Eq. (1.27), which diagonalizes the Hamiltonian.

The outlined analysis helps us to study the phase diagram of the model systematically. The phase boundaries separating the trivial 0-MF phase, a topologically ordered 2-MF phase, and an SPT 4-MF phase are given by

$$(2t \pm t_v^R \pm \Delta_v)^2 + (t_v^I)^2 = \mu^2. \quad (1.28)$$

Here t_v^I does enter into the expression for phase boundaries, which now in the space of parameters t_v^I and t_v^R becomes very interesting. It is shown in Fig. (1.5c), from which we see that it is topologically different from the one corresponding to the uniform magnetic field. In particular, the space corresponding to the 2-MF state is now compact.

1.3.4 Phase diagrams of models with broken TRS

In this subsection, we will discuss common features of all three phase diagrams corresponding to the models I, II, and III defined above. In each phase diagram, shown in Fig. (1.5a), Fig. (1.5b), and Fig.(1.5c), there is a peculiar 4-MF phase, which resides on a dashed (yellow) line. The dashed line itself also represents a first-order phase transition line. It has the following description: when the TRS breaking field, B, is added to the 4-MF state, the ground state degeneracy is *lifted*. This happens because the zero-energy boundary modes obtain finite energy proportional to B. Then the spectrum develops a level-crossing, signaling the first-order phase transition. There are phase boundaries corresponding to the second-order phase transitions between 2-MF and trivial phases shown in Fig. (1.5) by full lines (blue and red). Interestingly enough, the tricriticality happens as the intersection of the first-order transition line and the second-order transition line. The study of the *universal* properties around this tricriticality, shown by bold (red) dots in Fig. (1.5), is the main focus of the present chapter.

The tricriticality separates three different phases: 4-MF(characterized by $\mathbb{Z}_2^T$ topological invariants of the SPT theories), 2-MF(fermionic topologically ordered phase) and 0-MF (trivial phase).

- In 4-MF phase, near the tricriticality, two Majorana edge modes have localization lengths ξ_+ while the other two have localization length ξ_-, see Eq.(1.16) for definitions.

- The Majorana edge modes in a 2-MF phase, near the tricriticality, are characterized only by one localization length.

- At the tricriticality, there are two Majorana edge modes, with the same localization lengths ξ. As one departs from tricriticality in Fig. (1.5), and moves along the gapless phase boundary (the blue line), one immediately enters the trivial

gapless phase with no boundary Majorana modes. To achieve such a nontrivial transition, one will have to tune the model parameters correspondingly. Unlike this critical line, the tricriticality does support two Majorana modes, and as such, it represents an example of the gapless SPT phase.

The phase diagram Fig.(1.5a) has two tricritical points positioned at $(\Delta_v^I, t_v) = (0, 1)$ and $(\Delta_v^I, t_v) = (0, -1)$ (measured in units of $\mu = t$). The Majorana localization lengths at the former is ξ_- while at the latter it is ξ_+. In two other TRS breaking situations, only one tricritical point is shown, however, there are two such points as the phase diagrams are symmetric with respect to the vertical axis.

In all three situations with TRS breaking and the tricriticality, we define the universal dimensionless scale g as:

$$g = \alpha(\xi)\sqrt{N}B. \tag{1.29}$$

The function, $\alpha(\xi)$, is model dependent. The reason it enters into the universal scale, g, is the following. Besides the diverging correlation length, $\xi_{\mathbf{cor}} = \infty$, there is one more length scale, the localization length ξ, around the tricriticality. The models under consideration are described by short-ranged hoppings and pairings. These short-ranged terms are characterized by the lattice constant a, which is set to be unity throughout this section. The universal phenomena at criticalities emerge when $1 \ll \xi_{\mathbf{cor}}$. However, the new length scale ξ, which appears to be finite, needs to be carefully treated and compared with the existing scales: i) when $\xi \ll 1 \ll \xi_{\mathbf{cor}}$ the short-ranged properties, characterized by the lattice spacing (~ 1), can be captured by neither the localization length ξ nor the correlation length $\xi_{\mathbf{cor}}$. Thus $\alpha(\xi = 0) \equiv 1$, which is universal for all three models; ii) when $\xi \sim 1$, i.e, the localization length is comparable with lattice spacing, the short-ranged physics matters. That is the reason why the model-dependent function $\alpha(\xi)$ determines the scale, g.

In the next section, we will show how the scale g naturally emerges in the universal finite-size scaling corrections to ground state energy.

1.4 Universal finite-size scaling

In this section, we will show the emergence of the universal scale g describing the finite size correction to the ground state energy around the tricriticality. Namely, we will show that the finite size correction to the ground state energies of models I, II, and III has the universal form given by Eq. (1.3).

Further, we will show that in two simultaneous double-scaling[50] limits: a) $N \to \infty$, $m \to 0$ with $w = const$ and b) $N \to \infty$, $B \to 0$, with $g = const$, the function $f(w, g)$ is a universal function of two variables (in Eq. (1.3). To uniquely identify $f(w, g)$ around the tricriticality, we adopt the following convention: we chose the sign of m to be $m > 0$ for 4-MF and for 0-MF, while $m < 0$ for 2-MF).

1.4.1 Numerical approach

Here we outline the numerical approach for the calculation of the ground state energy, $E(N, m, B)$. We obtain it by performing a summation of the occupied single-particle energy levels corresponding to the Hamiltonian under open boundary conditions. The per-particle average bulk energy, $\epsilon(m, B)$, is obtained upon summing up the occupied energies and dividing the result by N. This procedure yields

$$\epsilon \;=\; -\frac{1}{4\pi}\int_{BZ} dk \sum_{s} E_s(k) \tag{1.30}$$

where BZ stands for the Brillouin zone, $E_s(k)$ is single-particle excitation energy in the k-space corresponding to band s. For example, in case of model I, one has 2

energy bands and thus s acquires only two values $s = \pm$ (for this model, $E_s(k)$ is given by Eq.(1.23)). The boundary energy, $b(m, B)$, is then given by

$$b = \lim_{N\to\infty} \left(E(N, m, B) - N\epsilon(m, B)\right). \tag{1.31}$$

Having identified all the necessary ingredients, the finite size scaling function f is obtained from

$$f = \lim_{n\to\infty} n \cdot \left(E(n, m, B) - n\epsilon(m, B) - b\right). \tag{1.32}$$

Numerically, we pick a large system with $N_0 = 1000$ and compute $\tilde{b} = E(N_0, m, B) - N_0\epsilon(m, B)$. Having evaluated the boundary energy, $\tilde{b}$, we take $n_0 = 100$ to evaluate the finite size scaling function, labeled by $\bar{f}$: $\bar{f} = n_0 \cdot \Big(E(n_0, m, B) - n_0\epsilon(m, B) - \tilde{b}\Big)$. The outlined computation is based on two approximations: i)The evaluated boundary energy $\tilde{b}$ generates an error $e_1 \sim \mathcal{O}(n/N)$ that contributes to $\bar{f}$. ii) The higher order terms are ignored, which yields an error e_2 $\mathcal{O}(n^{-1})$ to $\bar{f}$. The total error is thus $f - \bar{f} \sim \mathcal{O}(n/N) + \mathcal{O}(n^{-1})$. By keeping track of these errors and accumulating statistics, one can obtain an accurate data for f with controlled precision.

1.4.2 Emergence of the new scale g

In this subsection, we take the model I: coupled Majorana chains with *complex vertical pairing potential* as an example and use the method of Sec.(1.4.1) to evaluate its finite scaling f. Then we show that f is a double scaling function of two variables, the standard variable Nm and a completely new emergent scale g.

There are several important quantities around the tricriticality: i)The spectral gap m, (which is identified with the mass of the low-energy effective field theory); ii) The localization length, ξ, of Majorana edge modes existing at the tricriticality, which characterize the topological properties of the tricritical point; iii) The system

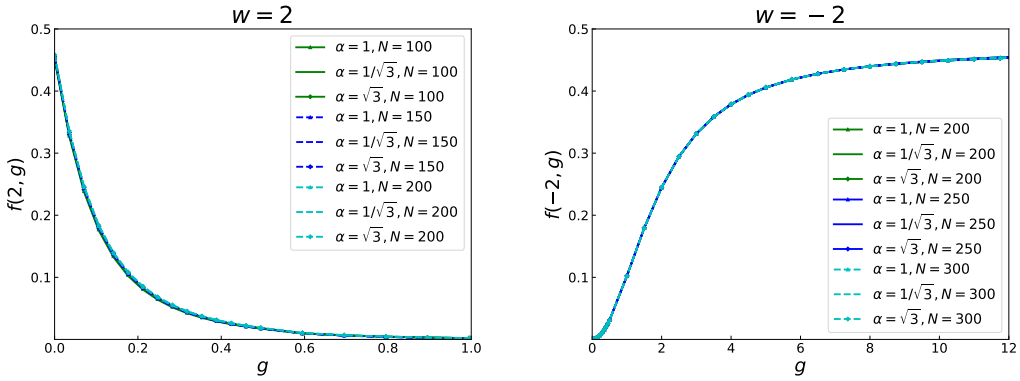

(a) (b)

Figure 1.7: (Color online) The finite size scaling function f is plotted as a function of g for Model I. Fig.(1.7a) corresponds to $w = 2$ and Fig.(1.7b) corresponds to $w = -2$. These curves have been obtained for nine different values of $\alpha = \sqrt{\coth 1/2\xi}$ and N.

size, N, which is the essential ingredient for studies of finite size effects; iv) The symmetry-breaking field B, which induces the tricriticality. We find that the finite scaling f does explicitly depend on certain combinations of m, N, ξ and B: if we vary m, N, ξ and B keeping $g = \sqrt{N \coth(1/2\xi)}B$ (for Model.I) and $w = Nm$ constant, f always yields exactly the same value. This means that $f \equiv f(w, g)$ is only a function two variables, w and g. This observation puts forward the definition of the scale g in Eq.(1.29). The scale $w = Nm$ is consistent with previous papers on the finite-size scaling effect with no TRS breaking [2, 33].

Figs.(1.7a) and (1.7b) give concrete results to support that f is a function of g: f yields the same value if we keep g to be constant simultaneously changing N, ξ, and B. In the remainder of the chapter, we will use $f(w, g)$ to represent the finite-size scaling around the tricriticality.

1.4.3 Universality

We calculate the scaling function f for all three models introduced in Sect.(1.3). We show the universality nature of $f(w, g)$ for all of them. In each model, symmetry-

breaking B is realized in different ways by involving different lattice parameters: Δ_v^I is imaginary part of the vertical pairing potential for model I in Sec.(1.3.1), t^I is imaginary part of the intra-chain hopping for model II in Sec.(1.3.2), and t_v^I is imaginary part of vertical hopping for model III in Sec.(1.3.3).

We find that all three models yield the same finite-size scaling function $f(w, g)$, although the field B has different origins in them. Fig.(1.1) depicts $f(w = 0, g)$ at criticality for all three models, and Fig.(1.2), depicts $f(w = 2, g)$ corresponding to the gapped phase for all of them. These plots support the universality, either at the criticality or for the gapped phase. The finite size scalings $f(w, g)$, calculated for three models, provide the same sets of curves.

1.4.4 Features of the finite size scaling function $f(w, g)$

Here we analyse the features of $f(w, g)$. The function itself is given by a 2D surface in a 3D space of (w, g, f). We depict some of the curves residing on this surface: for each value of w, we plot $f(w, g)$ as function of g. We use the parameters of the complex-vertical pairing model I as an example to present $f(w, g)$ (although f is universal, for simplicity of the presentation we work in the parameter space of this model).

The results are as follows: Figs.(1.8) and (1.9) show the behavior of $f(w, g)$ with w ranging between $1 \leq w \leq 5$ and $-5 \leq w \leq -1$. When w belongs to these intervals, $f(w, g)$ is a monotnoic function of g. In the first interval, $f(+|w|, g)$ decays exponentially as a function of g, while in the second one, $f(-|w|, g)$ converges slowly (which is in fact $\propto g^{-2}$ at large g). Figs. (1.10) and (1.11) show the behavior of $f(w, g)$ in the interval $-0.1 < w < 0.1$ For small $|w| < 0.1$, $f(w, g)$ is a non-monotnoic function of g. At the criticality, $w = 0$, the finite size scaling $f(0, g)$ strongly depends on the scale g. Fig.(1.12) shows that the function $f(w, g)$ saturates to a constant value as $\propto g^{-2}$ at large g.

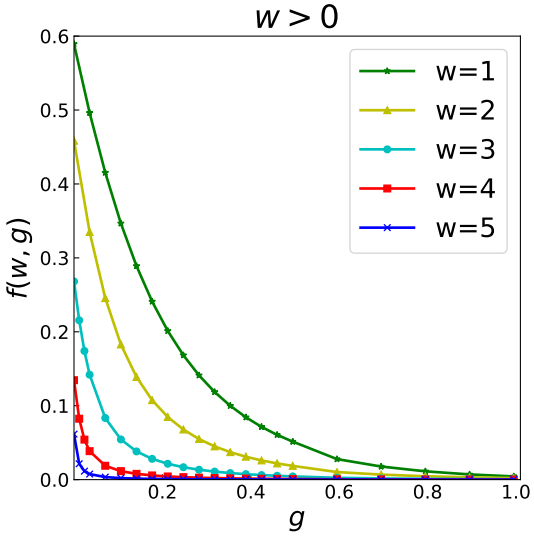

Figure 1.8: (Color online) The finite size scaling functions at $w \geq 1$. Curves from top to bottom correspond to values $w = 1, 2, 3, 4, 5$. Here only the $g \leq 1$ is presented. As w increases, $f(w, g)$ decays faster since larger w means being further away from second order phase transition. Then, the contribution coming from the first order transition dominates.

At this stage, it is interesting to compare our universal finite-size scaling function $f(w, g)$ with the result of Ref. [33] for the scaling function, $f_{\rm D}(w)$. The latter was calculated in a situation, where there were no tricriticalities. From all the curves above, we confirm the role of g: g provides interpolation between $f_{\rm D}(w)$ and $f_{\rm D}(-w)$ by $f(w, g = 0) = f_{\rm D}(w)$ and $f(w, g = +\infty) = f_{\rm D}(-w)$. For example, it is shown in Ref. [33] that $f_{\rm D}(1) \approx 0.6$ in a 1D topological phase while $f_{\rm D}(-1) \approx 0$ in a trival phase. The curve with $w = 1$ in Fig.(1.8) provides the decaying function $f(1, g)$ from 0.6 (that is the value of $f_{\rm D}(1)$) to 0 (value of $f_{\rm D}(-1)$).

1.5 Low-energy effective theory around the tricriticality

In the section, we start from the parent Hamiltonian $h(-i\partial_x)$, given by Eq. (1.10), which supports the low-energy Majorana field theory and two Majorana edge modes. As the first step, we rewrite the symmetry-breaking Hamiltonian $H_{\rm interchain}(B) -$

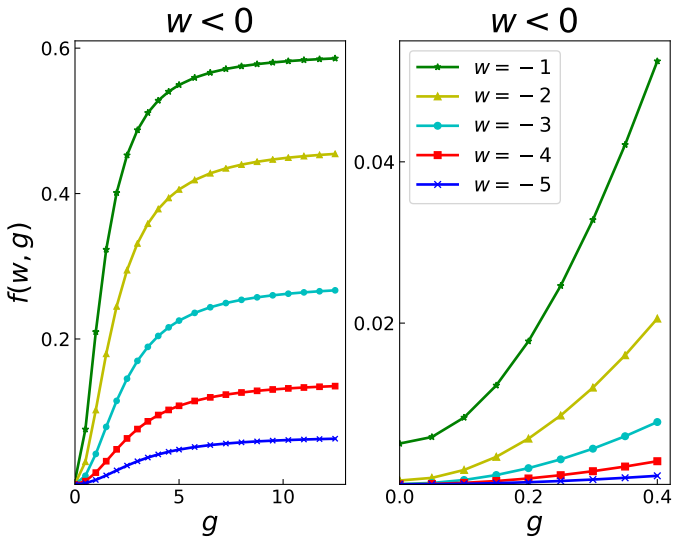

Figure 1.9: (Color online) The finite size scaling function at $w \leq -1$. The left figure depicts the scaling function when g varies from 0 to 12, while the right figure depicts the behavior when $0 \leq g \leq 0.4$.

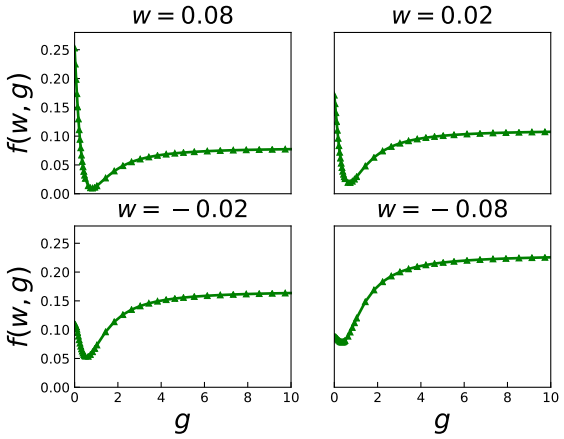

Figure 1.10: (Color online) The finite size scaling function at $-0.1 < w < 0.1$.

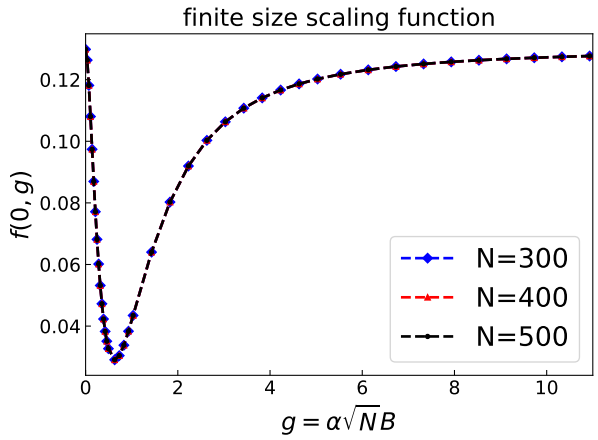

Figure 1.11: (Color online) The finite size scaling function at criticality ($w = 0$) plotted for three different values of N.

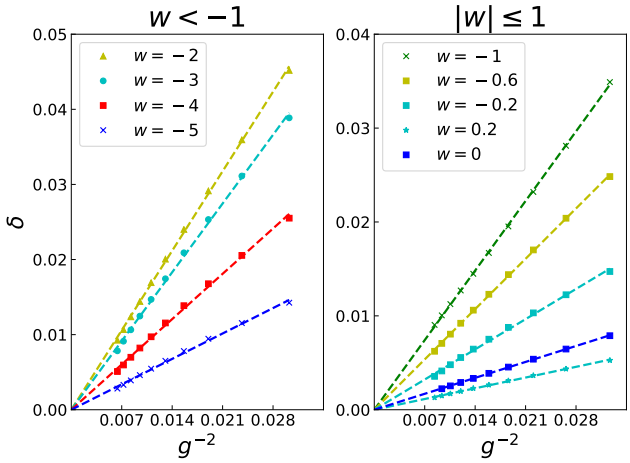

Figure 1.12: (Color online) The linear fit of $f(w, g)$ versus g^{-2} is shown at $g \gg 1$: $f(w, g) = f(w, \infty) - \beta/g^2$. Figures depict the function $\delta = f(w, \infty) - f(w, g)$ versus g^{-2}. The g-independent shift $f(w, \infty)$ is given by the constant part in the linear fit.

$H_{\text{interchain}}(B = 0)$, where $H_{\text{interchain}}(B)$ is given by Eq. (1.20), in the momentum representation. This yields $h_B = -B\sigma_x \otimes \tau_y$, that acts as a perturbation to the parent Hamiltonian. Then we consider the low-energy sector of the perturbed theory by calculating the matrix elements of h_B using the low-energy eigenstates of the full parent Hamiltonian (note that in this basis the parent $h(-i\partial_x)$ is diagonal). At this level, we explicitly show the emergence of the new scale, g, in the low-energy effective matrix. Finally, we obtain the spectrum of the effective matrix and analyze the essential properties around the tricriticality.

1.5.1 Low-energy sector

Here we identify the low-energy eigenstates of the parent Hamiltonian $h(-i\partial_x)$, around the tricriticality. Diagonalization of $h(-i\partial_x)$ yields two energy bands that are above the chemical potential. The lower one corresponds to the low energy states being described by the $1+1$D Majorana field theory. The higher energy band also brings upon states supporting and protecting Majorana zero-energy edge modes. In this way, we obtain two sets of low-energy states: i) states that are described by $1+1$D Majorana field theory. We call these states MFT-states. ii) zero-energy edge modes that are protected by the topological number of the higher energy band of the ladder model.

We take Model I with the *complex-vertical pairing potential* as an example, and start from the Hamiltonian $h(-i\partial_x)$:

$$\begin{aligned} h(-i\partial_x) &= (-2t\cos(-i\partial_x) - \mu)\sigma_z \otimes \mathbf{1}_2 \\ &+ 2\Delta \sin(-i\partial_x)\sigma_y \otimes \mathbf{1}_2 - t_v \sigma_z \otimes \tau_x \end{aligned} \tag{1.33}$$

where we took $\Delta_v = 0$ for simplicity (as it does not affect the universal properties under consideration).

Around the criticality, the wavefunction of the lower band can be obtained from linearization of $h(-i\partial_x)$. The operator $h(-i\partial_x)$ has two energy bands above the chemical potential, with the lowest one being $E_k = \sqrt{m^2 + k^2}$ with $m = (2t - \mu - w_v)/(2t)$, at $\mu, w > 0$. The corresponding eigenstates are the MFT-states. For an infinite system (no imposed boundary conditions), these MFT states are characterized by good quantum numbers k(momentum) and n(energy):

$$h(-i\partial_x)e^{ikx}u(n,k) = n \cdot 2t\sqrt{m^2 + k^2}e^{ikx}u(n,k) \tag{1.34}$$

where in principle, k can be either real or imaginary and $u(n,k)$ is a four-component vector function of n and k. Now, we impose the following geometry constraints: assume the system has a finite length $(0, N)$ and four-component eigenstates of $h(-i\partial_x)$, $\varphi_i(x)$, $i = 1 \ldots 4$, satisfy the following boundary conditions

$$\begin{aligned} \varphi_1(0) - \varphi_2(0) &= \varphi_3(0) - \varphi_4(0) = 0 \\ \varphi_1(N) + \varphi_2(N) &= \varphi_3(N) + \varphi_4(N) = 0. \end{aligned} \tag{1.35}$$

We find that the eigenstates of $h(-i\partial_x)$, which also satisfy the boundary conditions (1.35), are characterized by quantized k and n. The quantized values of k are given by the following equation

$$\tan kN = k/m, \tag{1.36}$$

For future consideration, we introduce a notation $Q(m)$ representing the set of quantized values of k, ranging from 0 to π, which satisfies Eq. (1.36). π, as the bound of quantized k, comes from that we consider unit lattice spacing and discrete space. We will also use the notation $|\psi_{n,k}\rangle$ to represent a single MFT state, which is characterized by quantized k and n.

The other set of Majorana zero-energy boundary modes, which are protected by the topological number of the higher band, cannot be accurately obtained from the first-order expansion of the Hamiltonian (1.33). Instead, one needs to use the exact form of the Hamiltonian, which can give a precise description of the higher-band. Solving $h(-i\partial_x)\psi(x) = 0$, we find two zero-energy wave functions: $\psi_L(x)$ and $\psi_R(x)$, which are protected by the higher-band. The wave functions $\psi_{L,R}(x)$ are localized at left or right boundaries of the system correspondingly. Their analytical expressions read as

$$\psi_L(x) = \sqrt{1-e^{-2/\xi}}e^{-x/\xi}\varphi_L, \quad \psi_R(x) = \sqrt{1-e^{-2/\xi}}e^{-(N-x)/\xi}\varphi_R \tag{1.37}$$

with $\xi^{-1} = \log\frac{2t}{\mu - t_v}$, $\varphi_L = \frac{1}{2}(1,1,-1,-1)^T$ and $\varphi_R = \frac{1}{2i}(1,-1,-1,1)^T$. We remind the reader that ξ^{-1} obtains the complex phase $i\pi$ if $2t/(\mu - t_v) < 0$. We will use the notation $|\psi_{L,R}\rangle$ to represent the corresponding ket (bra) states of these boundary modes. One may see that the expression for ξ here is consistent with ξ_- in Eq.(1.16), which is the localization length derived from the lattice model.

1.5.2 Low-energy effective matrix

Here we introduce the symmetry breaking field B and study the low-energy properties of the TRS broken Hamiltonian. For example, we consider the Model I with the complex vertical pairing potential. We remind that the symmetry breaking term in this Hamiltonian is written in the momentum space as

$$h_B = -B\sigma_x \otimes \tau_y \tag{1.38}$$

with $B = \Delta_v^I$ in this case. We confine our focus on the low-energy sector at the tricriticality. We choose the eigenstates of the parent Hamiltonian as basis states for the low-energy sector: $\{|\psi_{L,R}\rangle, |\psi_{n,k}\rangle | n = \pm, k \in Q(m)\}$, where $Q(m)$ is set

of quantized k-values defined above. In order to represent the full Hamiltonian, $h(-i\partial_x) + h_B$ in this basis, we need to calculate the corresponding matrix elements. Here $h(-i\partial_x)$ yields a diagonal matrix, whose diagonal values are the energies of corresponding modes. Thus, we will focus on the representation of h_B, which yields off-diagonal elements.

Upon calculating all the matrix elements of h_B, we find that only a limited number of off-diagonal matrix elements are non-zero. All possible finite off-diagonal elements are listed below. For the case when MFT-states $|\psi_{n,k}\rangle$ with real quantized k couple to the zero-energy modes $\psi_{L,R}$ via h_B, we have

$$\begin{aligned} \langle\psi_{n,k}|h_B|\psi_L\rangle &= -n\frac{B}{\sqrt{N}}\sqrt{\coth(1/2\xi)}\,|\sin kN|\,, \\ \langle\psi_{n,k}|h_B|\psi_R\rangle &= \frac{B}{i\sqrt{N}}\sqrt{\coth(1/2\xi)}\sin kN, \end{aligned} \tag{1.39}$$

where $|\sin kN|$ means the absolute value of $\sin kN$. In the case with imaginary quantized $k = i\kappa$, one has

$$\begin{aligned} \langle\psi_{n,i\kappa}|h_B|\psi_L\rangle &= -i\sqrt{w}\frac{B}{\sqrt{N}}\sqrt{\coth(1/2\xi)}, \\ \langle\psi^n_{n,i\kappa}|h_B|\psi_R\rangle &= -n\sqrt{w}\frac{B}{\sqrt{N}}\sqrt{\coth(1/2\xi)}. \end{aligned} \tag{1.40}$$

Using the four matrix-elements above, we can calculate the corrections to all single particle energies due to the TRS breaking perturbation. From here one clearly observes the emergence of the scale $g = \alpha(\xi)\sqrt{N}B$, with $\alpha(\xi) = \coth(1/2\xi)$ for Model I. This consideration analytically shows the nature of the scale g, which was extracted numerically from the universal finite-size corrections to the energy.

1.5.3 Evolution of spectrum with the TRS breaking field

One can calculate the eigenvalues of the effective low-energy matrix to obtain the low-energy spectrum of the system. We do this for three different values of $w = Nm$:

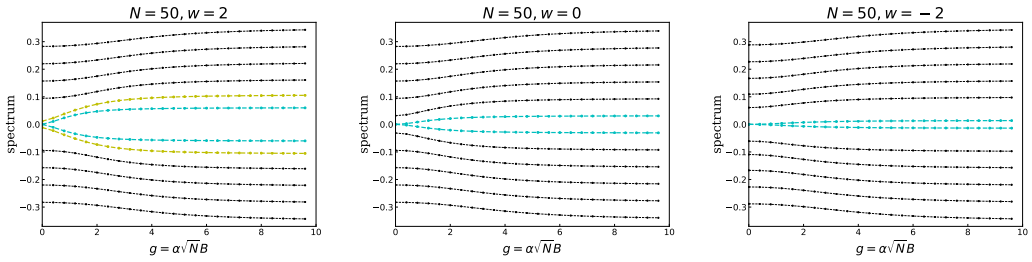

(a) $w = 2$ (4-MF and 0-MF) (b) $w = 0$ (criticality) (c) $w = -2$ (2-MF)

Figure 1.13: (Color online) Several low-lying energy levels of the effective matrix around $E = 0$ plotted as a function of g varying from 0 to 10. Fig. 1.13a depicts the spectrum for $w = 2$. It describes how 4-MF state is smoothly connected to 0-MF state. The evolution of the lowest energy levels, depicted as light gray (blue and yellow) lines, shows how the zero-energy modes merge into the bulk. The bulk energy levels (black lines) also experience change. Fig. 1.13b depicts the spectrum for $w = 0$ (criticality). It shows non-trivial behavior: the edge-modes, shown in light grey (blue), obtain finite energy and finally merge into the bulk. The energy levels of bulk modes deviate from Majorana CFT values when g increases from 0, and then converge to Majorana CFT values when $g \to +\infty$. Fig. 1.13c depicts the spectrum for $w = -2$. The zero-energy modes in 2-MF obtain finite energy, which is proportional to $e^{-\lambda|w|}$, indicating that the localization length of edge modes changes.

(i) At $w = 2$ we trace the topological transition from 4-MF phase (at $g = 0$) to 0-MF phase (at finite g); (ii) At $w = 0$ we trace the topological transition from tricriticality, (at $g = 0$), which represents an example of gapless SPT phase with two boundary Majorana modes, to the trivial critical phase; (iii) At $w = -2$ we trace evolution of the spectrum of the topologically ordered 2-MF phase with the TRS breaking field and show that the localized Majorana modes remain localized even in the presence of finite g. The low-energy spectra of the model in these three situations are shown in Fig. (1.13):

- Fig. (1.13a) describes the evolution of the low-energy spectrum with scale g, when the 4-MF phase smoothly transitions to the 0-MF phase without closing the bulk gap. We clearly observe that four zero-energy modes get gapped and merge into the bulk band. At the same time, the energy levels of bulk modes also acquire a sensitivity to g. We will analyze their g-dependence afterward.

- Fig.(1.13b) describes the evolution of the low-energy spectrum starting from tricriticality at $g = 0$, and upon increasing of g. We see that the zero-energy modes merge into the bulk band, and the energy level of each of the bulk mode is lifted by one "step" up, occupying the spot of the next higher band at $g = 0$. This happens when g increases from 0 to 10.

- Fig. 1.13c describes the g-dependence of the low-energy spectrum of the topologically ordered 2-MF state. Although the topology of 2-MF phase is robust with respect to the TRS breaking perturbation, the spectrum still exhibits some non-trivial behavior. The degeneracy of the zero-energy modes in 2-MF phase is being slightly lifted, but the discrepancy between the states is exponentially small and is proportional to $e^{-|w|}$. In fact, the localization length ξ of the edge modes is changed: if for example we consider the tricriticality corresponding to the upper tricritical point if the phase diagram 1.5a (which has the coordinates $(0, 1)$ in that diagram), then ξ changes from $\xi_-(g = 0)$ to $\xi_+(g = \infty)$. We note that $g = 0$ when the TRS is preserved ($B = 0$), while $g \to \infty$ is achieved at the thermodynamic limit when the system size is $N \gg 1/(\alpha B)^2$).

In Sect.(1.5.1) we considered the low-energy sector at the tricriticality ($g = 0$) and showed it is composed of MFT states, and the zero-energy modes at the tricriticality are protected by the higher-energy band. Thus the low-energy spectrum at the tricriticality, which is labeled by $E(m, g)$, is given by

$$E(m, 0) = \pm \left\{ 0, \sqrt{m^2 + k^2} | k \in \{Q_1(m) \dots Q_N(m)\} \right\} \tag{1.41}$$

Here we observe that the low-energy spectrum away from tricriticality ($g \to \infty$, or, in practice, $g \gtrsim 10$) is given by

$$E(m, g) = \left\{ \pm\sqrt{m^2 + k^2} | k \in \{Q_1(-m) \dots Q_N(-m)\} \right\}. \tag{1.42}$$

Here the spectral gap, m, around the tricriticality is positive in the 4-MF and 0-MF phase, while m is negative in the 2-MF phase.

From Eq.(1.41) and Eq.(1.42), one can observe that for the same value of m, the set of quantized momenta, k, is reversed ($\{Q_1(m)\dots Q_N(m)\}$ becomes $\{Q_1(-m)\dots Q_N(-m)\}$) when g evolves from 0 to ∞. The fact is supported by the numerically calculated energy spectrum shown in Figs. 1.13a and 1.13c. Although at the criticality $Q(-0) = Q(0)$, Fig. 1.13b still yields a non-trivial interpolation between $E(m = 0, g = 0)$ and $E(m = 0, g = \infty)$, indicating the discussed in Sect. (1.4) non-trivial finite-size scaling effect.

The derivation of the closed analytical expression for the exact spectrum of the effective matrix is tedious since the edge modes $\psi_{L/R}$ couple to all other states. For small $g \ll 1$, one may use the quasiparticle picture at $g = 0$ and apply perturbation theory. We find that the energies of MFT-states corresponding to the bulk $|\psi_{n,k}\rangle$ states, and the edge-modes $|\psi_{L,R}\rangle$, acquire perturbative corrections proportional to powers of the scale g. In the limit $g \ll 1$ and $w = 0$, the energy, ϵ_e, of the edge modes $\psi_{L/R}$ becomes

$$\epsilon_e \approx g^2/N, |w| = 0 \tag{1.43}$$

For the aymptotic region where g and w satisfy $\sqrt{|w|}e^{-|w|} \ll g \ll 1$, ϵ_e is given by

$$\epsilon_e \approx \begin{cases} \frac{\sqrt{2}}{|w|^3} g^2/N & \text{for } w \ll -1 \\ \sqrt{2w}\, g/N & \text{for } w \gg 1 \end{cases} \tag{1.44}$$

At $w \gg 1$, the linearity coefficient $\sqrt{2w} \gg 1$. This implies that the edge modes in 4-MF phase are unstable with respect to the TRS breaking perturbation. On contrary,

at $w \ll -1$, the coefficient $\sqrt{2}/|w|^3 \to 0$, indicating stability of edge modes in the 2-MF phase.

1.5.4 Function at $|w|, g \ll 1$

The ground state energy at $|w| \ll 1$ and $g \ll 1$ is obtained upon performing the summation of energy levels in the occupied band. At $|w| \ll 1$, the quantization of momenta in the MFT yields only bulk modes (and no boundary modes associated with MFT), and the energies of bulk MFT states are $\{\epsilon_l | 0 \leq l \leq N-1\}$. There are, however, two Majorana edge modes protected by the topological index of the higher band. The energies of these edge modes (defined as $\psi_{L/R}$ in the previous section) are defined as $\pm\epsilon_e$. The ground state energy of the system will thus read

$$E_G = -\frac{1}{2}\epsilon_e - \frac{1}{2}\sum_{l\geq 0}\epsilon_l. \tag{1.45}$$

This expression can further be simplified by rewriting the summation in the ground state energy (both, the summation in ϵ_e and the summation over l in Eq. (1.45)) via a Cauchy contour integral,

$$E_G = -\frac{1}{4}\oint_C \frac{dk}{2\pi i}[E_{m,g}(k)q_+(k) + E_{m,0}(k)q_-(k)]. \tag{1.46}$$

Here $q_\pm(k) = \partial_k \ln(\cos\frac{1}{2}(Nk+\delta_m)\pm\frac{\pi}{4})$, $\tan\delta_m = k/m$, $E_{m,g}(k) \approx \sqrt{m^2+k^2+8g^2/N^2}$ (since here $|w| \ll 1$). The contour C encircles all poles of $q_\pm(k)$ in the complex plane, but it avoids the branch cut line of $E(m,g)$ along the complex line $z = ix$ with $x \geq \sqrt{m^2+8g^2/N^2}$.

Upon taking the derivative of $q_\pm(k)$, one can obtain the bulk energy, $N\epsilon$, and the boundary energy, b, as follows:

$$
\begin{aligned}
N\epsilon &= \int_{-\pi}^{\pi} \frac{dk}{2\pi}[E_{m,g}(k) + E_{m,0}(k)]N/4 \\
b &= \int_{-\pi}^{\pi} \frac{dk}{2\pi}[E_{m,g}(k) + E_{m,0}(k)]\partial_k \delta_m/4.
\end{aligned} \tag{1.47}
$$

Then the combination $E_G - N\epsilon - b$ is the energy responsible for finite size corrections to the ground state energy, $-f/N$. After performing a contour integration, we find the finite size scaling function, $f(w, g)$, given by the following integral:

$$
\begin{aligned}
f(w,g) &= -\int_{\sqrt{8g^2+w^2}}^{\infty} \frac{dz}{2\pi} E_{w,g}(z)\partial_z \ln(1 + e^{-2z-2\delta_w(z)}) \\
&- \int_{w}^{\infty} \frac{dz}{2\pi} E_{w,0}(z)\partial_z \ln(1 + e^{-2z-2\delta_w(z)}).
\end{aligned} \tag{1.48}
$$

So, we see that $f(w, g)$ is a function of w and g. One can evaluate this integral at $w = 0$ and $g \ll 1$, yielding the following asymptote

$$
f(0, g) - f(0, 0) \simeq \frac{1}{\sqrt{\pi}} g^2 \log g, \tag{1.49}
$$

where $f(0, 0) = \pi/24$.

1.6 The Hamiltonion and boundary entropy

In this section, we work out the second quantized formalism for the low energy Hamiltonian at criticality. We show that the boundary entropy is a universal function of the scale g for Models I, II, III.

1.6.1 The low-energy Hamiltonian

In second quantization, for the MFT modes, $\psi_{n,k}$ and $\psi_{L/R}$ given by Eq.(1.37), one defines the corresponding quasiparticle operators, $\hat{\psi}_{n,k}$ and $\hat{\psi}_{\mathrm{L/R}}$. The particle-hole symmetry of the theory is reflected in the following property of $\hat{\psi}_{n,k}$: $\hat{\psi}^{\dagger}_{+,k} = \hat{\psi}_{-,k}$.

Thus, we only keep one operator with positive energy, $\hat{\psi}_k \equiv \hat{\psi}_{n,k}$. We remind that $\hat{\psi}_{\rm L}$ and $\hat{\psi}_{\rm L}$ are two localized Majorana fermion operators: $\hat{\psi}_{\rm L}^\dagger = \hat{\psi}_{\rm L}$ and $\hat{\psi}_{\rm R}^\dagger = \hat{\psi}_{\rm R}$.

Consider the effective matrix corresponding to the Model I at the criticality ($m = 0$), see Sec.(1.5). The corresponding low-energy Hamiltonian is given by

$$H = \sum_{k \in Q(0)} k \hat{\psi}_k^\dagger \hat{\psi}_k + \frac{\alpha(\xi) B}{\sqrt{N}} \left(\hat{\psi}_k - \hat{\psi}_k^\dagger \right) \hat{\psi}_{\rm L} + \sin(kN) \cdot \frac{\alpha(\xi) B}{\sqrt{N}} \frac{\hat{\psi}_k + \hat{\psi}_k^\dagger}{i} \hat{\psi}_{\rm R} \quad (1.50)$$

where $Q(0) \equiv \{\pi/2N + m\pi/N | m = 0, 1, \ldots, N-1\}$. Here the upper bound for m is $N-1$, since the lattice spacing is chosen to be unity.

In the continuum limit, when the lattice spacing $a \to 0$, the Hamiltonian above becomes equivalent to

$$\begin{aligned} H &= \frac{1}{2} \int_{-\infty}^{+\infty} dx \begin{pmatrix} \hat{\psi}_c^\dagger(x) & \hat{\psi}_c(x) \end{pmatrix} (m(x)\sigma_z - i\sigma_y \partial_x) \begin{pmatrix} \hat{\psi}_c(x) \\ \hat{\psi}_c^\dagger(x) \end{pmatrix} \\ &+ \frac{\alpha(\xi) B}{\sqrt{2}} \left(i \left[\hat{\psi}_c^\dagger(0) + \hat{\psi}_c(0) \right] \hat{\psi}_{\rm L} + \left[\hat{\psi}_c^\dagger(N) - \hat{\psi}_c(N) \right] \hat{\psi}_{\rm R} \right). \end{aligned} \quad (1.51)$$

Here $\hat{\psi}_c(x)$ is the generic spinless fermion annihilation operator at continuous space coordinate x, satisfying $\{\hat{\psi}_c(x), \hat{\psi}_c^\dagger(x')\} = \delta(x - x')$. Operators $\hat{\psi}_{\rm L/R}$ correspond to two localized Majorana fermion operators, satisfying $2\hat{\psi}_{\rm L/R}^2 = 1$, and the mass term, $m(x)$, is given by

$$m(x) = \begin{cases} 0 & 0 < x < N \\ +\infty & x < 0, x > N \end{cases}$$

From Eq.(1.51), one may formulate the corresponding action and conclude that $\alpha(\xi)B$ drives the boundary RG flow from the bulk Ising criticality with two localized Majorana boundary modes (gapless SPT phase) to the bulk Ising criticality without localized Majorana boundary modes (gapless trivial phase). Scaling dimension of $\alpha(\xi)B$ is $1/2$ so the dimensionless $g = \alpha(\xi)\sqrt{N}B$ emerges as invariant scale under

RG flow. The Hamiltonian in Eq.(1.51) is consistent with the action proposed in the literature[51, 52], which is used to describe the boundary Ising chain. In the model of boundary Ising chain , boundary magnetic field drives the RG flow from free boundary condition[53, 54] to fixed boundary condition.

1.6.2 The boundary entropy

The boundary entropy is defined by the logarithm of universal non-integer degeneracy[47], which only depends on the universality class of the conformally invariant boundary condition[53, 54]. In practice, one can obtain the boundary entropy via calculating the Von-Neumann entropy[55]. Given the system defined on an interval M, one can partition it into two subsystems consisting of two intervals, A and B. Von-Neumann entropy measures the entanglement between two subsystems. Let ρ be the density matrix of system M and $\rho_A := \mathrm{tr}_B \rho$ is the reduced density matrix of A. Von-Neumann entropy is then defined as $S = -\mathrm{tr}_A \rho_A \log \rho_A$. In the following, we will focus on the system with boundaries: $M = (0, N)$, $A = (0, l)$ and $B = (l, N)$.

For critical lines around the tricriticality, we find that the von-Neumann entropy is given by

$$S = \frac{c}{6} \log(2l) + c_1/2 + S_B(\alpha B \sqrt{l}) \tag{1.52}$$

where c_1 is non-universal constant and $S_B(\alpha B\sqrt{l})$ is the boundary entropy. We show that $S_B(\alpha B\sqrt{l})$ is universal for Models I, II, III and the low-energy Hamiltonian Eq.(1.51). It is depicted in Fig.(1.14). This result is consistent with that reported in the literature on the universal flow of boundary entropy[56, 57, 51].

1.7 Conclusions

In this chapter, we report the existence of quantum tricriticality in Models I, II, and III, which separates topologically ordered, SPT, and trivial phases of the

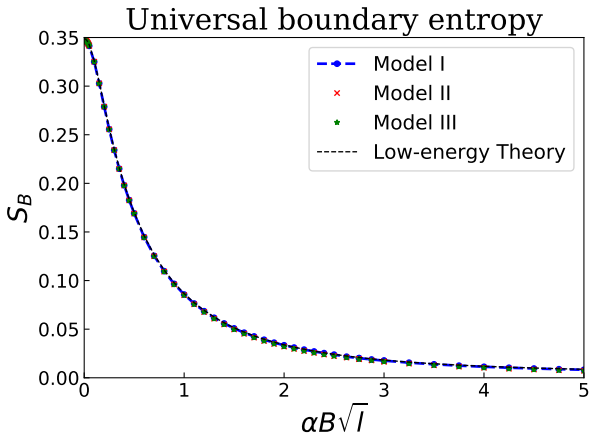

Figure 1.14: (Color online) Boundary entropies of Models I, II, III and the low-energy effective Hamiltonian Eqs.(1.50) and Eq.(1.51). All curves fall into same universal curve representing the universal boundary entropy.

system. We study the finite size corrections to the ground state energy and find that it is a universal function of a new dimensionless scale, $g = \alpha\sqrt{N}B$, where B is the symmetry-breaking field. Thus, around the tricriticality, the finite size corrections are determined by two variables, $w = Nm$, and g. We derive the effective low-energy theory corresponding to these models and show the emergence of the scale g that describes the evolution of the low-energy spectrum with B. We analytically calculate the asymptotes of the universal finite-size scaling function, $f(w, g)$. Finally, we show that the scale g emerges in the boundary entropy, which is shown to be universal for three models.

We conjecture that the universal finite-size double-scaling function should emerge not only for coupled Majorana chains considered in this work, but also for other models which support SPT, topologically ordered, and trivial phases. In the free fermion classification[14, 35, 36], only Majorana chains can support such phases. However, one may find such tricriticalities in interacting models, including the spin chains, which are beyond the free fermion classification. For example it is interesting to investigate the finite size effects in critical spin chains perturbed by a TRS breaking scalar

chirality operator[58, 59]. The tricriticality may also exist in interacting Majorana chains [19, 60, 61, 62, 63, 17],since 4-MF and 2-MF are both stable in the presence of interactions, which preserve the time-reversal symmetry and fermion-parity symmetry. The behavior of finite-size scaling function in interacting systems, including the spin chains and higher dimensional systems with TRS breaking is beyond the scope of the section, and is left for future studies.

CHAPTER 2

ABSENCE OF CONFORMAL SYMMETRY: THE $z = 2$ QUANTUM LIFSHITZ CRITICALITIES IN TOPOLOGICAL CHAINS

The text of this chapter has been adapted from Ref [64].

2.1 Introduction

A class of criticalities separate gapped symmetry protected phases[17, 18, 15] (SPTs) and topologically trivial ones. At these criticalities usually the system disperses linearly, $\epsilon = \pm v_F k$, around the Fermi surface, and the low-energy effective physics is described by conformal field theories[1, 3, 46] (CFTs). Several universal features characterize conformal critical points. One notable feature for quantum one-dimensional (1D) systems is the universal finite-size amplitude[2] together with the emergence of the universal characteristic of CFTs, the central charge, c. Namely, the finite-size correction to the ground state energy $E(L)$, e.g., in case of open boundary condition (b.c), always contains a universal term $c\pi/24L$. The other universal feature is the logarithmic entanglement entropy[65], e.g. , $S \sim c\ln(L)/6$ in the case of periodic b.c.

Topologically distinct and gapped phases are reached by adding the mass to the CFT criticalities[66]. A simple example is the hamiltonian $h(i\partial_x) = v_F\sigma_y i\partial_x + m\sigma_x$ and sign(m) is an integer to distinguish phases. Here $\sigma_{x,y}$ are Pauli matrices. Universal features also appear around the topological phase transitions[33], e.g., the finite-size correction emerges as a universal function of scale, $\omega = mL$.

Recently, it has been observed that CFT critical phases can have non-trivial topology and host boundary modes. Such criticalities are dubbed symmetry-enriched criticalities[67, 68, 69] or called gapless SPTs[70, 49]. At the transition between two symmetry-enriched CFTs, non-CFT criticalities can emerge[71]. The simplest case is the Lifshitz criticality[72, 73, 74, 75, 76, 77, 78] with dynamical exponent $z = 2$. Its role as a criticality between gapless SPTs is similar to CFT critical points separating gapped SPTs. Namely, one can reach topologically distinct gapless phases by adding velocity term v to $z = 2$ critical point. A simple Hamiltonian illustrates this fact,

$$h(-i\partial_x) = v\sigma_y(i\partial_x) + u\sigma_x\partial_x^2. \tag{2.1}$$

Here v is the velocity, and u is the curvature of the spectrum. The case with $v = 0$ corresponds to a non-CFT criticality, referred to as Π throughout this chapter. With appropriate boundary conditions, one can find the eigenstate, $\psi(x)$, of the Hamiltonian Eq. 2.1, exhibiting boundary modes at $\mathrm{sign}(v) > 0$ which however disappear at $\mathrm{sign}(v) < 0$. Thus, adding velocity perturbations to the $z = 2$ criticality generates two gapless phases: one topologically trivial and another non-trivial. This finding is supported by the detailed calculation in the Sec. 4.4.

In spite of its fundamental role of describing transitions between symmetry-enriched CFTs, the understanding of universal features of $z = 2$ critical points (with the dispersion $\epsilon \sim \pm k^2$) is still lacking. In this chapter, we aim to understand the universal properties of Π criticality from two aspects: the study of the energy and entanglement entropy of the ground state. To this end, we consider two concrete lattice models and develop the low energy field theoretical description of the criticality. Lattice models considered below are Majorana/Kitaev chains[14, 71] with next-nearest neighbor terms from BDI symmetry class[34, 14, 35, 36] and the generalized Su-Schrieffer–Heeger (SSH) model[23, 79] with next-next-nearest neighbor terms belonging to the AIII symmetry class.

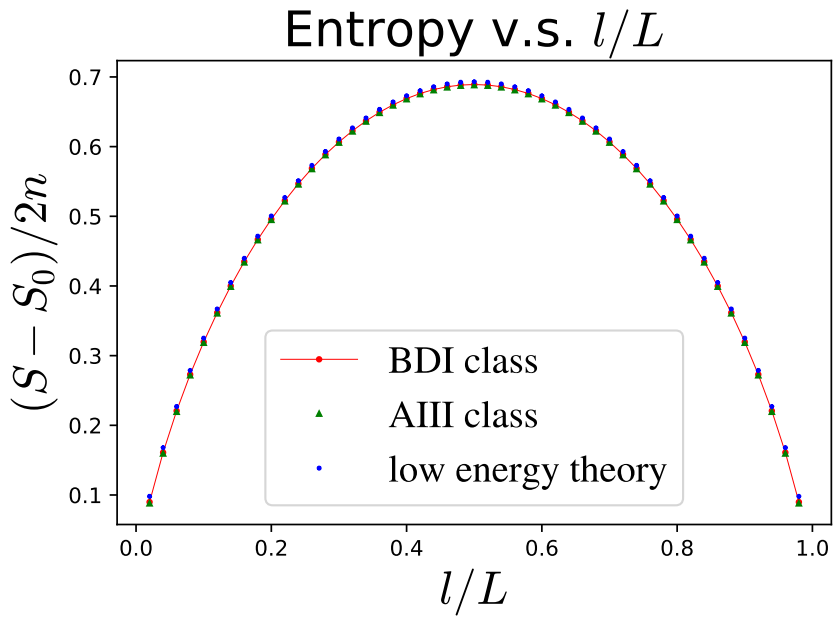

Figure 2.1: (Color online) Entanglement entropy $(S - S_0)/2n$ is plotted versus l/L. Here S_0 is the non-universal constant entropy, l is the size of subsystem, $n = 1/2$ for the Majorana chain in BDI class and $n = 1$ for the SSH model in AIII class. Three sets of data, including entropy of the Majorana chain, SSH model, and low energy theory, all fall into the same *universal* curve. The function, representing the plotted curve, is exactly the l/L-dependent term in Eq. 2.3.

The first result of the present chapter corresponds to the ground state energy $E(L)$ as a function of the system size, L. At open boundary condition, the finite-size corrections[80, 81, 82] to $E(L)$ exhibit a universal behavior and read

$$E(L) = L\epsilon + b - nu\frac{J}{L^2} + O(L^{-3}), \tag{2.2}$$

Here ϵ is average bulk energy, b is the boundary energy, and $n \in \mathbb{Z}^+/2$ depends on degrees of freedom of the underlying field theory: $n = 1/2$ for the Majorana chain and $n = 1$ for the SSH model under consideration. The amplitude J is $J \simeq 0.887984$, which is universal for two lattice models and the low-energy field theory giving the same value. This indicates a possible set of rich phenomena of finite-size scaling functions around this criticality[33, 83, 84]. We have checked that velocity perturbations modify A into a universal scaling function of $\omega = Lv$, and the function is sensitive to the topological nature of CFTs.

We also find that the entanglement entropy[65] exhibits an interesting dependence on l/L. At periodic b.c, the von Neumann entropy of the maximally-entangled ground state is given by

$$S \simeq S_0 + 2n \cdot \left[\frac{l}{L}\ln\left(\frac{L}{l} - 1\right) - \ln\left(1 - \frac{l}{L}\right)\right]. \tag{2.3}$$

Here l is the length of the subsystem, and S_0 is a non-universal constant. At the limit $l/L \ll 1$, S has a simple asymptote $\sim (l/L)\log(l/L)$, which is non-logarithmic. The l/L-dependent term is found to be universal, plotted in Fig. 2.1. Below we start with a definition of lattice models and observe the emergence of Π criticality.

2.2 Lattice models and criticality

We consider two concrete one-dimensional lattice models supporting the Lifshitz Π criticality. One is the Majorana chain, containing both nearest site and next-nearest

site hoppings and pairings. The Hamiltonian is given by

$$H_{\text{Majorana}} = \sum_n t_0 \tilde{\gamma}_n \gamma_n + t_1 \tilde{\gamma}_n \gamma_{n+1} + t_2 \tilde{\gamma}_n \gamma_{n+2}. \tag{2.4}$$

Here $\{\gamma_n, \tilde{\gamma}_n\}$ are two Majorana fermions at the same physical site, and constants $t_i \in \mathbb{R}$, with $i = 0, 1, 2$. The model is schematically shown in Fig. 2.2a. Note that the model belongs to the BDI class of Cartan's classification of symmetric spaces. A critical line of the model, where the gap closes, corresponds to the case $t_2 + t_0 = t_1$. One can observe three distinct critical behaviors in this situation: (1) when $0 < t_2/t_1 < 1/2$, the low-energy sector is described by Majorana CFT and two localized Majorana modes. (2) When $1 > t_2/t_1 > 1/2$, the low-energy description is a single Majorana CFT. (3) At $t_2 = t_0 = t_1/2$, the Π criticality emerges around $k = \pi$ in the Brillouin zone. The Hamiltonian around the Fermi surface, in Bogoliubov-de-Gennes (BdG) formalism, can be written as

$$H_{\text{FS}} = u \int dx \Psi^\dagger(x) \sigma_x \partial_x^2 \Psi(x). \tag{2.5}$$

Here $\Psi(x) = (\psi(x), \psi^\dagger(x))^T$ and $\psi(x)$ is the spinless fermion operator in the continuous space.

The second model under consideration is the generalized SSH model belonging to the AIII symmetry class. The model is schematically shown in Fig. 2.2b. The Hamiltonian includes nearest-neighbor and next-next-nearest neighbor hoppings of fermions $c(^\dagger)$ and is given by

$$H_{\text{ssh}} = \quad \sum_n u_0 c^\dagger_{n,A} c_{n,B} + \sum_{i=1,2} u_i c^\dagger_{n,B} c_{n+i,A} + h.c. \tag{2.6}$$

The model is defined on a bipartite lattice with A and B sublattices and real hopping parameters. It has a similar phase diagram as the model of Majorana chains identified

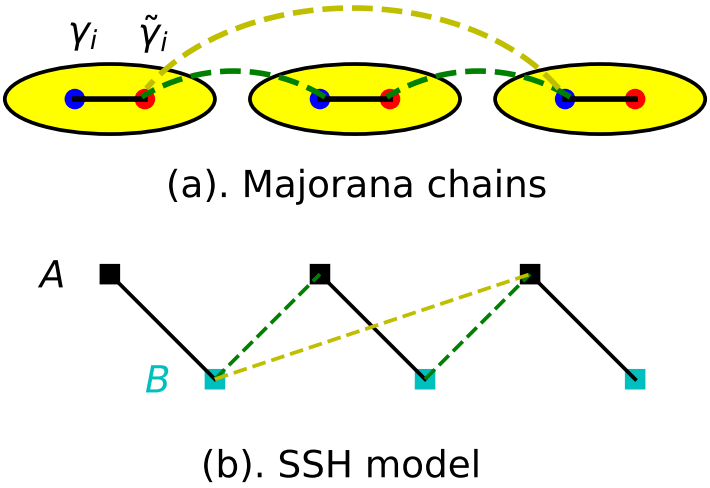

Figure 2.2: (Color online) Models with three unit cells are plotted to illustrate the hoppings and pairings. (a) Majorana chain. A single fermion is decomposed into two Majorana fermions, shown as blue and red dots. Black lines represent t_0 and dashed green/yellow lines represents t_1/t_2 hoppings (and pairings) in Eq. 3.9. (b) SSH model. Black/cyan rectangular dots represent A/B sublattices. Black, green and yellow lines represent u_0, u_1 and u_2 hoppings in Eq. 2.6.

above. Here the criticality Π emerges around $k = \pi$ when $u_0 = u_2 = u_1/2$. Now the Hamiltonian around the Fermi surface is described by Eq. 2.5 but with $\Psi(x) = (\psi_A(x), \psi_B(x))$.

Below, we will identify a set of universal properties inherent for theories at Π criticality and present the low-energy field theory description of the system yielding these universal properties.

2.3 Universal finite-size amplitude

The present section studies the finite-size correction to the ground state energy, $E(L)$, of the system at open boundary conditions at criticality Π.

In the lattice models under consideration, the computation of the finite-size amplitude of the ground state is similar to the method used in references[33], that was applied to CFT criticalities. The method has an error bar, $\sim L^{-1}$. Here we report the results for the SSH model and Majorana chain: we pick $L = 500$ and A is found to

be 0.88441 for the SSH model and 0.88440 for the Majorana chain. Compared to the value of A below Eq. 2.2, errors are at the expected order, $\sim 10^{-3}$. The amplitude A is universal because it originates from the long-wavelength degrees of freedom around the Fermi surface. Below, we will validate this point by deriving the amplitude A from the low energy theory.

2.3.1 Quantization condition

Consider the Hamiltonian Eq. 2.1 at $v = 0$. One special property of the operator $\sigma_x \partial_x^2$ is that the free wave and the bound states can belong to the same subspace of it. Namely, the eigenstates are $\psi_k(x) = \exp(ikx) \cdot \chi_-$ and $\psi_{ik}(x) = \exp(-kx) \cdot \chi_+$, which lie in the same energy level $\epsilon_k = uk^2$. Here $\chi_\pm$ satisfy $\sigma_x \chi_\pm = \pm\chi_\pm$ and $k \in (-\pi, \pi)$.

Now assume $h(-i\partial_x)$ acts on coordinate dependent wavefunctions with $x \in (0, L)$ and we impose open boundary conditions on wavefunctions. Namely, one has $\psi_1(0) = \partial_x \psi_1(0) = 0$ corresponding to the "left" boundary, and $\psi_2(L) = \partial_x \psi_2(L) = 0$ corresponding to the "right" boundary. These conditions describe the continuity of the wavefunction around boundaries, when one imposes the infinite velocity outside the segment $(0, L)$. Note that the wavefunction with the energy ϵ_k can be generally written as $\varphi_k(x) = \sum_{s=\pm} a_s \psi_{sk}(x) + b_s \psi_{isk}(x)$. Upon searching for solutions $\varphi_k(x)$, which obey the open boundary conditions, one arrives at the quantization condition (QC) of the momentum,

$$\cos kL + 1/\cosh kL = 0, \quad 0 < k < \pi, \tag{2.7}$$

different from conventional QC of Ising CFTs (that being $\cos kL = 0$). When $kL \gg 1$ in Eq. 2.7, the difference between the abovementioned QCs is exponentially small. However, when $kL \sim 1$, the difference is not negligible anymore. This difference indicates that there could be non-trivial finite-size effects. Solutions to Eq. 2.7 are shown in Fig. 2.3.

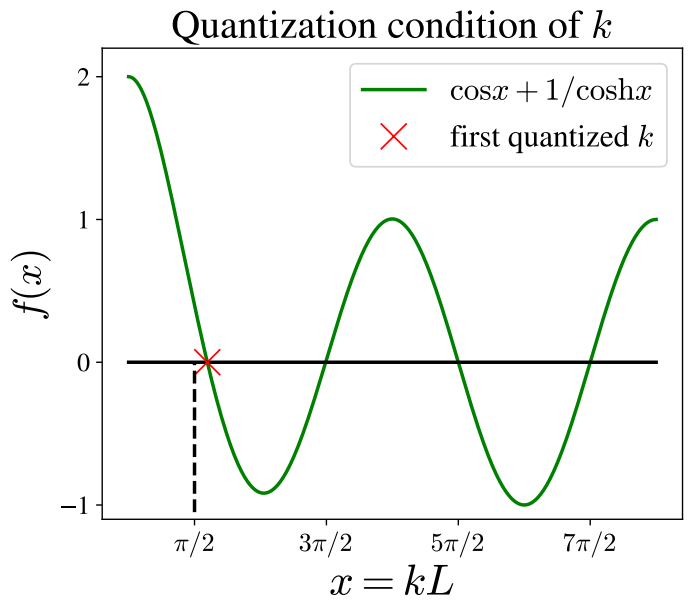

Figure 2.3: (Color online) Plot of the quantization condition in Eq. 2.7. The green curve plots the function $f(x) = \cos x + 1/\cosh x$ with $x = kL$. Intersections between $f(x)$ and x-axis determine quantized values of k. The first quantized value, located around $x_0 \simeq 1.875$, is marked by a red cross. This value deviate from the first quantized value in Ising CFT, $\pi/2$. Quanlitatively, the order of the amplitude J can be aruged from this deviation: the deviation in the spectrum level is given by $x_0^2 - (\pi/2)^2 \sim 1$, which is the order of J.

2.3.2 Ground state energy

To compute the ground state energy, one must perform summation over all the quasi-particle energies below the Fermi surface. Namely, $E(L) = -u \sum_{k \in \mathrm{QC}} k^2$. Note that all quantized solutions k of Eq. 2.7 are invovled in the ground state energy. Summation in $E(L)$ can be written as a contour integral. Defining $z = kL$, $f(z) = \cos z + 1/\cosh z$ and taking the analytical continuation of $f(z)$, one finds

$$E(L) = -\frac{1}{2L^2} \oint_C \frac{dz}{2\pi i} z^2 \partial_z \ln f(z). \tag{2.8}$$

Here C is the contour in complex plane $z = x + iy$, shown in Fig. 2.4.

$$E_{G.S.} = -\frac{1}{2L^2} \oint_C \frac{dz}{2\pi i} z^2 \partial_z \ln \Big(\frac{e^{iz} + e^{-iz}}{2} + \frac{2}{e^z + e^{-z}} \Big). \tag{2.9}$$

Now let us consider the upper part of the contour, $C^+ = (i\delta, +2\pi L + i\delta)$, in the complex space of the integration variable z. The contribution to the $E_{G.S.}$ that corresponds to this upper part of the contour can be decomposed into

$$E_+ \;=\; -\frac{1}{2L^2} \int_{i\delta}^{2\pi L + i\delta} \frac{dz}{2\pi i} z^2 \partial_z \Big\{ \ln e^{-iz} + \ln \Big(\frac{e^{2iz} + 1}{2} + \frac{2e^{iz}}{e^z + e^{-z}} \Big) \Big\}. \tag{2.10}$$

The first term in the integral gives $(2\pi)^2/3L$, which is exactly the bulk energy. Thus, the finite size effect comes from the second term.

2.3.3 Finite-size amplitude

We single out the finite-size contribution from E_+ and find that it is given by

$$J_+ \equiv \int_{i\delta}^{4\pi L + i\delta} \frac{dz}{2\pi i} z^2 \partial_z \ln \Big(\frac{e^{2iz} + 1}{2} + \frac{2e^{iz}}{e^z + e^{-z}} \Big). \tag{2.11}$$

Since the integrand at the arc is exponentially small, one could deform the contour into the form shoun by the (red) dashed line in Fig.2.4. Also, we define a new variable $z = x\alpha$ with $\alpha = e^{i\pi/4}$ and rewrite J_+ as

$$J_+ = -\int_0^{+\infty} \frac{dx}{4\pi} x^2 \partial_x \ln\Big(\frac{e^{2ix\alpha}+1}{2} + \frac{2}{e^{\sqrt{2}x} + e^{-i\sqrt{2}x}}\Big). \tag{2.12}$$

Here $\alpha = e^{i\pi/4}$. The " $-$ " sign emerges due to the deformation of the contour. Upon rescaling x by $x \to \sqrt{2}x$, one obtains

$$J_+ = -\int_0^{+\infty} \frac{dx}{8\pi} x^2 \partial_x \ln\Big(\frac{e^{(i-1)x}+1}{2} + \frac{2}{e^{x} + e^{-ix}}\Big). \tag{2.13}$$

Note there are also finite-size contributions coming from the other three segments, namely $(-i\delta, +2\pi L - i\delta)$ and $(\pm i\delta, -2\pi L \pm i\delta)$. All contributions add to the expression below,

$$J = -\mathrm{Re}\int_0^{+\infty} \frac{x^2 dx}{\pi} \frac{\frac{1}{2}(i-1)(e^{-x}+e^{ix}) - 2(e^x + e^{-ix})^{-1}(e^x - ie^{-ix})}{\cos x + \cosh x + 2} \tag{2.14}$$

Then one can take the real part of the integral and arrive at the following expression

$$J = \int_0^{+\infty} \frac{x^2 dx}{2\pi} \frac{1}{\cos x + \cosh x + 2}\left(e^{-x} + \cos x + \sin x + 4\frac{1 + (\cos x - \sin x)e^{-x}}{1 + 2\cos x e^{-x} + e^{-2x}}\right)$$

One can numerically evaluate the convergent integral over the single real-variable, x, and obtain the numerical value of the amplitude, J.

This analytically found constant matches the value of J presented below Eq. 2.2. The value of n can also be argued from the low-energy sector: $n = 1/2$ for BDI class is due to the property that the operator $\Psi(x) = (\psi(x), \psi^\dagger(x))^T$ is counted as $1/2$ degree of freedom, while $n = 1$ for AIII class is due to the fact that $\Psi(x) = (\psi_A(x), \psi_B(x))^T$ can be counted as 1 degree of freedom. In this way, we proved the Eq. 2.2.

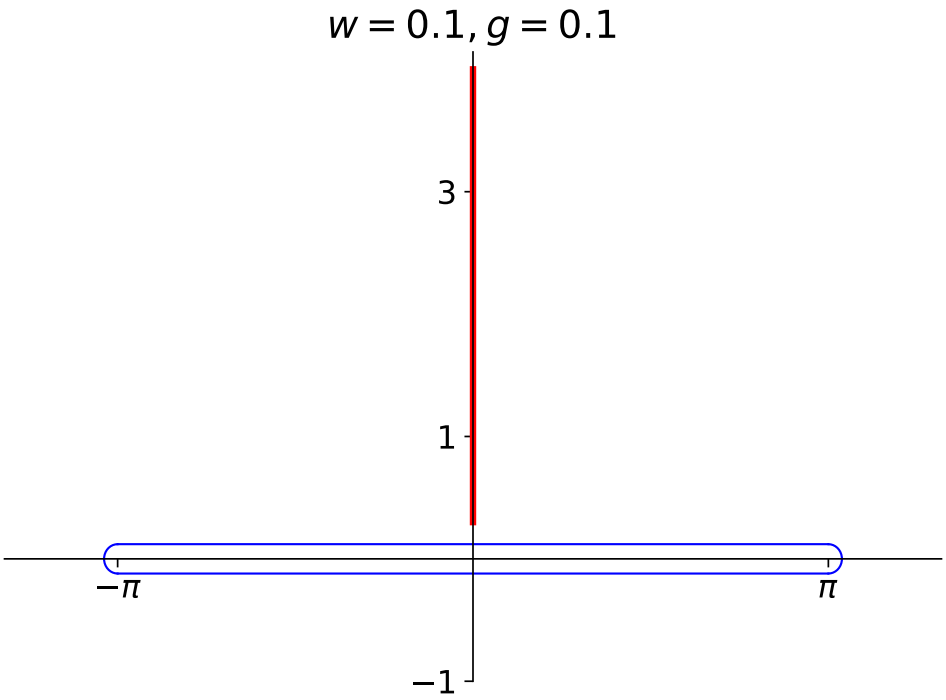

Figure 2.4: (Color online) Contours of integration. The blue contour C corresponds to Eq. 5.17. One can deform the contour C to D (the red lines), since the integrand on the arc (the black line) is exponentially small and the function $\ln f(z)$ is holomorphic when $\mathrm{Re}(z) \neq 0$ and $\mathrm{Im}(z) \neq 0$.

2.4 Anomalous entanglement entropy

The other universal data, which can be extracted from the Hamiltonian, is the entanglement entropy S. Below we take the Majorana chain as an example to illustrate the emergence of the anomalous entanglement. The consideration for the SSH model is similar.

At first glance, one may observe the eigenstates of Eq. 2.5 are not different from those of the gapped Hamiltonian (where one replaces $k^2 \to m$ and $m \neq 0$). Thus one expects short-ranged correlations and constant (non-universal) entanglement entropy, known as features of a gapped 1D quantum system. However, the presence of zero-modes at the Fermi surface changes the situation. With periodic boundary conditions, the $k = 0$ eigenstate leads to the double degeneracy of the ground state. Tracing the maximally-entangled ground state, we find that the asymptotic correlation function is given by

$$\langle \eta_\alpha(x)\eta_\beta(y)\rangle \simeq \epsilon^{\alpha,\beta}\frac{2i}{L}e^{ik_F(x-y)}, \quad \text{when } |x-y| \gg 1 \text{ and } \alpha,\beta = 1,2. \tag{2.15}$$

Here we relabeled the Majorana fermions $\eta_1(x) = \gamma_x$ and $\eta_2(x) = \tilde{\gamma}_x$ for the convenience, $\epsilon^{\alpha,\beta}$ is rank-2 anti-symmetric tensor, L is the size of the system, $k_F = \pi$ is the Fermi momentum. So this L-dependent long-range correlation originates from $k = 0$ zero modes at the Fermi surface. For free fermions, the correlation function encodes the information of entanglment spectrum[85, 86]. It is reflected by a simple fact, $\langle \eta_\alpha(x)\eta_\beta(y)\rangle = \mathrm{tr}(\eta_\alpha(x)\eta_\beta(y)\rho_O)$. Here O is a subsystem and $x, y \in O$.

To find entanglement entropy, one has to find all eigenvalues of the correlation matrix, $\langle \eta_\alpha(x)\eta_\beta(y)\rangle$, with the subsystem of length l. Here from the long-range correlation in Eq. 2.15, we find that there is only one non-trivial eigenvalue that has the form $|1 - (2l/L)|$. One can obtain the corresponding value in the entanglement spectrum via solving $\tanh(\epsilon_0/2) = |1 - (2l/L)|$. This gives $\epsilon_0 = \log(L/l - 1)$. Subsequently, the ϵ_0 results in the non-trivial entropy in Eq. 2.3. At the limit $l/L \ll 1$,

the asymptotic expression of S is $\sim l/L \log(l/L)$. The form is highly-nontrivial, as it is a non-logarithmic function. But its magnitude is weaker than a pure logrithmic function[87]. Below we give a detailed derivation of the entanglement entropy.

2.4.1 Correlation function

Without losing generality, we start from a rotated Hamiltonian given by $H = \int_0^L dx \Psi^\dagger(x) \partial_x^2 \sigma_z \Psi(x)$. For BDI symmetry class, $\Psi(x) = [\psi(x), \psi^\dagger(x)]$. Under the periodic boundary conditions, the eigenstates are simply free wavefunctions. They can be cast in the form

$$\varphi_k(x) = \frac{1}{\sqrt{L}} e^{ikx}(0, 1). \tag{2.16}$$

Thus the quasi-particle operator is given by

$$\hat{\varphi}_k = \frac{1}{\sqrt{L}} \sum_x e^{ikx} \psi^\dagger(x) = \frac{1}{2\sqrt{L}} \sum_x e^{ikx} [\eta_1(x) - i\eta_2(x)]. \tag{2.17}$$

As usual, we decomposed the fermion operator into Majorana fermions $\psi(x) = \frac{1}{2}[\eta_1(x) + i\eta_2(x)]$. Thus one can find that the Majorana operators diagonalizing the system are given by

$$b_k^1 = \frac{1}{\sqrt{L}} \sum_x (\eta_1(x) \cos kx + \eta_2(x) \sin kx) \tag{2.18}$$

$$b_k^2 = \frac{1}{\sqrt{L}} \sum_x (\eta_1(x) \sin kx - \eta_2(x) \cos kx) \tag{2.19}$$

With the diagonalizing Majorana fermions, one can evaluate the correlation function of η-Majorana fermions,

$$\langle \eta_\alpha(x_i) \eta_\beta(x_j) \rangle = I + \frac{i}{L} \sum_m \begin{pmatrix} -\sin k_m(x_i - x_j) & -\cos k_m(x_i - x_j) \\ \cos k_m(x_i - x_j) & -\sin k_m(x_i - x_j), \end{pmatrix} \tag{2.20}$$

where summation over $m \in \mathbb{Z}$ has to be performed. This can be done for diagonal and off-diagonal independently as follows:

- For the diagonal matrix element one obtains a Kronecker δ upon switching to integration:

$$\langle \eta_1(x_i)\eta_1(x_j)\rangle \simeq i\delta_{i,j} - \frac{i}{2\pi}\int_{-\pi}^{\pi} dk \sin k(x_i - x_j) \simeq i\delta_{i,j}. \tag{2.21}$$

- Then we compute the non-diagonal correlators:

$$\langle \eta_1(x_i)\eta_2(x_j)\rangle \;\; = \;\; -\frac{i}{2\pi}\int_{-\pi}^{\pi} dk \cos k(x_i - x_j) = -i\delta_{i,j}. \tag{2.22}$$

The conclusion is that

$$\langle \eta_1(x_i)\eta_1(x_j)\rangle \simeq i\delta_{i,j}, \quad \langle \eta_1(x_i)\eta_2(x_j)\rangle \simeq -i\delta_{i,j}. \tag{2.23}$$

The absence of the $\sim 1/x$ decaying correlation, as opposed to the Ising CFT, is because the degeneracy here is rather trivial. Namely, φ_k and φ_{-k} share the same vector part, namely $(0, 1)$. Recall that the degeneracy of k and $-k$ in CFT is non-trivial: the vector parts of φ_k and φ_{-k} are two different eigenstates of σ_z.

Up to now, the correlation looked like the massive ones. Now we uncover a straightforward fact that there exists zero-mode, defined by

$$\hat{\chi}_0 = \frac{1}{\sqrt{L}}\sum_x \psi(x) = \frac{1}{2\sqrt{L}}\sum_x [\eta_1(x) + i\eta_2(x)]. \tag{2.24}$$

This zero-mode is *not* considered in the previous ground state. In the BDI class, the ground state is double degenerate. We define the first ground state $|GS\rangle_0$ to be

$$\hat{\psi}_k|GS\rangle_0 = 0, \quad k \in (-\pi, \pi) \tag{2.25}$$

In fact, this ground state is rather trivial. It is simply the vacuum state of the field operators $\psi(x)$. From the redundancy description, this ground state is simply filling the negative band. Now we define the second ground state as

$$|GS\rangle_1 = \chi_0^\dagger |GS\rangle_0 \tag{2.26}$$

The previous calculation concerned only $|GS\rangle_0$. Now we perform the calculation for $|GS\rangle_1$. The calculation is similar to the previous case with only difference coming from the zero mode. Namely, take the compensation of the contribution when the zero-mode is not occupied. It gives the correlation function evaluated with $|GS\rangle_1$,

$$\langle \eta_1(x_i)\eta_2(x_j)\rangle_1 \simeq -i\delta_{i,j} + \frac{2i}{L}(-1)^{x_i - x_j} \tag{2.27}$$

One may use the following 2×2 matrix as the building block for the $2N \times 2N$ matrix:

$$\langle \eta_\alpha(x_i)\eta_\beta(x_j)\rangle_1 = \begin{pmatrix} \delta_{i,j} & -i\delta_{i,j} + \frac{2i}{L}(-1)^{x_i - x_j} \\ i\delta_{i,j} - \frac{2i}{L}(-1)^{x_i - x_j} & \delta_{i,j} \end{pmatrix} \tag{2.28}$$

In the asymptotic limit $|x_i - x_j| \gg 1$, one obtains Eq. 2.15 of the main text.

2.4.2 The entanglement entropy

We obtain the entanglement entropy for the free fermion system under consideration by directly diagonalizing the non-diagonal part of the correlation matrix. To this end, we consider the correlation matrix of the form

$$C_{i,j}^{\alpha,\beta} \equiv \begin{pmatrix} 0 & \delta_{ij} - \frac{2}{L}(-1)^{x_i - x_j} \\ -\delta_{ij} + \frac{2}{L}(-1)^{x_i - x_j} & 0 \end{pmatrix} \tag{2.29}$$

The matrix is antisymmetric. Now let us reconstruct a single-particle Majorana fermion Hamiltonian that gives the correlation matrix Eq. (2.29):

$$H_C = \frac{i}{4}\sum_{i,j}\left(\delta_{ij} - \frac{2}{L}(-1)^{x_i - x_j}\right)\gamma_{1,i}\gamma_{2,j} + h.c. \tag{2.30}$$

Here $\gamma_{\alpha,i}$ is an artificial Majorana fermion operator, and the index $\alpha = 1, 2$. One can prove that the eigenvalues of the C-matrix in Eq. (2.29) are the same as the ones for the H_C operator. Then let us diagonalize the Hamiltonian by introducing the fermion operators, $a_i = (\gamma_{1,i} + i\gamma_{2,i})/2$. Such a substitution leads to the following quadratic fermionic Hamiltonian:

$$H_C = \sum_{j=1}^{l} a_j^\dagger a_j - \frac{2}{L}\sum_{i=1,j=1}^{l}(-1)^{x_i - x_j} a_i^\dagger a_j \tag{2.31}$$

where l is the size of subsystem we take. Here, let us focus on the second term and define

$$\hat{y} = \frac{1}{\sqrt{l}}\sum_{i=1}^{l} a_i e^{i\pi x_i} \tag{2.32}$$

It is straightforward to check that $\hat{y}$ is still a fermionic operator, $\{\hat{y}, \hat{y}^\dagger\} = 1$. Thus H_C becomes

$$H_C = \sum_{j=1}^{l}\left(a_j^\dagger a_j - \frac{1}{2}\right) - \frac{2l}{L}\left(\hat{y}^\dagger\hat{y} - \frac{1}{2}\right). \tag{2.33}$$

This yielded the diagonal form of the fermionic Hamiltonian, H_C. The positive energies of the single particle spectrum thus read

$$\left|1 - \frac{2l}{L}\right|, 1, 1 \ldots, 1. \tag{2.34}$$

Note that $1 - \frac{2l}{L} \geq 0 \iff 2l \leq L$. If $2l > L$, the positive eigenvalue becomes $\frac{2l}{L} - 1$. Thus one can cast the non-trivial eigenvalues of H_C in the form

$$1 - \frac{2l}{L}, \quad \text{if } 2l < L, \quad \frac{2l}{L} - 1, \quad \text{if } 2l > L. \tag{2.35}$$

This indicates that only zero modes introduce nontrivial correlation while all other modes give trivial correlation. If ϵ denotes the entanglement spectrum, we can find it from the solution of the following relation:

$$\tanh \frac{\epsilon}{2} = 1 - \frac{2l}{L}. \tag{2.36}$$

Thus the eigenvalues of the correlation matrix in a subsystem l are the same with the number of 1's in the spectrum being $l - 1$. Then we could find the entanglement spectrum from the set of values

$$\epsilon = \log\left(\frac{L}{l} - 1\right), \quad \text{if } l \leq L/2; \quad \epsilon = \log\left(\frac{L}{L-l} - 1\right), \quad \text{if } l \geq L/2. \tag{2.37}$$

The entanglement entropy can be expressed as the sum over the entanglement spectrum[88, 89],

$$S = \sum_n \log\left(2\cosh\frac{\epsilon_n}{2}\right) - \frac{\epsilon_n}{2}\tanh\frac{\epsilon_n}{2}. \tag{2.38}$$

Here $\{\epsilon_n\}$ denotes the entanglement spectrum and the summation is performed over all values in the entanglement spectrum. Trivial terms corresponding to $\epsilon = \infty$ give zero contribution to the entropy. Thus we only need to keep track of the non-trivial contribution. Since there is a symmetry between l and $L - l$, we can only focus on

the calculation for the case $2l < L$. Before performing the calculations, we need the following identities for any real variable x:

$$2\cosh\log x = x + \frac{1}{x}, \quad \tanh\log x = \frac{x^2-1}{x^2+1}. \tag{2.39}$$

Having these, one can take $x = \sqrt{L/l-1}$ and putting together Eqs. 2.37,2.38, 2.39, one finds

$$S = \log\left(\frac{L}{L-l}\right) + \frac{l}{L}\log\left(\frac{L}{l}-1\right). \tag{2.40}$$

This is the main result in the chapter. Now we simplify Eq. 2.40 in two limiting cases:

- The limit of a small subsystem, $l \ll L$. Here first term in the expression for the entanglement entropy is approaching to zero due to the linear in l/L prefactor. Namely,

$$\log\left(\frac{L}{L-l}\right) \simeq \frac{l}{L} + O(l^2/L^2), \quad \text{if } l \ll L \tag{2.41}$$

  Similarly, we have

$$\frac{l}{L}\log\left(\frac{L}{l}-1\right) \simeq \frac{l}{L}\log\frac{L}{l} + O(l^2/L^2), \quad \text{if } l \ll L \tag{2.42}$$

  Thus in this limit, within the $O(l/L)^2$ accuracy,

$$S \simeq \frac{l}{L}\ln\left(\frac{eL}{l}\right) \tag{2.43}$$

  where e is the Euler number. The asymptotic behavior is obviously non-logarithmic in l.

- The limit of a large subsystem, $2l \simeq L$. Firstly, exactly at $L = 2l$, the entanglement entropy is found to be $S = \log 2$. It is the typical result of a gapped system. Writing $\delta l = L/2 - l$, one thus has

$$\begin{aligned} S &= \log\left(\frac{1}{1/2 + \delta l/2L}\right) + (1/2 - \delta l/L)\log\left(\frac{2}{1 - 2\delta l/L} - 1\right) \\ &\simeq \log 2 + O\left(\frac{\delta l}{L}\right)^2. \end{aligned} \tag{2.44}$$

  This indicates that the entanglement entropy, S, in this limit approaches its maximal value of $\log 2$ in this limit.

2.5 Velocity perturbation of the $z = 2$ Lifshtiz criticality

In this section, we exactly solve the noninteracting system described by the Hamiltonian Eq. 2.1 with open boundary conditions and in the presence of the velocity, v, perturbation to u. Here we derive the quantization condition corresponding to the system with open boundary conditions. This calculation supports the point made in the introduction suggesting that $\mathrm{sgn}(v)$ can distinguish topological phases and also provides an asymptotic departure from the zero-velocity momentum quantization condition.

As the first step we consider the matrix equation for the eigenstates of the system

$$\begin{pmatrix} 0 & v\partial_x + u\partial_x^2 \\ -v\partial_x + u\partial_x^2 & 0 \end{pmatrix} \psi(x) = E\psi(x). \tag{2.45}$$

For a given energy $E = \epsilon_k = \sqrt{v^2k^2 + u^2k^4} \equiv uk\kappa$,where $\kappa = \sqrt{k^2 + v^2/u^2}$, there exists four normlaized eigenvectors corresponding to that energy level. These are given by

$$
\begin{aligned}
\psi_k(x) &= \frac{1}{\sqrt{2L}} e^{ikx} \begin{pmatrix} \frac{-ivk+uk^2}{\epsilon_k} \\ -1 \end{pmatrix}, \quad \psi_{i\kappa}(x) = \sqrt{\frac{1}{1-e^{-2\kappa L}}} e^{-\kappa x} \begin{pmatrix} \sqrt{\kappa - v/u} \\ \sqrt{\kappa + v/u} \end{pmatrix} \\
\psi_{-k}(x) &= \frac{1}{\sqrt{2L}} e^{-ikx} \begin{pmatrix} \frac{ivk+uk^2}{\epsilon_k} \\ -1 \end{pmatrix}, \quad \psi_{-i\kappa}(x) = \sqrt{\frac{1}{e^{2\kappa L}-1}} e^{\kappa x} \begin{pmatrix} \sqrt{\kappa + v/u} \\ \sqrt{\kappa - v/u}. \end{pmatrix}
\end{aligned}
\tag{2.46}
$$

Under the open boundary conditions, we seek for the general solution of Eq. (2.45)in the form $\psi = C_1\psi_k + C_2\psi_{-k} + C_3\psi_{i\kappa} + C_4\psi_{-i\kappa}$, with real coeficients $C_i \in \mathbb{R}$, $i = 1 \ldots 4$. These coefficients can be determined from the condition

$$
\begin{pmatrix}
e^{-i\theta} & e^{i\theta} & \sqrt{\kappa - v/u} & \sqrt{\kappa + v/u} \\
ike^{-i\theta} & -ike^{i\theta} & -\kappa\sqrt{\kappa - v/u} & \kappa\sqrt{\kappa + v/u} \\
-e^{ikL} & -e^{-ikL} & e^{-\kappa L}\sqrt{\kappa + v/u} & e^{\kappa L}\sqrt{\kappa - v/u} \\
-ike^{ikL} & ike^{-ikL} & -\kappa e^{-\kappa L}\sqrt{\kappa + v/u} & \kappa e^{\kappa L}\sqrt{\kappa - v/u}
\end{pmatrix}
\begin{pmatrix} C_1 \\ C_2 \\ C_3 \\ C_4 \end{pmatrix} = 0, \tag{2.47}
$$

where $e^{-i\theta}$ is defined by $e^{-i\theta} = \frac{-iv/u+k}{\sqrt{v^2/u^2+k^2}}$. The existence of solution implies $\det(M) = 0$, where M is the 4×4 matrix in the left-hand-side of Eq. (2.47). This condition gives the quantization condition for the momenta in the presence of the finite velocity as

$$
\begin{aligned}
Q_\omega(y) \equiv\ & \frac{2(1+\frac{\omega^2}{y^2})}{\cosh\left(\sqrt{\omega^2+y^2}\right)} + \left[\cos y \left(2 + 2\frac{\omega^2}{y^2} + \frac{\omega^4}{y^4}\right) - \left(2\frac{\omega}{y} + \frac{\omega^3}{y^3}\right)\sin y\right] \\
& -\frac{\omega}{y}\sqrt{1+\frac{\omega^2}{y^2}}\left[\left(2+\frac{\omega^2}{y^2}\right)\cos y - \frac{\omega}{y}\sin y\right]\tanh\left(\sqrt{y^2+\omega^2}\right) = 0
\end{aligned}
\tag{2.48}
$$

where $y \equiv kL$ and $\omega \equiv Lv/u$. Analytically solving the transcendental Eq. 2.48 is a cumbersome task. The study of the properties of quantized k is beyond the scope of the present chapter, and we leave it for future works. However, one can perform an asymptotic analysis. Below we examine the asymptotic limits for both boundary and bulk modes.

- Consider the limit $|\omega| \gg 1$ and $y \ll 1$. This limit describes well the existence of boundary modes or absence thereof. In this limit, one finds that at positive $\omega > 0$, a real solution for y exists and it is found as $y \simeq 2\omega e^{-\omega}$. For negative $\omega < 0$, there is no real solution for y, indicating the absence of boundary zero-mode. Further, one can estimate the energy of boundary modes at $\omega > 0$, which is given by

$$\epsilon_b = \frac{u}{L^2}\sqrt{\omega^2 y^2 + y^4} = \frac{u(2\omega e^{-\omega})}{L^2}\sqrt{\omega^2 + (2\omega e^{-\omega})^2} \simeq \frac{2u\omega^2 e^{-\omega}}{L^2}. \tag{2.49}$$

  If we express the energy in terms of the constants u and v , we will have $\epsilon_b = 2u^{-1}v^2 e^{-Lv/u}$. The energy vanishes exponentially when $v/u \to \infty$. The exponential decay is the property corresponding to the topological degeneracy. We have also checked that the wavefunction is exponentially localized at the boundary. This concrete result supports our argument concerning the sign of $\mathrm{sgn}(v)$, discussed in the introduction.

- Consider the limit $1 < y \ll \omega$. In this limit, one finds that the quantization condition can be approximated by

$$Q_\omega(y_n + \delta y) \simeq (-1)^{n+1}\left(\frac{3\omega}{2y_n} - \frac{\omega^2}{2y_n^2}\delta y\right), \text{ where} \tag{2.50}$$
$$y_n = \frac{(2n+1)\pi}{2} \text{ is the CFT quantization condition}$$

  This indicates that the at large $\omega \gg 1$, the condition $Q_\omega(y_n + \delta y) = 0$ translates into $\delta y = 3y_n/\omega$. This, in turn, indicates that at large ω, the $Q_\omega(y)$ converges to the CFT quantization condition at a "speed" of $3/\omega$ as $\omega \to \infty$.

These calculations represent the first step for deriving the finite-size scaling function describing deviation from the gapless Lifshitz point. However, the transcendent

nature of the QC Eq. (2.48) makes it challenging to derive the form of the finite-size scaling function analytically. For this reason, we defer this analysis to forthcoming studies.

2.6 Conclusions

For the criticality Π with quadratic dispersion, $\epsilon \sim \pm k^2$, we find a universal finite-size amplitude J as the coefficient in front of L^{-2} term in the ground state energy of the system. The magnitude of J is anomalously large as it is of the order of one. There exist rich phenomena in finite-size scaling functions around this criticality[33, 83, 84]. For example, with Eq. 2.1 at $v \neq 0$, a universal finite-size scaling emerges as a function of the scale Lv, and the function has a peak at the topological side. In principle, the Lifshitz criticality can also be enriched by symmetries. In that case, the presence of boundary modes around the Fermi surface and in case of breaking of some discrete symmetries (including the chiral symmetry and the time-reversal symmetry), one expects the emergence of a non-monotonic universal function of some scaling variable. This is an interesting and open problem.

The entanglement of the ground state is also found to be non-trivial, carrying a non-logarithmic entropy. This originates from the zero modes at the Fermi surface. Compared to CFTs, zero modes play a more crucial role at the criticality Π. This offers an opportunity to observe the effects of zero modes in the fermionic field theory[90, 91, 92]. Similarly, one can also explore the behaviors of entanglement entropy and boundary entropy[53, 52, 47, 93] around Π.

Effects of interactions are not explored in the present work. The exciting question is establishing the interacting theory of the low energy sector of Π criticality. This question is beyond the scope of the Luttinger liquid[4, 5], where mostly the linear dispersion is considered.

PART II: CHIRAL SYMMETRY BREAKING IN GRAPHENE

CHAPTER 3

EMERGING PERSISTENT FRIEDEL OSCILLATIONS

The text of this chapter has been adapted from Ref. [94].

3.1 Introduction

Graphene, a single-atom-thick honeycomb sheet of carbon atoms[95, 96], possesses unusual material characteristics as compared to other 2D electron systems. Having high electron mobilities, the particles in Graphene are orders of magnitude faster than in silicon; they conduct heat much more efficiently than in diamond and conduct current order of magnitude better than in copper. Among other unique properties, Graphene is transparent and impermeable to most gases and liquids, including helium[97]. It is harder than diamond and more elastic than fiber carbon at the same time.

Unique electronic properties of Graphene[98, 99, 100, 101, 102, 103, 104, 105, 106, 107, 108, 109, 110, 111, 28, 112, 113, 114, 115, 116, 117, 118, 119, 29, 120, 121, 122, 123, 124, 125, 126, 127, 128, 129, 97] stem from the fact that it is single-atom-thick. It supports carriers with Dirac-like dispersion. When doping is low, the Fermi level is located in the close vicinity of K and K' points in the Brillouin zone. The reason for this is that Graphene quasiparticles possess chiral properties related to the two-sublattice structure of the honeycomb lattice. The latter also implies that the lattice unit cell contains two sites (atoms), leading to a "pseudospin" degree of freedom.

One of the most prominent effects in regular 2D electron systems is the interaction-induced zero-bias anomaly in the tunnel density of states (DOS). For small impurity

concentration, this anomaly can be traced to the fact[130] that impurities are dressed with Friedel oscillations of the electron density[131] which falls off as $1/r^2$ with distance, r, from the impurity. Modification of the wave functions due to scattering of electrons from the dressed impurities gives rise to the singular correction to the self-energy. Upon the advent of Graphene, the calculations similar to that in 2D gas,[102, 100, 108] indicated that the zero-bias anomaly in Graphene is absent. The underlying reason for this absence is that, with matrix underlying Hamiltonian of spin-orbit type, the backscattering of electrons is forbidden[132]. As a result, the Friedel oscillations in Graphene falls off faster than in 2D gas, as $1/r^3$.

Since [102, 108, 100] the Friedel oscillations in Graphene were studied in tiniest details, both analytically within continuum approximation and numerically, within tight-binding approximation. The results are summarized in the review[133].

Application of a magnetic field turns the spectrum of Graphene into a ladder of non-equidistant Landau levels. The corresponding perturbation of the electron density around an impurity can be cast into a sum over these levels[133, 125]. Still, at elevated temperatures, the discreteness of the Landau levels does not manifest itself, and the behavior of the Friedel oscillations with distance becomes quite a nontrivial issue. A natural expectation is that a weak, non-quantizing magnetic field, modifies the Friedel oscillations in Graphene in the same way as in the 2D electron gas[134]. By causing the curving of the semiclassical trajectories, the field gives rise to the position-dependent magnetic phase, and, thus, breaks the periodicity of the oscillations. Still, the decay law of the oscillations remains the same as in a zero field. In fact, such an intuitive reasoning, in application to Graphene, is wrong. It is not only the phase but also the *magnitude* of the Friedel oscillations that exhibits a crucial dependence on the magnetic field.

In the present chapter we consider this question systematically and find the field-dependent form of the Friedel oscillations. We shed light on the nature of the mag-

netic field modification. Our key finding is that the potential oscillates anomalously. Namely, it *does not fall off* with distance, r, in a parametrically large interval. This omnipresent effect plays a central role in a variety of quantum many-body contexts in Graphene. The polarization operator (PO) is an essential quantity for the evaluation of interaction effects using the Feynman diagrams. The non-decaying part in the PO dramatically changes the power counting in the integrand expressing Feynman diagrams. From the new power counting, the magnetic effect may give rise to a new zero-bias anomaly in DOS of Graphene, modify to the quasi-particle lifetime and thermodynamics of Dirac electrons in the Fermi liquid regime. It may also induce new temperature dependence for the dc/ac conductivities[135]. The obtained non-decaying Friedel oscillations open an avenue for controlled studies of magneto-transport. They also manifest themselves in field-related thermodynamic properties of Graphene and materials with a pseudo magnetic field such as randomly strained Graphene, stacked and twisted Dirac materials, and the properties of the wormholes in them[136, 137, 138].

The Hamiltonian that incorporates the B field in Landau gauge reads $H = H_B + \hat{u}V_{\rm imp}(r)$,

$$\hat{H}_B = v_F \left[(p_x - eBy)\hat{\Sigma}_x + p_y \hat{\Sigma}_y \right], \tag{3.1}$$

where $V_{\rm imp}(r)$ is the short-ranged impurity potential, v_F is the Fermi velocity and $\hat{\Sigma}_{x,y} = \hat{\sigma}_{x,y} \otimes \hat{\tau}_z$. One can define $\hat{\Sigma}_z = \hat{\sigma}_z \otimes \hat{\tau}_0$, together with $\hat{\Sigma}_{x,y}$, to form a su(2)-algebra. The Pauli matrices $\hat{\sigma}_{x,y,z}$ act in the space of A and B sublattices of the honeycomb lattice, $\hat{\tau}_z$ is the Pauli matrix distinguishing between two Dirac points (K and K') of the Graphene dispersion relation and $\hat{\tau}_0$ is the identity matrix. We consider the simplest case of the diagonal disorder $\hat{u} = u\hat{I}$, where u is a scalar. The uniform field breaks the chiral symmetry near each Dirac point individually since, $\mathbf{p} \cdot \hat{\mathbf{\Sigma}}$, $\hat{\Sigma} = (\hat{\Sigma}_x, \hat{\Sigma}_y)$, does not commute with the Hamiltonian. It is this non-

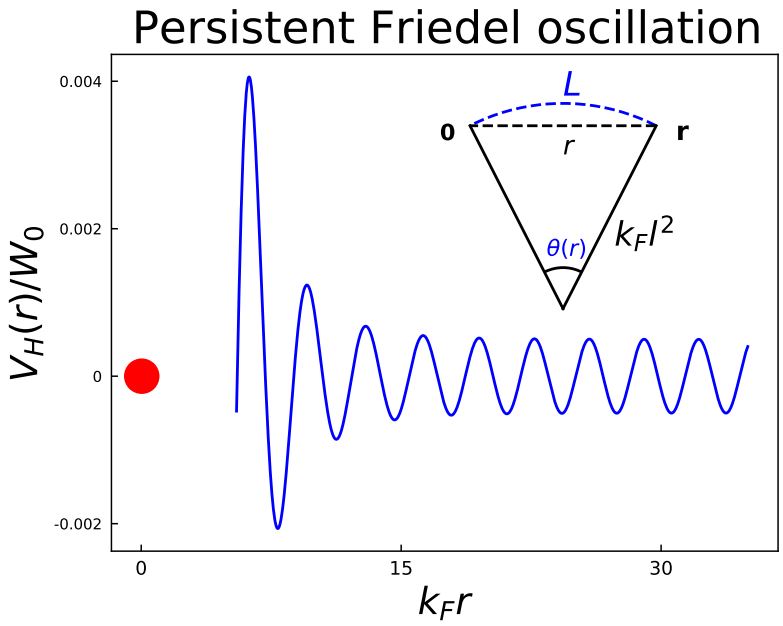

Figure 3.1: (Color online) Electrostatic potential, $V_H(r)$, is plotted vs. dimensionless distance $k_F r$ from the impurity [big (red) circle] in the presence of a weak magnetic field, B, in the range $1 \ll k_F r \ll k_F^2 l^2$. The figure is obtained from Eq. (5.6) using a typical value of $p_0/k_F = 0.1$. The potential $V_H(r)$ is measured in units of $W_0 = k_F^3 g V(2k_F)/2\pi^2 v_F$. The amplitude of oscillations first decays as $1/r^3$ and then converges to a constant $\propto B^2$. The inset illustrates the classical trajectory of 2D electrons between 0 and $\mathbf{r}$ in the presence of a weak magnetic field. L is length of the arc, r is the simply $|\mathbf{r}|$ and $\theta(r)$, the angle of the arc, is approximately given by $r/k_F l^2$.

commutativity, specific for graphene and other Dirac materials[139], that causes the observable modification of Friedel oscillations in a weak magnetic field, B. Quantitatively, the criterion of weak field is that the the magnetic length, $l = (\frac{\hbar c}{eB})^{1/2}$, is much larger than the de Broglie wavelength, k_F^{-1}. Below we show that weak field modifies the screened Coulomb potential[140, 141, 142] $V(r)$ to

$$V_H(r) = \frac{gV(2k_F)}{2\pi^2 v_F r^2}\left[\frac{1}{r}\cos\left(2k_F r - \frac{p_0^3 r^3}{12}\right) + \frac{r^2}{2k_F l^4}\sin\left(2k_F r - \frac{p_0^3 r^3}{12}\right)\right]. \qquad (3.2)$$

Here $V(2k_F)$ is the $2k_F$ component of the interaction, while the impurity potential is treated in the Born approximation with $g = u\int d^2 r V_{\rm imp}(r)$. There are two competing

terms. One can see that when the magnetic phase $p_0^3 r^3 \ll 1$ with $p_0^{-1} = (k_F l)^{4/3}/k_F$, the potential is decaying as a polynomial function, $\sim 1/r^3$. When $1 \ll p_0^3 r^3 \ll k_F r$, the potential is oscillating anomalously, with a *constant* amplitude. This persistent effect comes from the diagonal part $\hat{u} = u\hat{I}$ of impurity potential, while other non-magnetic impurity potentials do not contribute to $V_H(r)$ in the leading order in impurity scattering.

The chapter is organized as follows. In Sec.(3.2), we present a qualitative derivation of persistent Friedel oscillations, which follows from the semi-classical magnetic phase accumulated by the electron propagator. In Sec.(3.3), we present a thorough calculation of the polarization operator in the presence of a weak magnetic field and derive Friedel oscillations of electron density. The implications to interaction effects are discussed in Sec.(3.5). Concluding remarks are given in Sec.(3.6).

3.2 Qualitative discussion

In this section, we make a qualitative argument for new effects of Friedel oscillations in Eq. (3.2). Both modifications of Friedel oscillations, namely the phase $p_0^3 r^3$ in oscillations and the persistent part, can be understood semi-classically. The electron propagator, $G_{s,s'}(0, \mathbf{r})$, where $s = \pm$ represent A/B sublattices, accumulates a phase, $k_{s,s'} L$, when electrons propagate along the semi-classical arc. Here L is the length of arc shown in the inset of Fig. (3.1) and $k_{s,s'}$ is an effective momentum. The diagonal component of Dirac propagator, $G_{s,s}(0, \mathbf{r})$, can be understood as a propagator of the 2D electron gas with an effective Fermi energy $E_F^s = E_F[1 - s(2k_F^2 l^2)^{-1}]$ and an effective cyclotron frequency $\omega_0 = v_F(k_F l^2)^{-1}$. This yields an effective momentum $k_{s,s} = k_F[1 - s(2k_F^2 l^2)^{-1}]$ for diagonal propagators. While if $s \neq s'$, $k_{s,s'} = k_F$. Derivation is stated below.

3.2.1 Effective momentum

In this section, we give a derivation of effective momenta $k_{s,s'}$, mentioned by the qualitative argument from maintext, in the operator formalism (summations over Landau levels). Since $\hat{G}_K$ and $\hat{G}_{K'}$, propagators at valley K and K', can be connected by $\hat{\sigma}_z \hat{G}_K \hat{\sigma}_z = \hat{G}_{K'}$, we will only focus on the calculation of one valley, K-valley.

Under a magnetic field, the free Dirac electrons are transformed into ladders of Landau levels. The positive part of landau levels are given by $\omega_n = \sqrt{2n} v_F / l$. Here v_F is the Fermi velocity and l is the magnetic length. The corresponding wave-function at K-valley is given by $\psi_{n,k_x}(\mathbf{x}) = \frac{1}{\sqrt{2}}\Big(\varphi_{n-1,k_x}(\mathbf{x}), -\varphi_{n,k_x}(\mathbf{x})\Big)$, where $\varphi_{n,k_x}(\mathbf{x})$ is the wave-function of n^{th} Landau level of 2D electrons. Considering the positive Fermi energy E_F, we only need to consider the Landau levels around E_F. Then from definition of propagators, we get the following expression

$$G_K^{s,s'}(\mathbf{x}, \mathbf{x}'; \omega) \simeq \int \frac{dk_x}{2\pi} \sum_n \psi^s_{n,k_x}(\mathbf{x}) \psi^{s',*}_{n,s,k_x}(\mathbf{x}') \times \frac{1}{\omega - \omega_n + i\delta\Theta(\omega - E_F)}. \tag{3.3}$$

Here $s, s' = \pm$ refer to A/B sublattice and $\Theta(x)$is the step function. The off-diagonal propagtors could be expressed in terms of diagonal ones via the following expression

$$G_K^{s,s'}(\mathbf{x}, \mathbf{x}', \omega) = \frac{l^2 \omega p_{s'}}{v_F r^2} \left[G_K^{11}(\mathbf{x}, \mathbf{x}', \omega) - G_K^{22}(\mathbf{x}, \mathbf{x}', \omega) \right] \tag{3.4}$$

with $\tilde{p}_\pm = \pm(y - y') - i(x - x')$. The derivation mainly involves the properties of Lagaurre polynomials. Thus we could only focus on the Landau summations for diagonal propagators. One puts the expression of $\psi_{n,k_x}(\mathbf{x})$ and finds

$$G_K^{s,s}(\mathbf{x}, \mathbf{x}'; \omega) \simeq \frac{1}{2} \int \frac{dk_x}{2\pi} \sum_n \varphi_{n-(s+1)/2,k_x}(\mathbf{x}) \varphi^*_{n-(s+1)/2,s,k_x}(\mathbf{x}') \frac{1}{\omega - \omega_n}. \tag{3.5}$$

One can transfer the index s into $(\omega - \omega_n)^{-1}$ by variable change $n \to n - (s+1)/2$. This method yields

$$G_K^{s,s}(\mathbf{x},\mathbf{x}';\omega) \simeq \frac{1}{2}\int \frac{dk_x}{2\pi}\sum_n \varphi_{n,k_x}(\mathbf{x})\varphi^*_{n,s,k_x}(\mathbf{x}')\frac{1}{\omega-\omega_{n+(s+1)/2}}. \tag{3.6}$$

We expand $\omega_{n+(s+1)/2} = \sqrt{2n+(s+1)}v_F/l$ around the Fermi energy and find

$$\omega_{n+(s+1)/2} \simeq E_F\Big(1+\frac{s}{2k_F^2l^2}\Big) + (\delta n + 1/2)\frac{E_F}{k_F^2l^2}$$

Here it introduce an effective Fermi energy $E_F(1+s(2k_F^2l^2)^{-1})$ and effective cyclotron frequency $\omega_0 = E_F/k_F^2l^2$. Subsequently, the effective Fermi energy introduces an effective momentum by $k_{s,s} = E_F^s/v_F$. One immediately see $k_{s,s} = k_F(1+s(2k_F^2l^2)^{-1})$.

One could use Eq. (3.4) to find that effective momentum in the off-diagonal Green functions is exactly the Fermi momentum. It indicates that $k_F^{s,s'} = k_F$, if $s \neq s'$. Combining two facts, one could conclude that

$$k_{s,s'} = k_F\Big(1+\frac{s+s'}{4k_F^2l^2}\Big) \tag{3.7}$$

3.2.2 Implications of the effective momentum

The phase $p_0^3r^3$ in the oscillations is due to the curving of the path. Semi-classically, the propagator acquires a magnetic phase $k_F(L-r)$ because of the curving of trajectory. Since $L = k_Fl^2\theta$, $r = 2k_Fl^2\sin(\theta/2)$ and $\theta(r) \simeq r/k_Fl^2$, the magnetic phase $k_F(L-r)$ becomes equal to $p_0^3r^3/24$. The PO involves a product of two propagators, and thus the magnetic phase in PO is doubled. This is exactly the magnetic phase of Friedel oscillations.

The persistent part of Friedel oscillations originates from the deviation of $k_{s,s'}$ from k_F. The effective momentum implies spin-dependent magnetic phases, $\sim (k_{s,s}-k_F)r = -sr(2k_Fl^2)^{-1}$ of diagonal propagators . Although the phase is spin-dependent, it does not depend on the valleys. The phase could then be expressed compactly, $-\theta(r)\hat{\Sigma}_z/2$. The PO involves a trace of two propagators. Using the fact that Pauli

matrices are traceless and $\mathbf{tr}\hat{\Sigma}_z^2 \neq 0$, the leading magnetic contribution to PO is from a square of $\theta(r)$, namely $\theta(r)^2 \propto r^2/k_F^2 l^4$. This is the new amplitude of the second term in Eq. (3.2).

Importantly, the anomalous effect in Eq. (3.2) persists even at high temperatures, $T \sim T_0 \equiv v_F p_0$, which is much higher than the cyclotron energy. The temperature scale, T_0 can be derived qualitatively. Quasi-classically, the electron propagator accumulates a dynamical phase $k_F L$ along the arc (see the inset in Fig. 3.2). The condition $k_F(L-r) \sim 1$ can be cast in the form $r \sim p_0^{-1}$, since $k_F(L-r) \propto (p_0 r)^3$. Then, the spatial scale p_0^{-1} translates into the energy scale $v_F p_0$. This, in turn, sets the temperature scale, T_0.

3.3 The polarization operator

In this section, we show the emergence of persistent Friedel oscillations by calculating the PO rigorously in the momentum space. We start from the summation over Landau levels for PO and then develop a low energy effective theory around the Fermi level. We show how the spin-dependent magnetic phase of the gauge-invariant electron propagator manifests itself in the matrix elements of PO. Using the obtained form of the PO, we derive the Friedel oscillations and observe their persistent behavior. Finally, we discuss the smearing of anomalies in the PO under a weak magnetic field.

3.3.1 Summation over Landau levels

We start from a general expression for the PO in the momentum space

$$\Pi(k,\omega) = \sum_{n,n'=0}^{\infty} \sum_{s,s'=\pm} \frac{n_F(s'\omega_{n'}) - n_F(s\omega_n)}{\omega - (s\omega_n - s'\omega_{n'})} \left| M_{s,s',k}^{n,n'} \right|^2, \tag{3.8}$$

where $n_F(\omega)$ is the Fermi-Dirac distribution, while the frequencies, ω_n, are given by $\omega_n = (2n)^{1/2} v_F/l$. The quantities $M_{s,s',k}^{n,n'}$ are the matrix elements of $\exp(i\mathbf{kr})$ between

the states $\langle s,n|$ and $|s',n'\rangle$. Since the wave functions are the vectors consisting of the oscillator states n and $n+1$, the square of the matrix element can be expressed via the generalized Laguerre polynomials, L_m^n, as follows

$$\begin{aligned}\left|M_{s,s',k}^{n,n'}\right|^2 &= (-1)^{n'-n}\frac{e^{-x}}{\pi l^2}\Big[L_{n'-1}^{n-n'}(x)L_{n-1}^{n'-n}(x) \\ &+ L_{n'}^{n-n'}(x)L_n^{n'-n}(x) + 2ss'\left(\frac{n}{n'}\right)^{1/2}L_{n'-1}^{n-n'}(x)L_n^{n'-n}(x)\Big]. \qquad (3.9)\end{aligned}$$

where $x = k^2l^2/2$. The summation in Eq. (3.8) is performed over two valleys and two spins. However, the main contribution comes from the states near the Fermi level, E_F, which we assume to be positive. This allows to set $s = s' = 1$ in Eq. (3.9). The condition that the magnetic field is weak can be cast in the form, $N_F \gg 1$, where $N_F = k_F^2l^2/2$ is the number of Landau levels with energies between $\epsilon = 0$ and $\epsilon = E_F$.

To perform the summation over n and n' it is convenient to use the following integral representation of the Laguerre polynomials

$$L_m^n(x) = \frac{1}{2\pi}\int_0^{2\pi}\frac{d\theta}{(1-e^{i\theta})^{n+1}}\exp\left\{\frac{xe^{i\theta}}{e^{i\theta}-1} - im\theta\right\}. \qquad (3.10)$$

In the vicinity of the Kohn anomaly, $k \approx 2k_F$, we have $x \gg 1$. Under this condition, the major contribution to the integral Eq. (3.10) comes from the vicinity of $\theta = \pi$. In the vicinity of the Kohn anomaly, $k \approx 2k_F$, we have $x \gg 1$. Under this condition, the major contribution to the integral Eq. (3.10) comes from the vicinity of $\theta = \pi$. Substituting $\theta = \pi + \psi$ into the integrand and expanding with respect to ψ, we get

$$L_m^n(x) \approx \int\frac{d\psi}{2\pi}\frac{1}{2^{n+1}}\exp\left[\frac{x}{2} + i\pi m + i\phi_m^n(\psi)\right], \qquad (3.11)$$

where the phase $\phi_m^n(\psi)$ is given by $\phi_m^n(\psi) = \left(\frac{x}{4} - m - \frac{n+1}{2}\right)\psi + \frac{x\psi^3}{48}$. The last term in the brackets originates from the denominator in Eq. (3.10) expanded and exponentiated. This term is important since $n \approx N_F$ and, thus, $n \gg 1$.

From Eq. (3.11), and the form of $\phi_m^n(\psi)$, we conclude that the integrand in the product $L_{n'-1}^{n-n'}(x)L_{n-1}^{n'-n}(x)$ contains the phase

$$\phi_{n'-1}^{n-n'}(\psi)+\phi_{n-1}^{n'-n}(\psi')=\Big(\frac{x}{4}-\frac{n+n'-1}{2}\Big)(\psi+\psi')+\frac{x}{48}\left(\psi^3+\psi'^3\right), \qquad (3.12)$$

while the integrand in the product $L_{n'-1}^{n-n'}(x)L_{n}^{n'-n}(x)$ contains the phase

$$\phi_{n'-1}^{n-n'}(\psi)+\phi_{n}^{n'-n}(\psi')=\Big(\frac{x}{4}-\frac{n+n'}{2}\Big)(\psi+\psi')+\frac{1}{2}\left(\psi-\psi'\right)+\frac{x}{48}\left(\psi^3+\psi'^3\right).$$

Substituting $\theta=\pi+\psi$ into the integrand and expanding with respect to ψ yields the following integral representation for the square of the matrix element

$$\begin{aligned}\left|M_{s,s,k}^{n,n'}\right|^2 &= \frac{1}{4\pi^3 l^2}\int\frac{d\psi d\psi'}{4}\exp\left\{\frac{ix}{48}\left(\psi^3+\psi'^3\right)\right\}\left[\sum_{\nu=\pm}\exp\left\{i\left(\frac{x}{4}-\frac{n+n'+\nu}{2}\right)(\psi+\psi')\right\}\right.\\ &- \left.2\exp\left\{i\left(\frac{x}{4}-\frac{n+n'}{2}\right)(\psi+\psi')+i\frac{\psi-\psi'}{2}\right\}\right]. \qquad (3.13)\end{aligned}$$

Here the spin-dependent magnetic phase, the signal of chiral symmetry breaking, manifests itself in the matrix element as a small, but non-negligible, phases $\nu(\psi+\psi')$, with $\nu=\pm$. The negative sign in the second line is the result of the Berry phase π, which is specific for Dirac electrons. The two features are responsible for the main result of the section.

Since the main contribution to the sum in Eq. (3.8) comes from n and n' close to N_F, it is convenient to introduce the new variables $m=N_F-n$, $m'=-N_F+n'$. Then the summation in Eq. (3.8) can be performed with the help of the following identity

$$\begin{aligned}&\sum_{m,m'=-\infty}^{+\infty}\frac{n_F(\epsilon_F+\frac{\sqrt{2}v_F}{2l}m')-n_F(\epsilon_F-\frac{\sqrt{2}v_F}{2l}m)}{m'+m}\\ &\times\cos\left[(m'-m)\alpha+\beta\right]=-\frac{\pi^2T\cos\beta}{\omega_0\sinh(2\pi|\alpha|T/\omega_0)}, \qquad (3.14)\end{aligned}$$

where $\omega_0 = v_F(k_F l^2)^{-1}$ is the effective cyclotron frequency and α, β are real numbers. When applying the above identity to the summation in Eq. (3.8), we set $\alpha = y$ with $y \equiv 2^{-1}(\psi + \psi')$ and $\beta = 0$. As we will see in the next section, the integration over y defines a characteristic scale, $y \sim (k_F l)^{-2/3}$. This scale for y implies that the temperature damping term $A(T) \equiv T\left[\omega_0 \sinh(2\pi y T/\omega_0)\right]^{-1}$ is essentially temperature independent at $T \ll T_0$, namely $A(T) \approx \left[2\pi(k_F l)^{2/3}\right]^{-1}$. At $T \gg T_0$, the damping factor is important, as it becomes exponential: $A(T) \approx 2T\omega_0^{-1}\exp(-\pi T/T_0)$. In the following, we work in the low temperature limit, $T \ll T_0$. This effect of persistent oscillation will survive up to $T \sim T_0$, while at higher temperatures the Friedel oscillations will be washed out.

3.3.2 The form of Polarization operator

Since the main contribution to the sum comes from n and n' close to N_F, it is convenient to introduce the new variables $m = N_F - n$, $m' = -N_F + n'$, so that the relevant m, m' are much smaller than N_F. Note also, that the first terms in Eqs. (3.12), (3.13) measure the proximity of the momentum, k, to the Kohn anomaly $k \approx 2k_F$. Indeed, with $x = \frac{k^2 l^2}{2}$, we have $\frac{x}{4} - \frac{n+n'}{2} \approx \frac{k_F l^2}{2}\delta k - \frac{m'-m}{2}$, where $\delta k = k - 2k_F$. On other hand, the cubic terms in Eqs. (3.12), (3.13) are the smooth functions of k, so it is sufficient to replace x by $\frac{k_F^2 l^2}{2}$ in these terms. Using these notations in Eqs. (3.13), we rewrite the static polarization operator as a sum over m and m'

$$\begin{aligned}\Pi(k) \;=\; & \sum_{m,m'} \frac{n_F(\omega_{N_F+m'}) - n_F(\omega_{N_F-m})}{\omega_{N_F+m'} - \omega_{N_F-m}} \times \frac{1}{4\pi^3 l^2}\int \frac{d\psi d\psi'}{4} \exp\left[i\frac{k_F^2 l^2}{24}\left(\psi^3 + \psi'^3\right)\right] \\ & \times\left[\sum_{\nu=\pm 1} \exp\left\{i\Big(\frac{k_F l^2 \delta k}{2} - \frac{m'-m+\nu}{2}\Big)(\psi+\psi')\right\}\right. \\ & \left. -2\exp\left\{i\Big(\frac{k_F l^2\delta k}{2} - \frac{m'-m}{2}\Big)(\psi+\psi') + i\frac{\psi-\psi'}{2}\right\}\right]. \qquad (3.15)\end{aligned}$$

Subsequent steps rely on the relative smallness of m, m'. Using this smallness, we expand $\omega_{N_F-m} - \omega_{N_F+m'}$ as $\omega_{N_F-m} - \omega_{N_F+m'} \approx -\frac{\sqrt{2}v_F}{2l}(m+m')$, and replace the

difference $n_F(\omega_{N_F+m'})-n_F(\omega_{N_F-m})$ by $n_F(\omega_{N_F+m'})-n_F(\omega_{N_F-m}) \approx n_F\Big(\epsilon_F+\frac{\sqrt{2}v_F}{2l}m'\Big)-n_F\left(\epsilon_F-\frac{\sqrt{2}v_F}{2l}m\right)$. Finally, we extend the summation over m and m' to $\pm\infty$.

The above simplifications allow to perform the summation over m and m' explicitly. This is achieved with the help of the identity in Eq.(3.14). Upon applying this identity, the polarization operator Eq. (3.15) acquires the form

$$\begin{aligned}\Pi(k) &= -\frac{k_F}{2\pi^2 v_F^2}\int \frac{d\psi d\psi'}{4|\psi+\psi'|}\exp\left[i\frac{k_F^2 l^2}{24}(\psi^3+\psi'^3)\right] \\ &\quad\times\left[\sum_{\nu=\pm1}\exp\left\{i\Big(\frac{k_F l^2\delta k}{2}-\frac{\nu}{2}\Big)(\psi+\psi')\right\}\right. \\ &- \left. 2\exp\left\{i\frac{k_F l^2\delta k}{2}(\psi+\psi')+i\frac{\psi-\psi'}{2}\right\}\right]. \qquad (3.16)\end{aligned}$$

Define $2y=\psi+\psi'$, $2z=\psi-\psi'$. Then the double integral assumes the form

$$\Pi(k) = -\frac{k_F}{2\pi^2 v_F^2}\int \frac{dydz}{4|y|}\exp\left[i\frac{k_F^2 l^2}{12}\left(y^3+3yz^2\right)\right]$$
$$\left\{\sum_{\nu=\pm1}\exp\Big(ik_F l^2\delta k y-i\nu y\Big)-2\exp\Big(ik_F l^2\delta k y+iz\Big)\right\}.$$

We see that the exponents in both terms are the quadratic forms of z. Thus, with respect to z, the integrals of both terms are gaussian. The result of the integration reads

$$\Pi(k) \approx -\frac{1}{4\pi^{3/2}v_F^2 l}\int_a^\infty \frac{dy}{y^{3/2}}\left\{\sum_{\nu=\pm1}\cos\left[\left(k_F\delta k l^2-\nu\right)y\right.\right.$$
$$\left.\left.+\frac{k_F^2 l^2 y^3}{12}+\frac{\pi}{4}\right]-2\cos\left[k_F\delta k l^2 y+\frac{k_F^2 l^2 y^3}{12}-\frac{1}{k_F^2 l^2 y}+\frac{\pi}{4}\right]\right\}.$$

Equipped with Eq. (3.13) and (3.14), one can write the static PO, $\Pi(k)\equiv\Pi(k,0)$, as a single integral with respect to variable y. To clarify two different effects in $\Pi(k)$, we

present $\Pi(k)$ as sum of two terms $\Pi_1(k)+\Pi_2(k)$. Here $\Pi_1(k)$ and $\Pi_2(k)$ are expressed by

$$\begin{aligned}\Pi_1(k) &= -\frac{1}{4\pi^{3/2}v_F l}\int_a^\infty \frac{dy}{y^{3/2}} \times \left\{ \sum_{\nu=\pm 1} \cos\left[\left(k_F \delta k l^2 - \nu\right) y + \frac{k_F^2 l^2 y^3}{12} + \frac{\pi}{4}\right]\right. \\ &- \left. 2\cos\left[k_F \delta k l^2 y + \frac{k_F^2 l^2 y^3}{12} + \frac{\pi}{4}\right]\right\}, \end{aligned} \tag{3.17}$$

and

$$\Pi_2(k) = \frac{1}{2v_F l \pi^{3/2}}\int_a^\infty \frac{dy}{y^{3/2}}\left(\frac{1}{k_F^2 l^2 y}\right) \times \sin\Big(k_F \delta k l^2 y + \frac{k_F^2 l^2 y^3}{12} + \frac{\pi}{4}\Big). \tag{3.18}$$

Here $\delta k = k - 2k_F$ is the momentum measured from $2k_F$. Finite low-y cutoff, a, of the order of the lattice spacing, does not affect the form of the Friedel oscillations. We will see that Π_1 and Π_2 are responsible for the two distinct contributions to the Friedel oscillations in Eq. (3.2).

Here we derive the PO in the real space. We start with the contribution Eq. (3.17). Transformation to the real space is accomplished by the following radial integral

$$\Pi(r) = \int_0^\infty k dk (2\pi)^{-1} J_0(kr)\Pi(k) \simeq k_F \int_{-\infty}^\infty d\delta k (2\pi)^{-1} J_0(k_F r)\Pi(k_F+\delta k) \tag{3.19}$$

where $J_0(x)$ is the zeroth-order Bessel function. Here we have used the fact that $\delta k \ll k_F$. In the domain, $k_F r \gg 1$, we can replace the Bessel function by the large-x asymptote $J_0(x) \approx (2/\pi x)^{1/2}\cos\left(x - \frac{\pi}{4}\right)$. The integration over k sets $y = r(k_F l^2)^{-1}$. Then the summation over ν in Eq. (3.17) yields

$$\Pi_1(r) = -\frac{k_F}{2v_F \pi^2 r^2}\sin\Big(2k_F r - \frac{p_0^3 r^3}{12}\Big) \times \left[\cos\Big(\frac{r}{k_F l^2}\Big) - 1\right]. \tag{3.20}$$

The effect of the weak magnetic field is not negligible if the magnetic phase $p_0^3 r^3 \sim 1$. From here, the characteristic scale for y is $(p_0 k_F l^2)^{-1} = (k_F l)^{-2/3}$. Since we

consider the distances $r \ll k_F l^2$, i.e. much smaller than the Lamour radius, the magnitude of $2k_F r$ oscillations given by sin-function in the equation above can be further simplified to $k_F(2v_F\pi^2 r^2)^{-1}(1-\cos r/k_F l^2) = (4v_F\pi^2 k_F l^4)^{-1}$. The result for Π_1 describes the contribution to the oscillations of the electron density which do not decay with distance in the domain $k_F^{-1} \ll r \ll k_F l^2$. It reproduces the second term in Eq. (3.2).

Evaluation of the contribution $\Pi_2(r)$ to the PO defined by Eq. (3.18) involves the same steps as evaluation of $\Pi_1(r)$. The result reads

$$\Pi_2(r) \approx \frac{1}{2\pi^2 v_F r^3}\cos\Big(2k_F r - \frac{p_0^3 r^3}{12}\Big). \tag{3.21}$$

It reproduces the first term in Eq. (3.2). The decay $1/r^3$ is specific for Graphene, while the phase is the same as in 2D electron gas.

The the real space static PO, $\Pi(r)$, determines the Hartree potential $V_H(r)$, via modulation of the electron density $\delta n(\mathbf{r})$ around the impurity. Within the Born approximation, $\delta n(\mathbf{r}) = g\Pi(r)$. Since the density modulation originates from the backscattering of fermions, $\delta n(\mathbf{r})$ determines the Hartree potential as $V_H(r) = V(2k_F)\delta n(\mathbf{r})$. As such, the Hartree potential $V_H(r)$ is equivalent to $gV(2k_F)\Pi(r)$.

3.3.3 Smeared anomalies

The spin-dependent magnetic phase, $\theta(r)\hat{\Sigma}_z/2$, leads to a new term, $\Pi_1(k)$, in the PO, while the curving of path smears the existing anomaly in $\Pi_2(k)$. We start from the momentum-space representation of the PO given in terms of the product of the Airy functions[143]. Then we differentiate Eq. (3.18) with respect to δk twice and obtain

$$\Pi_2''(k) = -(v_F\sqrt{p_0 k_F})^{-1} F(\delta k/p_0) \tag{3.22}$$

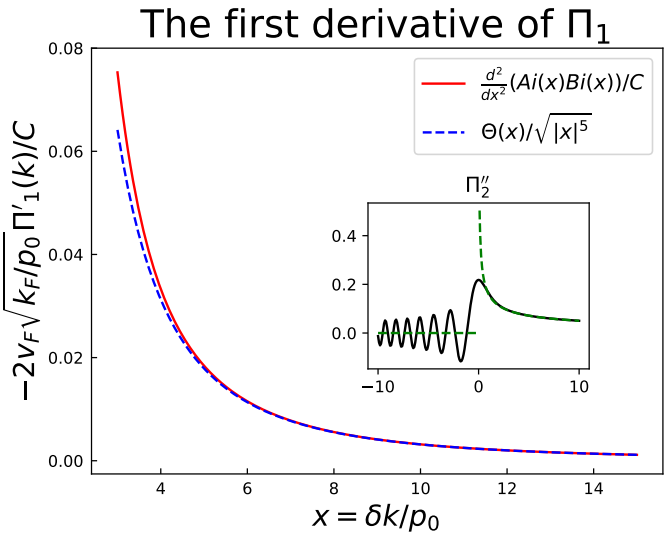

Figure 3.2: (Color online) Asymptote of derivative $\Pi_1'(k)$ is plotted versus the dimensionless $x = \delta k/p_0$. The red curve depicts $-2v_F\sqrt{k_F/p_0}\Pi_1'(k)/C = [Ai(x)Bi(x)]''/C$ versus x. Here C is a positive constant, approximately equal to 0.12. The blue curve is $1/(\sqrt{|x|})^5$, converging to Π_1' when $x \gg 1$. The inset depicts $\Pi_2''(k)$. The black curve is $-v_F\sqrt{p_0k_F}\Pi_2''(k) = Ai(x)Bi(x)$, demostrating the smearing of the anomaly. The green represents $D\Theta(x)/\sqrt{|x|}$, namely the Kohn anomaly in PO in a zero field. D is a positive constant, approximately equal to 0.16.

where $F(z) \equiv \mathrm{Ai}(z)\mathrm{Bi}(z)$. This represents the smearing of the Kohn anomaly of the PO by the weak field. Inset of Fig. (3.2) illustrates how the anomaly get smeared.

Importantly, $\Pi_1'(k)$ can also be obtained. We derive it as following. The first step is to redefine the variable $t = (k_F l)^{2/3} y$. Then the PO can be written as

$$\begin{aligned}\Pi_1(k) = \quad & \frac{(k_F l)^{1/3}}{4\pi^{3/2} v_F l} \int_{a'}^{\infty} \frac{dt}{t^{3/2}} \Bigg\{ \sum_{\nu=\pm 1} \cos\Bigg[\left(\frac{\delta k}{p_0} + \nu \sqrt{\frac{p_0}{k_F}} \right) t \\ & + \frac{t^3}{12} + \frac{\pi}{4} \Bigg] - 2\cos\left[\frac{\delta k}{p_0} t + \frac{t^3}{12} + \frac{\pi}{4} \right] \Bigg\}. \end{aligned} \tag{3.23}$$

with the new cut-off $a' = (k_F l)^{2/3} a$. The next step is to take the first derivatve of $\Pi_1(\delta k, 0)$ versus δk

$$\begin{aligned}\Pi_1'(k) = \quad & -\frac{(k_F l)^{1/3}}{4\pi^{3/2} p_0 l v_F} \int_{a'}^{\infty} \frac{dt}{\sqrt{t}} \Bigg\{ \sum_{\nu=\pm 1} \sin\Bigg[\left(\frac{\delta k}{p_0} + \nu \sqrt{\frac{p_0}{k_F}} \right) t \\ & + \frac{t^3}{12} + \frac{\pi}{4} \Bigg] - 2\sin\left[\frac{\delta k}{p_0} t + \frac{t^3}{12} + \frac{\pi}{4} \right] \Bigg\}. \end{aligned} \tag{3.24}$$

Here we use the integral expression of product of Airy functions

$$\mathrm{Ai}(z)\mathrm{Bi}(z) = \frac{1}{2\pi^{3/2}} \int_0^{\infty} dt \frac{1}{\sqrt{t}} \sin\Big(zt + \pi/4 + t^3/12 \Big).$$

Then we write $\Pi_1'(\delta k, 0)$ as summation of three Airy functions

$$\begin{aligned}\Pi_1'(k) = & -\frac{(k_F l)^{1/3}}{2 p_0 l v_F} \Big\{ \sum_{\nu=\pm} \mathrm{Ai}\Big(\frac{\delta k}{p_0} + \nu \sqrt{\frac{p_0}{k_F}} \Big) \\ & \times \mathrm{Bi}\Big(\frac{\delta k}{p_0} + \nu \sqrt{p_0/k_F} \Big) - 2\mathrm{Ai}\Big(\frac{\delta k}{p_0} \Big) \mathrm{Bi}\Big(\frac{\delta k}{p_0} \Big) \Big\}. \end{aligned} \tag{3.25}$$

Since $\sqrt{p_0/k_F} \ll 1$ (weak magnetic field), one can take Taylor Expansion of the product of Airy functions $\mathrm{Ai}(x + \nu\sqrt{p_0/k_F})\mathrm{Bi}(x + \nu\sqrt{p_0/k_F})$ around $x = \delta k/p_0$. Define

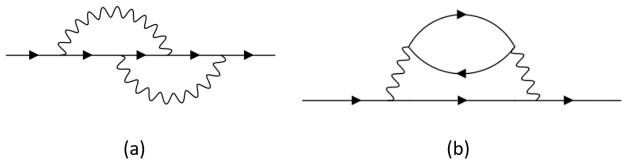

Figure 3.3: The leading contributions to the lifetime of quasi-particles. Solid lines represent the Feynman propagators. The wavy lines represent the electron-electron interactions. (a) Fock Digram. (b) Hatree diagram.

$F(x) \equiv \mathrm{Ai}(x)\mathrm{Bi}(x)$. Up to the second order perturbation, Eq. (3.25) is rewritten as

$$\Pi_1'(k) \approx -\frac{(k_F l)^{1/3}}{2p_0 v_F} \times \left\{ \sum_{\nu=\pm} \left[F(x) + \nu\sqrt{p_0/k_F} F'(x) + \frac{p_0/k_F}{2} F''(x) \right] - 2F(x) \right\} \Big|_{x=\delta k/p_0} \quad (3.26)$$

Here, the leading term cancels since $2\mathrm{Ai}(\delta k/p_0)\mathrm{Bi}(\delta k/p_0) - 2\mathrm{Ai}(\delta k/p_0)\mathrm{Bi}(\delta k/p_0) = 0$, while the first order perturbation $\propto \sqrt{p_0/k_F}$ also vanishes. So the left term is the second order perturbation in the Taylor Expansion

$$\Pi_1'(k) = -\frac{(k_F l)^{-2/3}}{2v_F} \left(\mathrm{Ai}(\delta k/p_0)\mathrm{Bi}(\delta k/p_0)\right)'' \quad (3.27)$$

Upon using $\sqrt{p_0/k_F} = (k_F l)^{-2/3}$, we reach

$$\Pi_1'(k) = -\frac{\sqrt{p_0/k_F}}{2v_F} \left(\mathrm{Ai}(\delta k/p_0)\mathrm{Bi}(\delta k/p_0)\right)'' \quad (3.28)$$

This term only emerges in the presence of the magnetic field. In the limit $\delta k \gg p_0$, $\Pi_1'(k)$, it converges to zero as $\propto B^2(\delta k)^{-5/2}$. This asymptote, plotted in Fig. (3.2), has same origin with persistent oscillations. To better understand the effect, one can Fourier transform $\Pi_1(k)$ using the asymptote. From power counting, it is straightforward to see the emergence of the non-decaying oscillating function, $\sim B^2 \sin(2k_F r)$.

3.3.4 Real-space calculation of the Friedel oscillations

Consider the modification of the Friedel oscillations in graphene by a weak uniform magnetic field. The Hamiltonian that incorporates the B field in Landau gauge reads

$$H_B = v_F \left[(p_x - eBy)\hat{\Sigma}_x + p_y \hat{\Sigma}_y \right] + \hat{u} V_{\text{imp}}(r) \tag{3.29}$$

with $\hat{u} = u\hat{I}$. Here $V_{\text{imp}}(r)$ is the short-ranged impurity potential, v_F is the Fermi velocity and $\hat{\Sigma}_{x,y} = \hat{\sigma}_{x,y} \otimes \hat{\tau}_z$. One can define $\hat{\Sigma}_z = \hat{\sigma}_z \otimes \hat{\tau}_0$, together with $\hat{\Sigma}_{x,y}$ to form a su(2)-algebra. Clearly, the uniform field breaks the chiral symmetry since, in a finite fields, $\mathbf{p} \cdot \mathbf{\Sigma}$ does not commute with H_B. In the following, we report the result for the Green function in the asymptotic region $k_F^2 l^2 \gg k_F r \gg 1$, $G(\mathbf{x}, \mathbf{x}'|\omega) = I(\mathbf{x}, \mathbf{x}'; \omega)\hat{M}(\mathbf{r}; \omega)$. Here M is given by

$$\hat{M}(\mathbf{r}; \omega) \simeq \Big(\text{sgn}(\omega) + \frac{i}{2k_F r} \Big) \hat{r} \cdot \mathbf{\Sigma} + \exp\Big\{ -i \frac{\theta(r)}{2} \text{sgn}(\omega) \hat{\Sigma}_z \Big\} \tag{3.30}$$

where we only preserve the leading orders with the non-quantized condition $k_F r \ll k_F^2 l^2$. Here $l = \sqrt{\hbar/eB}$ is the magnetic length, k_F is the Fermi momentum and ω is the frequency measured from the Fermi energy. We also define functions $I(\mathbf{x}, \mathbf{x}'; \omega)$ by

$$I(\mathbf{x}, \mathbf{x}'; \omega) = \frac{k_F}{2v_F} \frac{1}{\sqrt{2\pi k_F r}} e^{-i\chi} \exp\left\{ i\text{sgn}(\omega) \left(k_F r [1 + \frac{\omega}{\epsilon_F}] - \frac{p_0^3 r^3}{24} + i\pi/4 \right) \right\}.$$

where $r = |\mathbf{x} - \mathbf{x}'|$, $\chi = (x - x')(y + y')/(2l^2)$ describe breaking of the translational invariance and $p_0^3 = 1/(k_F l^4)$ is a scale introduced by Sedrakyan, Mishchenko, and Raikh in Ref. [134] to characterize the magnetic phase in the Green function of the 2D electron gas.

Having the form of Green's function in the presence of a weak field, one can calculate the polarization operator.

$$\Pi(\mathbf{x},\mathbf{x}';\omega) = -i\int_{\Omega}\frac{d\omega'}{2\pi}I(\mathbf{x}-\mathbf{x}';\omega')I(\mathbf{x}-\mathbf{x}';\omega'-\omega)\mathbf{tr}\hat{M}(\mathbf{r};\omega)\hat{M}(-\mathbf{r};\omega'-\omega) \quad (3.31)$$

Here we still consider an impurity with $\hat{u} = u\mathbf{I}_4$. After putting expression expressions into the equation above, one can obtain the $2k_F$ component of the polarization operator

$$\Pi_{2k_F}(\mathbf{x},\mathbf{x}';0) \approx \frac{u}{v_F}\frac{\cos(2k_Fr-\frac{p_0^3r^3}{12})}{4\pi^2r^3}+\frac{u}{v_F}\frac{\sin(2k_Fr-\frac{p_0^3r^3}{12})}{4\pi^2}\frac{1}{2k_Fl^4} \quad (3.32)$$

It fits well with the result obtained in the momentum space. The decay of the first oscillatory term here is consistent with the result of free Dirac electrons[100, 102, 108], however there is an additional magnetic phase $p_0^3r^3/12$ that breaks periodicity of oscillations. The ratio between magnitudes of the first and the second oscillatory functions is proportional to $k_F^3r^3/k_F^4l^4$. When (i) $1 \ll k_Fr \ll (k_Fl)^{4/3}$, the polarization operator in real space decays as $1/r^3$; (ii) $(k_Fl)^{4/3} \ll k_Fr \ll (k_Fl)^2$, the chiral symmetry breaking effect dominates. This symmetry-breaking term is proportional to $B^2\sin(2k_Fr)$, i.e., it oscillates with constant amplitude.

Finally, one can evaluate the effective electrostatic potential around the impurity (where we restore spin 1/2 back), which yields

$$V_H(r) = \frac{gV(2k_F)}{2\pi^2v_F}\frac{\cos(2k_Fr-\frac{p_0^3r^3}{12})}{r^3}+\frac{gV(2k_F)}{2\pi^2v_F}\frac{1}{2}p_0^3\sin(2k_Fr-\frac{p_0^3r^3}{12}) \quad (3.33)$$

3.4 Disorder in graphene

This section provides further detailed calculations for the effects of disorder potentials on the Hartree potential. Consider a non-magnetic impurity, which should

be Hermitian and time-reversal symmetric . Then the $\hat{u}$ could be expressed by ten parameters[144, 103]

$$\hat{u} = u\hat{I} + \sum_{s,l=x,y,z} u_{sl}\Sigma_s\Lambda_l \tag{3.34}$$

where the matrices are given by

$$\Sigma_x = \hat{\tau}_z \otimes \hat{\sigma}_x, \quad \Sigma_y = \hat{\tau}_z \otimes \hat{\sigma}_y, \quad \Sigma_z = \hat{\tau}_0 \otimes \hat{\sigma}_z \tag{3.35}$$

$$\Lambda_x = \hat{\tau}_x \otimes \hat{\sigma}_z, \quad \Lambda_y = \hat{\tau}_y \otimes \hat{\sigma}_z, \quad \Lambda_z = \hat{\tau}_z \otimes \hat{\sigma}_0. \tag{3.36}$$

Here the Pauli matrices $\hat{\tau}$ are acting on space of the valley indices while the Pauli matrices $\hat{\sigma}$ act in the space of A/B sublattices. Components of impurity potentials are explained as follows:

- $u\hat{I}$ is the diagonal disorder, the electric-static potential averaged over A/B sublattices.
- u_{xz} and u_{yz} introduce the hoppings between A and B.
- u_{sx},u_{sy} introduce the intervalley scatterings, $s = x, y, z$.
- u_{zz} defines the difference between on-site chemical potentials on A and B sublattices. It represents the sublattice symmetry breaking mass term.

The polarization operator is given by

$$\Pi(\mathbf{r}, \mathbf{r}'; \omega) = -i\mathrm{tr}\Big(\hat{u}\int_{-\infty}^{+\infty} \frac{dw'}{2\pi} G(\mathbf{r}, \mathbf{r}'; \omega')G(\mathbf{r}', \mathbf{r}; \omega' - \omega)\Big).$$

Then we define a intermediate matrix, which does not depend on the nature of impurity potentials

$$T(\mathbf{r}, \mathbf{r}'; \omega) = -i\int_{-\infty}^{+\infty} \frac{d\omega'}{2\pi} G(\mathbf{r}, \mathbf{r}'; \omega')G(\mathbf{r}', \mathbf{r}; \omega' - \omega)$$

After the integration, we find that T reads as

$$T(\mathbf{r},\mathbf{r}';\omega) = \frac{k_F}{v_F}\frac{1}{16\pi^2 r^2}e^{i|\omega|/v_F r}\times\begin{pmatrix} Q & 0 \\ 0 & \sigma_z Q \sigma_z \end{pmatrix} \tag{3.37}$$

where σ_y is the second pauli matrix and Q is defined by

$$Q = \cos X\begin{pmatrix} \frac{1}{k_F r}+\frac{k_F r}{k_F^2 l^2} & \frac{k_F p_-}{k_F^2 l^2} \\ -\frac{k_F p_+}{k_F^2 l^2} & \frac{1}{k_F r}-\frac{k_F r}{k_F^2 l^2}\end{pmatrix} + \sin X\begin{pmatrix} \frac{k_F^2 r^2}{2k_F^4 l^4} & \frac{k_F p_-}{k_F^2 l^2}\frac{1}{k_F r} \\ -\frac{k_F p_+}{k_F^2 l^2}\frac{1}{k_F r} & \frac{k_F^2 r^2}{2k_F^4 l^4}\end{pmatrix}. \tag{3.38}$$

Here $X = 2k_F r - p_0^3 r^3/12$. Then the polarization operator is given by

$$\Pi(\mathbf{r},\mathbf{r}';\omega) = \mathrm{tr}\Big(\hat{u}T(\mathbf{r},\mathbf{r}';\omega)\Big) \tag{3.39}$$

Since T is quasi-diagonal, the inter-valley scattering components of the impurity vanish after the trace. So we only need to take u, u_{xz}, u_{yz} and u_{zz} into consideration, involving the matrices

$$\Sigma_x\Lambda_z = \tau_0\otimes\sigma_x, \quad \Sigma_y\Lambda_z = \tau_0\otimes\sigma_y, \quad \Sigma_z\Lambda_z = \tau_z\otimes\sigma_z$$

Among these impurity potentials, we find that only u-component gives non-zero contribution to PO in the leading order

$$\Pi(\mathbf{r},\mathbf{r}';\omega) = \frac{k_F}{v_F}\frac{u}{4\pi^2 r^2}e^{i|\omega|/v_F r}\times\left(\frac{1}{k_F r}\cos(2k_F r-\frac{p_0^3 r^3}{12})+\frac{r^2}{2k_F^2 l^4}\sin(2k_F r-\frac{p_0^3 r^3}{12})\right)$$

As we can see, only the diagonal disorder $u\hat{I}$ gives the persistent Friedel oscillations. Other impurity potentials do not contribute to the polarization operator in the leading order in impurity scattering.

3.5 Implications to interaction effects

Graphene is a 2D Fermi-liquid when $E_F > 0$. This implies that the scattering rate of the quasi-particle around Fermi surface obeys $\Gamma(\omega) \propto \omega^2/E_F \log(E_F/\omega)$. In perturbation theory in interaction parameter, two leading Feynman diagrams contributing to the electron lifetime are shown in Fig. (3.3). We evaluate these diagrams in the presence of the weak magnetic field using the obtained form of the electron propagator. The computation leads to an unexpected result[135]: the quasiparticle lifetime acquires a singular in ω magnetic correction $\Gamma(\omega; B) - \Gamma(\omega; 0) \propto \omega_0^2/E_F \log\left(\omega/E_F\right)$. Here $\Gamma(\omega; B)$ is the scattering rate of quasi-particle with frequency ω in the presence of the magnetic field, B, $\omega_0 = v_F(k_F l^2)^{-1}$. The expression is valid when $E_F > \omega > \{\omega_0, T\}$. The magnetic correction above is more singular in frequency ω than the non-magnetic part. This singularity originates from the spin-dependent magnetic phase, $\theta(r)\hat{\Sigma}_z$, in electron propagators. Interestingly, the field-dependent interaction corrections to various observables in Graphene, including zero-bias anomaly in the density of states and ac/dc conductivities, also exhibit more singular behavior in either ω or temperature, T.

3.6 Concluding remarks

In this chapter we demonstrated that weak magnetic field manifests itself in the Friedel oscillations in two ways: it modifies (i) the phase of the oscillations and (ii) makes the magnitude of oscillations non-decaying in a parametrically large interval. The origin of the modification of the phase in oscillations, $\sim p_0^3 r^3$, can be traced to the curving of the classical trajectory of an electron in a weak magnetic field. The trajectory is curved even at r much smaller than the Larmour radius, leading to the magnetic phase[134] $\sim (p_0 r)^3$. This effect just by itself leads to remarkable high-temperature interaction effects in 2DEG[145, 146, 147].

Graphene also supports modification of the magnitude of the Friedel oscillations by a weak field. The origin of this effect is an emerging spin-dependent phase in electron propagators, $\sim \exp(-i\hat{\Sigma}_z\theta(r)/2)$. This effect manifests in persistent Friedel oscillations and leads to non-trivial magnetic corrections to many-body characteristics in Graphene. The transport and thermodynamic properties of monolayer Dirac materials, randomly strained Graphene and stacked and twisted Dirac materials will also be anomalously sensitive to this magnetic phase even at temperatures, $T \sim T_0$, which is much higher than the cyclotron energy[134].

Technically, to develop the theory of interaction effects in Dirac materials in the presence of the weak field, one can use the obtained form of the PO and/or Friedel oscillations in the Feynman diagrams (in the momentum or real space representations). However, a word of caution is in order here. Since the field dependence also enters the fermion Green's functions, in the Feynman diagrams, one should also consider modified propagators on the same footing along with Friedel oscillations.

Experimentally, Friedel oscillations can be observed with the scanning tunneling microscope (STM), which images 2D surfaces at the atomic level[148, 126, 149]. In STM, data are determined by backscattering processes along the energy contours. Experimental tests of these oscillations would include examining the temperature dependence of the Friedel oscillations through an extended range of temperatures $0 \lesssim T \lesssim T_0$, determining the persistent range of oscillations, $p_0^{-1} \lesssim r \lesssim k_F l^2$, and investigating the effect of their B-dependence.

CHAPTER 4

MANY-BODY CHARACTERISTICS OF DIRAC ELECTRONS

The text of this chapter has been adapted from Ref [150].

4.1 Introduction.

Electron spectrum in graphene possesses a chiral (pseudo-spin) structure[151, 152]. Two pseudospin projections are identified with two points, K and K', of the Brillouin zone near which the spectrum is characterized by a massless Dirac dispersion. Numerous consequences of the Dirac spectrum of graphene for the disorder and interaction effects were established, see e.g. Refs. [101, 103, 109, 28, 119, 29, 120, 121, 126, 127, 129, 153, 154, 155, 156, 157, 158, 159].

One distinctive feature of the graphene bandstructure is the absence of backscattering from the impurities. This feature is a consequence of orthogonality of the spinors corresponding to the wave vectors $\mathbf{k}$ and $-\mathbf{k}$. In turn, the absence of backscattering leads to the suppression of the oscillations of electron density (Friedel oscillations[131]) created by an impurity in graphene.[132, 102] In the ballistic regime[130, 160, 161, 162], electron scattering from individual impurities dressed by the Friedel oscillations is responsible for a zero-bias anomaly $\propto \ln \omega$ in conventional 2D electron gas. Here ω is the energy measured from the Fermi level and the condition $\omega\tau \gg 1$, where τ is the elastic scattering time, is implied. Fast decay of the Friedel oscillations suggests that zero-bias anomaly in graphene is absent.[163, 102] More detailed study[164] indicated that it is the Hartree correction which is absent in graphene, while the Fock correction, originating from the forward scattering, is still present.

In the absence of impurities, electron-electron interactions in 2D electron gas cause non-analytic corrections[6, 7, 8, 9] to the self-energy, $\Sigma(\omega)$. At low temperatures, $T \ll \omega$, the imaginary part of self-energy has the form $\tau_{ee}(\omega)^{-1} \sim (\omega^2/E_F)\ln(E_F/\omega)$, where E_F is the Fermi energy. Correspondingly, the real part of self-energy behaves as $\mathrm{Re}\Sigma(\omega) \sim \omega^2 \mathrm{sgn}(\omega)$. At finite T, interactions cause a correction to the specific heat[165, 166] $\delta C(T) \propto T^2$. Microscopically, the above corrections emerge in the random-phase approximation. Their derivation is so general that it is natural to expect that, in doped graphene, the interaction corrections have the same Fermi-liquid form[167].

In the present chapter, we identify the interaction effects specific to graphene. These effects emerge in the presence of a weak magnetic field. Their origin is the field-induced lifting of chiral symmetry in K and K' valleys of graphene while preserving the overall symmetry. To capture these effects, one should go beyond the random-phase approximation.

With regard to ballistic zero-bias anomaly, lifting of the chiral symmetry in the field, B, gives rise to the contribution $\propto B^2/\omega^2$, which can be even *stronger* than the zero-field contribution.[164] A formal difference between the calculations of the ballistic zero-bias anomaly in electron gas with parabolic spectrum and in graphene is that the Green functions, which enter into the calculation, have a matrix structure in graphene. Without this matrix structure, the B-sensitive contributions to the tunnel conductance *cancel out*.

A natural energy scale imposed by the field, B, in graphene is $\omega_0 = v_F/R_L$, where $R_L \propto B^{-1}$ is the Larmour radius. Quantization of the energy levels can be neglected for $\omega \gg \omega_0$. We show that the B-dependent correction to the thermodynamic characteristics of the clean graphene can be conveniently expressed in terms of ω_0. Namely, the corrections to the imaginary and real parts of self-energy behave as $\mathrm{Im}\left[\Sigma(\omega, B) - \Sigma(\omega, 0)\right] \sim \omega_0^2 E_F^{-1} \ln(\omega/T)$ and $\mathrm{Re}\left[\Sigma(\omega, B) - \Sigma(\omega, 0)\right] \sim \omega_0^2 E_F^{-1} \mathrm{sgn}(\omega)$,

respectively. On the basis of these results we draw the consequences for observables. Namely, we show that the B-dependent correction to the specific heat is temperature-independent in a wide temperature interval.

4.2 Electrons in a weak magnetic field.

The Hamiltonian of monolayer graphene which incorporates the B field in the Landau gauge reads

$$\hat{H}_B = v_F \left[(p_x - eBy)\hat{\Sigma}_x + p_y \hat{\Sigma}_y \right]. \tag{4.1}$$

Here v_F is the Fermi velocity. Here $\hat{r} = \mathbf{r}/r$, $\mathbf{\Sigma} = (\Sigma_x, \Sigma_y)$ and $\Sigma_x = \hat{\tau}_z \otimes \hat{\sigma}_x$, $\Sigma_y = \hat{\tau}_z \otimes \hat{\sigma}_y$. The Pauli matrices $\hat{\sigma}_i$ act in the space of A and B sublattices of the honeycomb lattice and $\hat{\tau}$ is the Pauli matrix distinguishing between two Dirac points in Graphene. Diagonalizing the Hamiltonian, one finds that the linear spectrum is transformed into a non-uniform ladders of spectrum, $\sqrt{2n}v_F/l$. Here $n \geq 0$ and $l = \sqrt{\hbar/eB}$ is the magnetic length. Under a weak field, the spectrum around the Fermi level, E_F, can be linearized as $\sqrt{2n}v_F/l \simeq E_F + (n - N_F)v_F(k_F l^2)^{-1}$, where $N_F = (k_F l)^2/2$. This yields the expression for the effective cyclotron frequency $\omega_0 = v_F(k_F l^2)^{-1}$.

The Feynman propagator of free Dirac electrons is known to possess a non-trivial matrix structure. Namely, in the absence of magnetic field, the propagator in the real space is given by [164]

$$G_\omega(\mathbf{r}) = \frac{k_F}{2v_F}\sqrt{\frac{1}{2k_F r}} e^{i\mathrm{sgn}(\omega)\Phi_0(r)} M_0, \tag{4.2}$$

where the phase $\Phi_0(r) = k_F r + \omega r/v_F + \pi/4$ and the matrix M_0 is given by $M_0 = (\mathrm{sgn}(\omega) + i(2k_F r)^{-1})\,\hat{r}\cdot\mathbf{\Sigma} + \hat{I}$. Here $\hat{r} = \mathbf{r}/r$, $\mathbf{\Sigma} = (\Sigma_x, \Sigma_y)$ and $\hat{I}$ is the identity matrix. This matrix structure reflects the chiral symmetry of electrons: fast decay

of the Friedel oscillations[102] and the absence of a zero-bias anomaly[164] are the consequences of this matrix form.

Presence of magnetic field modifies the gauge-invariant part of the electron propagator by breaking the chiral symmetry of the electrons in the vicinity of the Dirac point. Field-induced modification of the propagator amounts to the changes of $\Phi_0(r)$ and $M_0(r)$. The phase Φ_0 becomes $\Phi = \Phi_0 - r^3/(24k_F l^4)$, which is due to the curving of the semiclassical trajectory[134, 146, 168] in a weak field. In graphene, due to the matrix structure of the Hamiltonian, the identity matrix, $\hat{I}$, in M_0 transforms into a new 4-dimensional field-dependent matrix. This matrix contains $\hat{\Sigma}_z$, and thus, does not commute with M_0. This is because M_0 contains the matrices $\hat{\Sigma}_{x,y}$. Here $\hat{\Sigma}_z = \hat{\sigma}_z \otimes \hat{\tau}_0$, where τ_0 is a 2×2 unit matrix.

Specific form of the matrix, M, is the following

$$M(\mathbf{r}, \mathrm{sgn}(\omega)) \simeq M_0 - i\mathrm{sgn}(\omega)\varphi(r)\hat{\Sigma}_z - \frac{\varphi(r)^2}{2}\hat{I}, \tag{4.3}$$

where $\varphi(r) = \omega_0 r/(2v_F)$ is half of the angle corresponding to the arc of the Larmour circle with length r. Eq. (4.3) applies in the domain $k_F^{-1} < r < k_F l^2 = R_L$.

The *pseudospin* structure of the term $\sim \varphi(r)\hat{\Sigma}_z$ in the propagator, while preserving the chiral symmetry of the system[151], reflects the field-induced breaking thereof around a single Dirac cone. see Fig. 4.1 for a graphical representation of this effect.

In general, the ballistic correction to the density of states is given by two diagrams shown in Figs. 4.2a and 4.2b, which provide comparable contributions. However, as shown in [164], in graphene the Fock diagram dominates over the Hartree diagram in the absence of magnetic field. This is a consequence of the suppressed backscattering. We will thus focus on the sensitivity of the Fock diagram to a weak magnetic field.

We start with a matrix generalization of the analytical expressions for the Fock diagram, Fig. 4.2a. For this purpose, we consider a non-magnetic impurity causing a

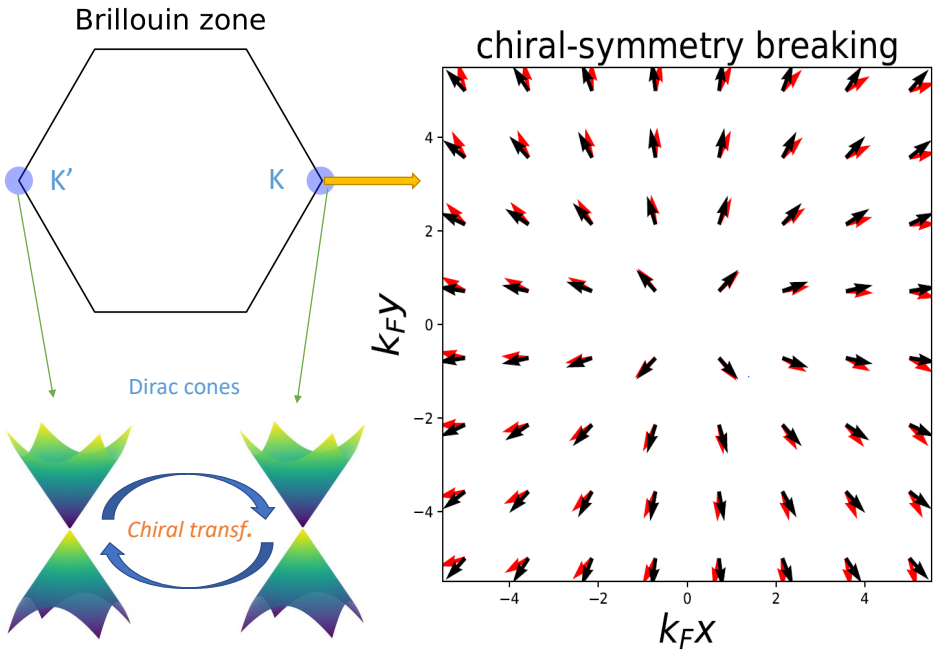

Figure 4.1: (Color online) The left panel depicts the Brillouin zone of graphene. Around the K and K' valleys, the spectrum is Dirac-like, supporting low-energy Hamiltonians $\hat{H}_K$ and $\hat{H}_{K'}$ that are connected via a chiral transformation, $H_K = \hat{\sigma}_z H_{K'} \hat{\sigma}_z$. The right panel depicts the vector field $\mathbf{v}_K(\mathbf{r})$ at K-valley. The dark (black) vectors field represents the $\mathbf{v}_K(\mathbf{r})$ at zero magnetic field. The grey (red) vector field is the $\mathbf{v}_K(\mathbf{r})$ at a weak but non-zero magnetic field. Here we take $\omega_0/(2E_F) = 0.07$. The figure shows the chiral symmetry of the state at $B = 0$. At finite B, the chiral-symmetry in one valley is broken. In the leading approximation, the angle between two vector fields is proportional to $\varphi(r)$. Importantly, the chiral transformation leads to the relation, $\mathbf{v}_{K'}(\mathbf{r}) = \mathbf{v}_K(-\mathbf{r})$, manifesting the chiral symmetry of the whole system.

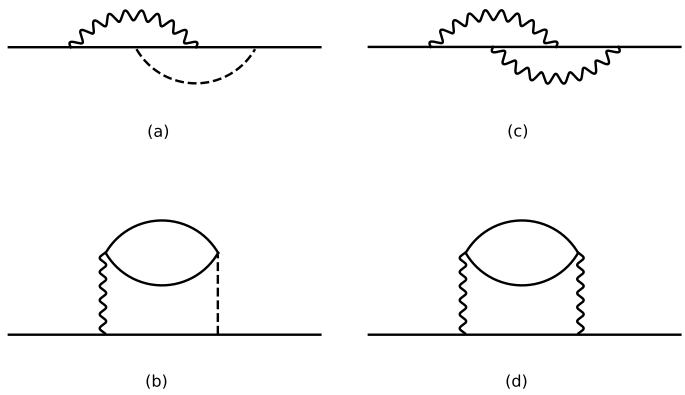

Figure 4.2: Diagrams for the corrections to the Green function. Solid lines represent the Feynman propagators. Wavy lines represent the electron-electron interactions. (a) represents the Fock diagram involving a single-impurity scattering. It yields a leading contribution to the B^2 ballistic zero-bias anomaly. (b) represents a Hartree diagram involving a single-impurity scattering. It is insensitive to a weak magnetic field. (c) and (d) represent, respectively, the Fock and Hartree diagrams for the B^2 correction to the electron lifetime. Unlike the Hartee diagram, which is the first diagram of the RPA sequence, diagram (c) yields an anomalous temperature dependence.

perturbation $\hat{u}\delta(\mathbf{r})$ and the screened interaction potential, $U(\mathbf{r})$, with a radius $\sim k_F^{-1}$. The corresponding expression reads

$$\begin{aligned}\delta G_\omega(\mathbf{r},\mathbf{r}) = \quad & \int d\mathbf{r}_1 d\mathbf{r}_2 G_\omega(\mathbf{r},\mathbf{r}_1) H_{\rm F}(\mathbf{r}_1,\mathbf{r}_2) G_\omega(\mathbf{r}_2,\mathbf{0}) \\ & \times \hat{u} G_\omega(\mathbf{0},\mathbf{r}) + (\hat{u} \leftrightarrow H_{\rm F})\,. \end{aligned} \tag{4.4}$$

Here G_ω is the free Feynman propagator of the Dirac electrons between the position of impurity $\mathbf{r}=0$ and the point $\mathbf{r}$), while H_F stands for nonlocal Fock potential

$$H_F = \frac{i}{2\pi}\int d\Omega G_{\omega+\Omega}(\mathbf{r}_1,\mathbf{0})\hat{u}G_{\omega+\Omega}(0,\mathbf{r}_2)U(\mathbf{r_1}-\mathbf{r}_2). \tag{4.5}$$

The interaction correction to the local density of states, $\delta\nu_\omega(\mathbf{r})$, is related to the retarded Green's function as $\delta\nu_\omega(\mathbf{r}) = -\frac{2}{\pi}\mathrm{Tr\ Im}\ \delta G_\omega(\mathbf{r},\mathbf{r})$.

The structure of Eqs. (4.4), (4.5) suggests that $\delta\nu_\omega(\mathbf{r})$ contains the product of 4×4 matrices. In the semiclassical limit, all trajectories $\mathbf{r}\to\mathbf{r}_1\to\mathbf{r}_2\to 0\to\mathbf{r}$ contributing to δG are close to a straight line. With screened Coulomb potential being point-like, the Fock diagram involves the following product of the M-matrices

$$F\equiv \mathrm{tr}\left[\hat{u}M(\mathbf{r},+)M(-\mathbf{r},-)\hat{u}M(\mathbf{r},-)M(-\mathbf{r},+)\right]. \tag{4.6}$$

For a qualitative discussion, let us choose $\hat{u}$ in the form of a scalar, $u_0\hat{I}$. Then the leading field-dependent term emerges as a coefficient in front of the product of the projection operators $\mathrm{tr}\left[\hat{\Sigma}_z\hat{\Sigma}_{x/y}\hat{\Sigma}_z\hat{\Sigma}_{x/y}\right]$. Since the term $\hat{\Sigma}_z$ appears in the matrix M in combination with $\varphi(r)$, we have $F\propto\varphi^2(r)$. With the help of the commutation relations for $\hat{\Sigma}_x$, $\hat{\Sigma}_y$, and $\hat{\Sigma}_z$, it is easy to check that $\mathrm{tr}\left[\hat{\Sigma}_z\hat{\Sigma}_{x/y}\hat{\Sigma}_z\hat{\Sigma}_{x/y}\right]=-\mathrm{tr}\left[I\right]$, i.e. it is nonzero. An estimate for F is $\sim u_0^2\varphi^2(r)\sim u_0^2\omega_0^2r^2/v_F^2$. With characteristic r being v_F/ω, this estimate translates into $u_0^2\omega_0^2/\omega^2$. Below we examine a number of observables having the structure similar to Eq. (4.4).

4.3 Emerging zero-bias anomaly

For the scalar impurity scattering, $\hat{u}=u_0\hat{I}$, there is no zero-bias anomaly in graphene[164]. To convert the above estimate for F into the B-dependent correction to the density of states, we perform the spatial averaging of Eq. (4.4), which generates the impurity concentration, n_i. Final result reads

$$\frac{\delta\nu_\omega(B)-\delta\nu_\omega(0)}{\nu_F}\simeq\frac{\lambda_0 n_i u_0^2}{8\pi v_F^2}\frac{\omega_0^2}{\omega^2}, \tag{4.7}$$

where $\lambda_0=k_FU_0/(2\pi v_F)$ stands for dimensionless interaction parameter, U_0 is the interaction potential with zero momentum transfer and $\nu_F=k_F/(\pi v_F)$.

The most general form of the point-like perturbation, $\hat{u}$, consistent with time-reversal symmetry is $\hat{u}=u_0\hat{I}+\sum_{s,l=x,y,z}u_{sl}\Sigma_s\Lambda_l$. Here $\Lambda_{x,y}=\hat{\tau}_{x,y}\otimes\hat{\sigma}_z$, $\Lambda_z=\hat{\tau}_z\otimes\hat{\sigma}_0$.

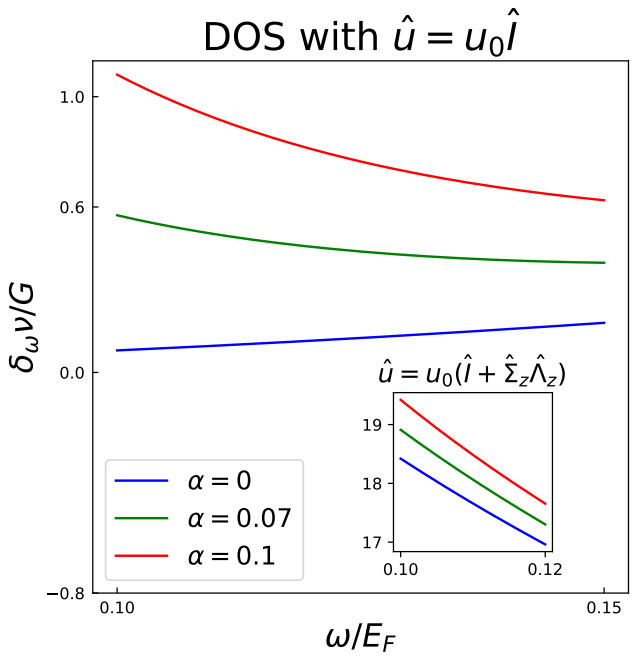

Figure 4.3: (Color online) Plot (a) and the inset illustrate the energy dependence of the interaction correction to the density of states. Three curves correspond to the three values of the dimensionless magnetic field $\alpha = (k_F l)^{-2}$. Plot (a) is for the scalar impurity with magnitude $\hat{u} = u_0\hat{I}$. The correction, $\delta\nu$, is measured in the units of $G = \nu_F n_i (u_0/2v_F)^2 \lambda_0/2\pi$. Note that for $\alpha = 0$ the zero-bias anomaly is absent, so that $\delta\nu$ is a smooth function of energy, ω, measured from the Fermi level. In the low-energy regime, $\omega/E_F < \sqrt{\alpha}$, the B-dependent anomalous term in $\delta\nu$ dominates and behaves as $\sim \alpha^2 E_F^2/\omega^2$. The inset of Plot (a) is for the impurity-induced perturbation For this perturbation, zero-bias anomaly exists even in the absence of magnetic field. The magnetic contribution yields only a small correction to the logarithmic $\delta\nu$.

The remaining nine types of the disorder can be incorporated into Eq. 4.7 by replacing u_0^2 by $t = u_0^2 - \sum_l u_{zl}^2$. The result Eq. 4.7 was obtained under the assumptions $\omega\tau \gg 1$ and $\omega \gg \omega_0$ which ensure the ballistic regime and the irrelevance of the Landau quantization, respectively.

Emergence of a zero-bias anomaly in graphene in the presence of magnetic field manifests itself in the local density of states (DOS), $\delta\nu_\omega(\mathbf{r}, B) = -2\pi^{-1}$ tr [Im $G_R(\mathbf{r}, \mathbf{r}, \omega)$]. Evaluation of Eq. (4.4) yields

$$\frac{\delta\nu_\omega(\mathbf{r}, B) - \delta\nu_\omega(\mathbf{r}, 0)}{\nu_F} \simeq \frac{\lambda_0 t\omega_0^2}{(2\pi v_F^2)^2} \cos\frac{\omega r}{v_F}. \tag{4.8}$$

Note that, unlike the $B = 0$ case[164], the interaction correction Eq. (4.8) is isotropic. The most dramatic difference between Eq. (4.8) and the $B = 0$ result is that the zero-field correction falls off as $1/r^2$, while the amplitude of oscillations in Eq. (4.8) does not depend on r. Naturally, the fall-off starts from the distances $r \gtrsim R_L = v_F/\omega_0$, where Eq. (4.8) does not apply. Technically, the extra factor r^2 comes from $\varphi^2(r)$ in the factor F. In relation to the local DOS, we would like to point out that it can be measured experimentally using the scanning tunneling microscopy (STM)[169, 170].

Below we give a detailed derivation of Eq. 4.7. now we start from the standard expression for the density of states, $\nu(\omega; B)$, in terms of the retarded Green function,

$$\nu(\omega; B) = -\frac{2}{\pi} \int d^2 r \mathbf{Im tr} G_R(\mathbf{r}, \mathbf{r}; \omega). \tag{4.9}$$

In the ballistic regime, the interaction correction to $\nu(\omega; B)$ is given by the Fock and the Hartree diagrams depicted in Figs. 4.2a and 4.2c, respectively. Specifics of graphene is the absence of the backscattering. As a result, the Hartree diagram, which is dominated by the backscattering, does not lead to the zero-bias anomaly. Analytical expression for the Fock diagram reads

$$\delta_f G(\mathbf{r},\mathbf{r};\omega) \simeq i2U \int d^2 r_1 \int_{-E_F}^{-\omega} \frac{d\Omega_1}{2\pi} G(\mathbf{r},\mathbf{r}_1;\omega) G(\mathbf{r}_1,0;\omega+\Omega_1)$$
$$\times \hat{u} G(0,\mathbf{r}_1;\omega+\Omega_1) G(\mathbf{r}_1,0;\omega) \hat{u} G(0,\mathbf{r};\omega). \quad (4.10)$$

Here we consider the touching potential. Thus the interaction potential in momentum space is uniform, namely, a single number U. We assume that ω is positive and use the Green function, G, instead of G_R.

Spatial averaging of $\delta_f G(r,r)$ is accomplished with the help of the following identity

$$\int d^2 r G(0,\mathbf{r};\omega) G(\mathbf{r},\mathbf{r}_1;\omega) = -\partial_\omega G(0,\mathbf{r}_1;\omega). \quad (4.11)$$

Another simplification comes from the fact that the distances contributing to the integral Eq. 4.10 are large, so that the Green function can be replaced by the semiclassical asymptote

$$\partial_\omega G(0,\mathbf{r}_1;\omega) \simeq i\mathrm{sgn}(\omega) \frac{r_1}{v_F} G(0,\mathbf{r}_1;\omega). \quad (4.12)$$

Subsequent steps are in line with the calculation in Phys. Rev. B **76**, 165402 (2007). They involve substituting the asymptotic expressions for the Green functions into $\delta_f \nu(\omega;B)$, calculating the product of matrices entering the Green functions and integrating out the intermediate frequency Ω_1. As a result, the expression for $\delta_f \nu(\omega;B)$ simplifies to

$$\delta_f \nu(\omega;B) \;=\; -2n_i U_0 \mathbf{Re} \int d\theta dr_1 \frac{k_F^2}{32\pi^4 v_F^4} \frac{1}{r_1} e^{2i\omega r_1/v_F} \times \mathbf{tr}(\hat{u}^2 - \hat{\Sigma}(\psi)\hat{u}\hat{\Sigma}(\bar{\psi})\hat{u}),$$

where n_i is the impurity concentration. In Eq. (4.13) the angle θ is the angular coordinate of $\mathbf{r}_1$, while the angles $\psi, \bar{\psi}$ are defined as

$$\psi = \theta + \varphi(r_1), \quad \bar{\psi} = \theta - \varphi(r_1). \quad (4.13)$$

Finally, the function $\hat{\Sigma}$ is expressed via ψ, $\bar{\psi}$ as follows

$$\hat{\Sigma}(\psi) = (\cos\psi, \sin\psi) \cdot (\hat{\Sigma}_x, \hat{\Sigma}_y). \tag{4.14}$$

Eq. (4.13) illustrates how the magnetic phase, $\varphi(r_1)$, from the electron propagator enters the interaction correction to the density of states.

To explore the magnetic field dependence, we analyze the intermediate integral

$$\int \frac{d\theta}{2\pi} \mathbf{tr}(\hat{u}^2 - \Sigma(\psi)\hat{u}\Sigma(\bar{\psi})\hat{u}) \simeq 4 \sum_{l=x,y,z} (2u_{zl}^2 + u_{yl}^2 + u_{xl}^2) + t\frac{2r_1^2}{k_F^4 l^4}. \tag{4.15}$$

Here $t = u^2 - \sum_l u_{zl}^2$. From the above expression, one concludes that only the scalar potentials, including u, u_{zz}, u_{zx} and u_{zy}, are sensitive to the magnetic field. Defining a dimensionless variable $x = 2\omega r_1/v_F$, we cast the magnetic-field correction in the form of a single integral over x

$$\frac{\delta_f\nu(\omega; B) - \delta_f\nu(\omega; 0)}{\nu_F} = -\frac{k_F U_0}{v_F} \frac{t}{16\pi^2 v_F^2 v} \frac{\omega_0^2}{\omega^2} \int_{2\omega/E_F}^{2\omega/\omega_0} x e^{-\epsilon x} \cos x dx. \tag{4.16}$$

Here ϵ is introduced as a cutoff. In the limit $\omega_0 \ll \omega \ll E_F$, we get

$$\frac{\delta_f\nu(\omega; B) - \delta_f\nu(\omega; 0)}{\nu_F} \simeq n_i \frac{k_F U_0}{v_F} \frac{t}{16\pi^2 v_F^2} \frac{\omega_0^2}{\omega^2}. \tag{4.17}$$

We thus arrive to the main conclusion of DOS.

4.4 Lifetime of quasi-particles

Energy dependence of electron-electron scattering rate, τ_{ee}^{-1}, in doped graphene is $\omega^2 \ln(E_F/\omega)$, as in a regular Fermi liquid.[167] This dependence emerges already in the lowest order of the perturbation theory. Corresponding diagram is illustrated

in Fig. 4.2. Subsequent summation of the higher-order diagrams within the random-phase approximation (RPA) modifies the prefactor in τ_{ee}^{-1}. Equally, the calculations leading to non-analytic interaction corrections[9] apply to the doped graphene. With regard to the magnetic field dependence of τ_{ee}^{-1}, it appears that, similarly to the zero-bias anomaly, the leading B-dependence originates from the Fock diagram on Fig. 4.2c, which is beyond the RPA.

The result for the correction, $\delta\tau_{ee}^{-1}(B)$, depends on the ratio ω/T. In the low-T limit, $\omega \gg T$, this correction reads

$$\delta\tau_{ee}^{-1}(B) \simeq \frac{\lambda_0\lambda_{2k_F}\omega_0^2}{2\pi E_F}\ln\Big(\frac{|\omega|}{\Delta}\Big), \quad |\omega| \gg T, \tag{4.18}$$

where $\lambda_{2k_F} = k_F U_{2k_F}/(2\pi v_F)$, $\Delta = \max\{T, \tau_{ee}^{-1}\}$. The relative magnitude of the correction is essentially $(\omega_0/\omega)^2$ and, similarly to the zero-bias anomaly, it originates from the magnetic phase $\hat{\Sigma}_z\varphi(r)$ of the propagator in Feynman diagrams.

In the high-temperature limit, $T \gg \omega$, evaluation of the B-dependent correction to the diagram Fig. 4.2c yields

$$\delta\tau_{ee}^{-1}(B) \simeq -\ln(2)\frac{\lambda_0\lambda_{2k_F}\omega_0^2}{2\pi E_F}, \quad T \gg |\omega|. \tag{4.19}$$

Note that the correction is T-independent, but it exists on the background of the T^2 main term.

4.5 Effective velocity and Specific heat

In the doped graphene, as in 2D electron gas, the effective velocity of quasi-particles, v^*, and specific heat, C_v, are expected to acquire interaction corrections[9, 167]. These corrections scale as $\delta v^* \propto T$ and $\delta C_v \propto T^2$, respectively. Both anomalies originate from the non-analytic corrections to the quasi-particle lifetime [9]. Here we trace how the ω_0^2-corrections specific for graphene manifest themselves in v^* and C_v.

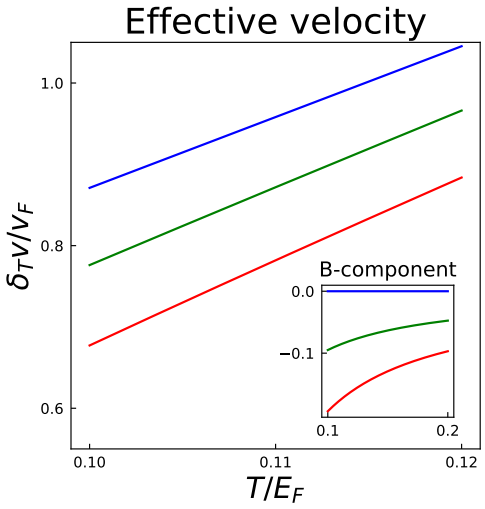

Figure 4.4: (Color online) In plot the temperature-dependent interaction correction to the effective velocity, $\delta_T v^* = v^*_T(B) - v^*_{T=0}(B)$ is shown. The inset shows the B-dependent component of the effective velocity, $\delta_T v^*(B) - \delta_T v^*(0)$. This part behaves as an inverse temperature, $\sim \alpha^2 E_F/T$.

The question of interest is the temperature dependence of these corrections. We found that the correction to v^* behaves as ω_0^2/T, while the correction to C_v is $\propto \omega_0^2/v_F^2$ and is T-independent. Both originate from ω_0^2 correction to the lifetime given by Eqs. 4.18 and 4.19.

Another ingredient required to find the B-dependent corrections to v^* and C_v is the electron spectrum renormalized by the interactions. The corresponding ω_0^2-correction comes from the Fock diagram Fig. 4.2c

$$\mathrm{Re}[\Sigma(\omega, B) - \Sigma(\omega, 0)] \simeq -\frac{\lambda_0 \lambda_{2k_F} \omega_0^2}{16 E_F} \times \begin{cases} \mathrm{sgn}(\omega), & |\omega| \gg T \\ \omega/(2T), & |\omega| \ll T. \end{cases} \tag{4.20}$$

The above correction can, in principle, be measured using the Angle-resolved photoemission spectroscopy (ARPES)[171] from the analysis of the constant energy maps[172] at different values of B.

In the limit $T \gg \omega$, the renormalized spectrum Eq. 4.20 leads to the following correction to the effective velocity of quasi-particles $v = v_F/\left(1 - \partial_\omega \mathrm{Re}\Sigma|_{\omega=0}\right)$,

$$\frac{v(B)-v(0)}{v_F} \simeq -\frac{\lambda_0 \lambda_{2k_F} \omega_0^2}{32 E_F^2} \frac{E_F}{T}. \tag{4.21}$$

Note that $v(0)$ contains a non-magnetic interaction correction which is linear in T. On the contrary, the B-dependent correction is $\propto T^{-1}$. This feature is illustrated in Fig. 4.4 for several values of B. Since the thermodynamical potential, Ω, involves the summation over energies of quasi-particles near the Fermi level, the energy correction in Eq. 4.20 has non-trivial implications for thermodynamics. Here we consider the specific heat per unit volume, $C_v = V^{-1}\partial\Omega/\partial T$, where V is the volume of system. The result for specific heat in the limit $T \gg \omega_0$ is the following,

$$\delta C_v(B) - \delta C_v(0) \simeq -\frac{\lambda_0 \lambda_{2k_F} \omega_0^2}{8\pi v_F^2}, \tag{4.22}$$

where $\delta C_v(B)$ is the interaction correction to the specific heat. Note that $\delta C_v(0)$ contains the conventional T^2 term, specific for 2D Fermi liquid. We find that the field-dependent correction to δC_v is a T-independent. In the absence of electron-phonon interactions, the field-dependent correction exists in a parametrically large interval of temperatures, $\omega_0 < T < E_F$. Eq. 4.22 can be verified experimentally by measuring the specific heat of graphene in a comprehensive Raman optothermal method[173].

4.6 Self-energy at finite temperature

In this section, we provide a detailed calculation of the self-energy at finite temperature. The calculation presented here is performed for a single spin. At finite temperature, the asymptotic expression for the propagator reads

$$G(\mathbf{z}, \mathbf{z}'; i\omega_n) \simeq e^{-i\chi} I(\mathbf{z}-\mathbf{z}'; i\omega_n) \hat{M}(\mathbf{z}-\mathbf{z}'; \mathrm{sgn}(n)), \tag{4.23}$$

where $i\omega_n$ is the fermionic Matsubara frequency.

In the coordinate space, the Hartree and Fock corrections to the self-energy are, respectively, given by the summation over bosonic Matsubara frequencies

$$\Sigma_{\text{Hartree}}(\mathbf{x}_1, \mathbf{x}_2; i\omega_n) \simeq -TU^2 \sum_{i\nu_m} G(\mathbf{x}_1, \mathbf{x}_2, i\omega_n - i\nu_m)\Pi(\mathbf{x}_2 - \mathbf{x}_1, i\nu_m), \tag{4.24}$$

and

$$\begin{aligned}\Sigma_{\text{Fock}}(\mathbf{x}_1, \mathbf{x}_2; i\omega_n) \simeq T^2U^2 \sum_{i\nu_m, i\nu_l} & G(\mathbf{x}_1, \mathbf{x}_2; i\omega_n - i\nu_m) \\ & G(\mathbf{x}_2, \mathbf{x}_1; i\omega_n - i\nu_m - i\nu_l)G(\mathbf{x}_1, \mathbf{x}_2; , i\omega_n - i\nu_l).\end{aligned} \tag{4.25}$$

Here U is the short-ranged interaction potential (touching potential) in momentum space, $\nu_m = 2\pi Tm$ and $\Pi(\mathbf{x}_2 - \mathbf{x}_1, i\nu_m)$ is the polarization operator. Since the chiral structure of graphene suppresses the backscattering process, we focus on the zero-momentum species of polarization operator Π_0,

$$\Pi_0(\mathbf{x_2}, \mathbf{x_1}; i\nu_m) \;=\; \frac{k_F^2}{2\pi^2 v_F^2}\frac{1}{k_F r}|\nu_m| e^{-|\nu_m|r/v_F}. \tag{4.26}$$

Here we introduced $r = |\mathbf{x_2} - \mathbf{x_1}|$. Further, we consider quasi-particles characterized by index ν (ν is characterized by the momentum for a free particle in the absence of the B-field and the Landau level index in the presence of the magnetic field). Then the self-energy is defined by

$$\Sigma(\nu, i\omega_n) = \mathbf{tr}\int d^2x_1 d^2x_2 A(\mathbf{x}_2, \mathbf{x}_1, \nu)\Sigma(\mathbf{x}_1, \mathbf{x}_2, i\omega_n)/\Big(Vk_F/2\pi v_F\Big), \tag{4.27}$$

where A is the spectral function of electrons in the absence of interaction and V is the volume of the system. The spectral function is defined from by $A = -(2\pi i)^{-1}(G_R - G_A)$. Here $G_{R/A}$ are the retarded/advanced non-interacting Green functions. Taking

an analytic continuation $i\omega_n \to \omega + i\delta$ (consider the case with $\omega > 0$) and separating the on-shell singularity, we obtain

$$\Sigma_{\rm Hartree}(\omega + i\delta) \simeq i\Big(\frac{k_F U}{v_F}\Big)^2 \frac{T}{2\pi^2 E_F} \int \frac{e^{-\delta r/v_F} dr}{r} \Bigg[\frac{\pi T}{\sinh^2(2\pi T r/v_F)} - \frac{e^{i2\omega r/v_F}}{\sinh(2\pi T r/v_F)} \Big(-i\omega + \frac{\pi T}{\tanh(2\pi T r/v_F)} \Big) \Bigg],$$

and

$$\Sigma_{\rm Fock}(\omega + i\delta) \simeq -i\Big(\frac{k_F U}{v_F}\Big)^2 \frac{T}{2\pi^2 E_F} \int dr \frac{e^{-\delta r/v_F} \sin^2\varphi(r)}{r} \Bigg[\frac{\pi T}{\sinh^2(2\pi T r/v_F)} - \frac{e^{i2\omega r/v_F}}{\sinh(2\pi T r/v_F)} \Big(-i\omega + \frac{\pi T}{\tanh(2\pi T r/v_F)} \Big) \Bigg]. \quad (4.28)$$

4.6.1 Low-temperature limit: $T/\omega \ll 1$

For small $T/\omega \ll 1$, the $\Sigma_{\rm Hartree}$ is simplified to

$$\Sigma_{\rm Hartree}(\omega + i\delta) \simeq i\Big(\frac{k_F U}{v_F}\Big)^2 \frac{1}{4\pi^3} \int dr \frac{e^{-\delta r/v_F} dr}{k_F r^2} \Bigg[\frac{v_F}{2r} - e^{i2\omega r/v_F} \Big(-i\omega + \frac{v_F}{2r} \Big) \Bigg], \quad (4.29)$$

and the $\Sigma_{\rm Fock}$ becomes

$$\Sigma_{\rm Fock}(\omega + i\delta) \simeq -i\Big(\frac{k_F U}{v_F}\Big)^2 \frac{1}{4\pi^3} \int dr \frac{e^{-\delta r/v_F} dr}{k_F r^2} \Bigg[\frac{v_F}{2r} - e^{i2\omega r/v_F} \Big(-i\omega + \frac{v_F}{2r} \Big) \Bigg] \sin^2\varphi(r).$$

- *Quasiparticle lifetime.* Here we calculate the imaginary part of the self-energy and find the expression for the lifetime. Defining dimensionless quantity $x = 2\omega r/v_F$, we write $\Sigma_{\rm Hartree}(\omega + i\delta)$ as

$$\mathbf{Im}\Sigma_{\rm Hartree}(\omega + i\delta) \simeq \Big(\frac{k_F U}{v_F}\Big)^2 \frac{\omega^2}{2\pi^3 E_F} \int_{2\omega/E_F}^{+\infty} dx \Big(\frac{1}{x^3}[1 - \cos x] - \frac{1}{x^2} \sin x \Big) \quad (4.30)$$

The leading term in the integral $\int_{2\omega/E_F}^{+\infty} dx \Big(\frac{1}{x^3}[1-\cos x] - \frac{1}{x^2}\sin x \Big)$ is $2^{-1}\log(2\omega/E_F)$. Thus one obtains $\mathbf{Im}\Sigma_{\rm Hartree}(\omega + i\delta) \simeq \Big(\frac{k_F U}{v_F}\Big)^2 \frac{\omega^2}{4\pi^3 E_F} \log(2\omega/E_F)$, which is

the typical behavior of the lifetime of 2D Fermi liquids. The scattering rate $\delta = -\tau_{\rm ee}^{-1}/2$ is estimated by the RPA diagrams which give the leading contribution to the lifetime of quasi-particles. Now we study the B-dependence of the lifetime. We consider the weak magnetic field such that the mean free path is smaller than the Lamour radius ($\delta > \omega_0$). Consider two cases.

The first case is $T \ll \tau_{\rm ee}^{-1}$. In this limit, the temperature is an irrelevant scale and the RPA lifetime dominates. We obtain the following equation fo the field-dependent self-energy term:

$$\mathbf{Im}\Sigma_{\rm Fock}(\omega + i\delta) \simeq -\Big(\frac{k_F U}{v_F}\Big)^2 \frac{\omega_0^2}{16\pi^3 E_F} \int_{2\omega/E_F}^{+\infty} \frac{e^{-\epsilon x} dx}{x} \Big[1 - \cos x\Big]. \qquad (4.31)$$

Here $\epsilon = \delta/2\omega$. The leading term in the integral $\int_{2\omega/E_F}^{+\infty} \frac{e^{-\epsilon x} dx}{x} \Big[1 - \cos x\Big]$ giving $\log(2\omega\tau_{\rm ee})$.

The second case is $T \gg \tau_{\rm ee}^{-1}$. In this limit, the temperature enters under the logarithm replacing the inverse lifetime there.

- *Spectrum.* The real part of the self-energy gives a correction to the spectrum of quasi-particles. Thus here we compute $\mathbf{Re}\Sigma_{\rm Hartree}$ and $\mathbf{Re}\Sigma_{\rm Fock}$

$$\mathbf{Re}\Sigma_{\rm Hartree}(\omega + i\delta) \simeq \Big(\frac{k_F U}{v_F}\Big)^2 \frac{1}{2\pi^3} \frac{\omega^2}{E_F} \int_{2\omega/E_F}^{+\infty} dx \Big[-\frac{1}{x^2} \cos x + \frac{1}{x^3} \sin x \Big]. \qquad (4.32)$$

The leading term in integral $\int_{2\omega/E_F}^{+\infty} dx \Big[-\frac{1}{x^2} \cos x + \frac{1}{x^3} \sin x \Big]$ is simply a constant, given by $\pi/4$. Thus this leads to $\mathbf{Re}\Sigma_{\rm Hartree}(\omega + i\delta) \simeq \Big(\frac{k_F U_0}{v_F}\Big)^2 \frac{1}{8\pi^2} \frac{\omega^2}{E_F}$ and

$$\mathbf{Re}\Sigma_{\rm Fock}(\omega + i\delta) \simeq \Big(\frac{k_F U}{v_F}\Big)^2 \frac{1}{32\pi^3} \frac{\omega_0^2}{E_F} \int_{2\omega/E_F}^{\omega/\omega_0} dx e^{-\epsilon x} \Big(\cos x - \frac{1}{x} \sin x \Big).$$

Then we extend the integral from 0 to ∞, since $\omega/E_F \ll 1$ and $\epsilon\omega/\omega_0 \gg 1$. This yields

$$\mathbf{Re}\Sigma_{\text{Fock}}(\omega) \simeq -\Big(\frac{k_F U}{v_F}\Big)^2 \frac{1}{(8\pi)^2}\frac{\omega_0^2}{E_F}. \tag{4.33}$$

The expression is valid when $\tau_{\text{ee}}^{-1}(\omega) > \omega_0$. This introduces the correction to the quasi-particle spectrum in the low temperature limit, shown in Eq. 11. If one considers $\omega < 0$, one will restore a $\text{sgn}(\omega)$.

4.6.2 High-temperature limit: $T/\omega \gg 1$

In case of large $T/\omega \gg 1$, the temperature is a relevant scale.

- *Lifetime.* Here we compute the imaginary part of the self-energy to find the quasiparticle lifetime. Defining dimensionless variable $x = \pi T r/v_F$, we write $\Sigma_{\text{Hartree}}(\omega)$ as

$$\mathbf{Im}\Sigma_{\text{Hartree}} \simeq -\Big(\frac{k_F U}{v_F}\Big)^2 \frac{T^2}{4\pi E_F}\int_{\pi T/E_F}^{+\infty}\frac{dx}{x}\frac{1}{\cosh^2 x}. \tag{4.34}$$

The integral $\int_{\pi T/E_F}^{+\infty}\frac{dx}{x}\frac{1}{\cosh^2 x}$ is equal to $\log(E_F/\pi T) + c + O(T/E_F)$. Here c is a constant. Thus we find $\mathbf{Im}\Sigma_{\text{Hartree}} \simeq \Big(\frac{k_F U_0}{v_F}\Big)^2 \frac{T^2}{4\pi E_F}\log(\pi T/E_F)$, a typical result for 2D Fermi-liquids. Meanwhile, one could write $\Sigma_{\text{Fock}}(\omega)$ as

$$\mathbf{Im}\Sigma_{\text{Fock}} \;\simeq\; \Big(\frac{k_F U}{v_F}\Big)^2 \frac{1}{4\pi^3}\frac{\omega_0^2}{4E_F}\int_{\pi T/E_F}^{\infty} dx \frac{x}{\cosh^2 x}.$$

The integral $\int_{\pi T/E_F}^{\infty} dx\frac{x}{\cosh^2 x} = \log(2) + O(T^2/E_F^2)$. Thus $\mathbf{Im}\Sigma_{\text{Fock}} \simeq \Big(\frac{k_F U_0}{v_F}\Big)^2 \frac{1}{4\pi^3}\frac{\omega_0^2}{4E_F}\log(2)$. This gives the correction to the lifetime.

- *Spectrum.* The real part of $\Sigma_{\rm Hartree}$ is given by

$$\mathbf{Re}\Sigma_{\rm Hartree}(\omega+i\delta) \simeq -\Big(\frac{k_F U}{v_F}\Big)^2 \frac{\omega T}{2\pi^2 E_F}\int_{2\pi T/E_F}^{\infty}\frac{dx}{x}\frac{1}{\sinh x}\Big(1-\frac{x}{\tanh x}\Big).$$

The integral $\int_{2\pi T/E_F}^{\infty}\frac{dx}{x}\Big[\frac{1}{\sinh x}\Big(1-\frac{x}{\tanh x}\Big)\Big] = -\log(2)+O(T/E_F)$. Thus we find that $\mathbf{Re}\Sigma_{\rm Hartree}(\omega+i\delta) \simeq \Big(\frac{k_F U_0}{v_F}\Big)^2\frac{\omega T}{2\pi^2 E_F}\log(2)$. This is also a typical result for 2D Fermi liquids. Then we consider the Fock diagram and write $\mathbf{Re}\Sigma_{\rm Fock}$ as

$$\mathbf{Re}\Sigma_{\rm Fock}(\omega+i\delta) \simeq \Big(\frac{k_F U}{v_F}\Big)^2 \frac{\omega\omega_0^2}{32\pi^4 E_F T}\int_{2\pi T/E_F}^{2\pi T/\omega_0} dx\, x\frac{1}{\sinh x}\Big(1-\frac{x}{\tanh x}\Big). \quad (4.35)$$

Since $T/E_F \ll 1$ and $T/\omega \gg 1$, we can replace the lower bound of the integral domain by 0 and the upper bound by ∞. Making use of the integral $\int_0^{+\infty} dx x\frac{1}{\sinh x}\Big(1-\frac{x}{\tanh x}\Big) = -\pi^2/4$, we obtain at $T \gg \omega, \omega_0$:

$$\mathbf{Re}\Sigma_{\rm Fock}(\omega+i\delta) \;\simeq\; -\Big(\frac{k_F U}{v_F}\Big)^2 \frac{\omega}{2(8\pi)^2}\frac{\omega_0^2}{E_F^2}\times\frac{E_F}{T}. \quad (4.36)$$

The velocity of quasi-particle might be obtained by Fourier transformation, $(2\pi)^{-1}\int d\omega G(\omega)\exp(i\omega t)$. One obtains a delta-funtion $\delta(r-v_F t)$ after the transformation. This indicates that the velocity of quasi-particle is v_F in the semi-classical regime, even in the presence magnetic field. In the presence of interaction, the spectrum of quasi-particle is corrected. Thus the propagator obtains interaction correction. Now the exponential part in $G(\omega)$ becomes $\exp i\Big(\omega-\mathbf{Re}\Sigma(\omega)\Big)r/v_F$, where Σ is the self-energy correction, containing both Hartree and Fock corrections. Then the Fourier transformation leads a delta function, $\delta\left((1-\partial_\omega \mathbf{Re}\Sigma|_{\omega=0})\, r - v_F t\right)$. Thus the velocity got renormalzied by the interaction to be $v_F/\left(1-\partial_\omega \mathbf{Re}\Sigma|_{\omega=0}\right) \simeq v_F(1+\partial_\omega \mathbf{Re}\Sigma|_{\omega=0})$. Since the field-dependence correction comes from Eq. 4.36, one then uses Eq. 4.36 to obtain the field-dependent correction to effective velocity.

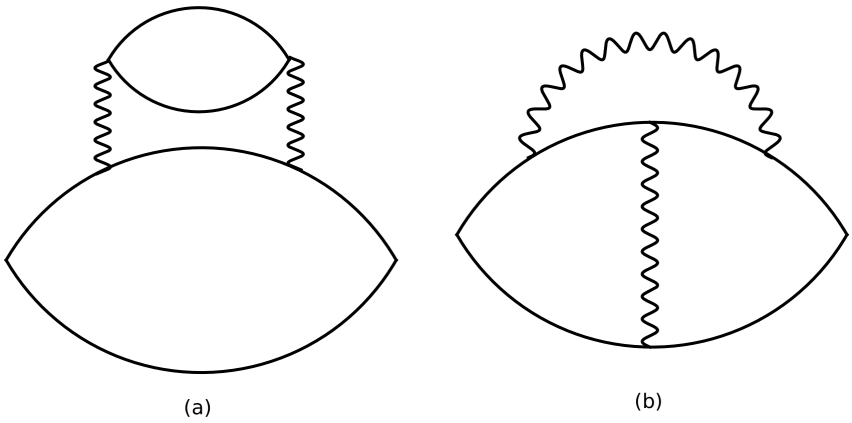

Figure 4.5: The Feynman diagrams representing the corrections to thermodynamic potential. (a) Hartree diagram. (b) Fock diagram.

4.7 Theromodynamic potential

According to the linked cluster theorem, the thermodynamical potential is reduced to the computation of closed Feynman diagrams. We employ perturbation theory in interactions and consider two leading diagrams depicted in Fig. (4.5). The calculation presented here is for a single spin. The Hartree term, given by the diagram Fig. (4.5)a, gives the following contribution to the potential

$$\Omega_a = -T \sum_{\nu_m} \Pi(i\nu_m)\Pi(i\nu_m). \tag{4.37}$$

Here $\nu_m = 2\pi m T$. The Fock term, depicted in Fig. (4.5)b, gives

$$\Omega_b = T^3 \mathbf{tr} \sum_{m,n,l} G(i\omega_m)G(i\omega_m - \nu_l)G(i\omega_m - \nu_l - i\nu_n)G(i\omega_m - i\nu_n). \tag{4.38}$$

4.7.1 Hartree diagram

Due to the chiral structure, the leading contribution to Ω_a is from the zero-momentum transfer. Upon summing over ν_m and defining dimensionless variable $x = 2\pi T r/v_F$, one obtains

$$\Omega_a = -vU^2T^3\frac{k_F^2}{\pi v_F^4}\int_{2\pi T/E_F}^{\infty}\frac{dx}{x}\frac{1}{(\sinh x)^2\tanh x}. \tag{4.39}$$

The integral $\int_{2\pi T/E_F}^{\infty}\frac{dx}{x}\frac{1}{(\sinh x)^2\tanh x} = c_0(2\pi T/E_F)^{-3} - c_1 + O(T/E_F)$. Here c_0 and c_1 are two constants. Importantly, one may write c_1 as a generic integral $c_1 = \int_0^{\infty}\frac{dx}{x}\Big[\frac{1}{x^3} - \frac{1}{(\sinh x)^2\tanh x}\Big]$ Numerically, it is approximately given by $c_1 \approx 0.121727$. Then we consider the specific heat per unit volume

$$C_v^a = \frac{1}{v}\frac{\partial\Omega_a}{\partial T}\Big|_v. \tag{4.40}$$

Obviously, the leading contribution comes from the $\propto c_1$ part. Thus we obtain

$$C_v^a = 3c\Big(\frac{k_FU}{v_F}\Big)^2\frac{T^2}{\pi v_F^2}. \tag{4.41}$$

This T^2 behavior is a typical property of 2D Fermi-liquids.

4.7.2 Fock diagram

Upon the summation over m, n, l in Eq. (4.38), we obtain the following integral expression

$$\Omega_b = \frac{vT}{(2\pi)^3}\Big(\frac{k_FU}{v_F}\Big)^2\frac{\omega_0^2}{2v_F^2}\int_{2\pi T/E_F}^{+\infty} zdz\frac{1}{\sinh^2 z\tanh z}. \tag{4.42}$$

The integral $\int_{2\pi T/E_F}^{+\infty} zdz\frac{1}{\sinh^2 z\tanh z} = a_0\frac{E_F}{T} - \frac{1}{2} + O(T^3/E_F^3)$. Here a_0 is a constant. Thus its contribution to specific heat, C_v^b, now reads

$$C_v^b \simeq -\frac{1}{(2\pi)^3}\Big(\frac{k_FU}{v_F}\Big)^2\frac{\omega_0^2}{4v_F^2}. \tag{4.43}$$

This is a constant correction to specific heat, which only depends on the magnetic field B, v_F, k_F and the interaction strength U_0.

4.8 Comparison with other magnetic mechanisms

4.8.1 Zeeman effect

In this section, we argue that the Zeeman effect gives subleading corrections to thermodynamics compared to the (pseudo)-spin phase. The Zeeman effect originate from the coupling $-\frac{1}{2}\mu_B B 1_4 \otimes \hat{\alpha}_z$. Here μ_B is the Bohr magneton and $\hat{\alpha}_z$ is the Pauli matrix acting on the (real-)spin of electron. Since energy is splitted by the Zeeman effect, each spin's Fermi momentum is different. Namely,

$$k_F^s = k_F + \frac{s}{2}\frac{\mu_B B}{v_F}, \tag{4.44}$$

where k_F is defined by ϵ_F/v_F. We find that the propagator is modified to be $G_{K,s}(\mathbf{r}, \delta w) \approx \frac{I_s}{2}\Big(1 + (\mathrm{sgn}(\omega) + \frac{i}{2k_F^s r})\hat{r}\cdot\hat{\sigma}\Big)$. Two observations: (1) The chiraly feature is not influenced by the Zeeman effect. (2) k_F^s enters the oscillatory function. This is the key point to consider the Zeeman effect. In fact, it affects the thermodynamic potential in the following way

$$\Omega_a^z = -TU_{2k_F}^2 \sum_{\nu_m} \int d^2 r \Pi_+(i\nu_m, r)\Pi_-(i\nu_m, r). \tag{4.45}$$

Here Ω_a^z is the correction to the thermodynamic potential by Zeeman effect and $\Pi_\pm$ is $2k_F$ polarization operator for spin up and down respectively. Here $\Pi_{2k_F}^s$ is the $2k_F$ polarization operator for the spin-up/down ($s = +/-$) electron. However, in Graphene, the $2k_F$-scattering is suppressed by chirality. In fact, $\Pi_{2k_F}^+(r)\Pi_{2k_F}^-(r)$ carries one extra decaying factor $(k_F r)^{-2}$. Since the characteristic scale for r is the thermal length v_F/T, the decaying factor then translates into a small factor, T^2/E_F^2.

In the Zeeman effect, the fundamental energy scale is $\omega_z = \mu_B B$. Set $B = x(T)$ and then ω_z given by

$$\omega_z = 9.27x \times 10^{-24} J. \tag{4.46}$$

The effective cyclotron-frequency is given by $\omega_0 = \hbar v_F/R_L$. If $k_F^{-1} \simeq 1.65$ nm, the Larmor radius given by $R_L \simeq \frac{400}{x} nm = 4 \times 10^{-7}/x(m)$. For simplicity, we take $v_F = 10^6 m/s$. Recall $\hbar \simeq 10^{-34} J \cdot s$. Then the energy scale ω_0 is estimated by

$$\omega_0 = \frac{x}{4} \times 10^{-21} J. \tag{4.47}$$

It is easy to see that $\omega_0 \gg \omega_z$.

From smallness of T^2/E_F^2 and ω_z/ω_0, one observes that the Zeeman effect gives parametrically smaller corrections compared to the effect coming from the pseudospin-dependent orbital phase.

4.8.2 Effect of the curved electron trajectory

In this section, we consider the effect of curving of the electron trajectory and argue that it gives a sub-leading correction to the thermodynamic characteristics of the interacting electron gas. Curving of the trajectory manifests itself in the two-loop diagram in the RPA sequence. Now we consider the correction to DOS and find that it is proportional to the following expression

$$P(\mathbf{r},\omega) = U_{2k_F}^2 u_0^2 \mathrm{tr} \int d^2r_1 d^2r_2 G(\mathbf{r},\mathbf{r}_1;\omega) G(\mathbf{r}_1,\mathbf{r}_2;\omega) G(\mathbf{r}_2,\mathbf{r};\omega) \Pi(\mathbf{r}_1;0) \Pi(\mathbf{r}_2;0), \tag{4.48}$$

where U_{2k_F} is the $2k_F$ component of interaction and u_0 is the strength of the point-like impurity. Since we focus on the effect trajectory, we only preserve the $p_0^3 r^3$-corrections and ignore the spin-dependent phase correction in P. We call this part as P_0, given by the following integral expression

$$\begin{aligned} P_0 = \quad & -\frac{\partial_\omega}{2} \mathrm{tr} \int d^2r_1 d^2r_2 \frac{1}{2\pi v_F^2 |\mathbf{r}_1 - \mathbf{r}_2|^2} \exp 2i \left((k_F + \frac{\omega}{v_F}) |\mathbf{r}_1 - \mathbf{r}_2| - \frac{p_0^3 |\mathbf{r}_1 - \mathbf{r}_2|^3}{24} \right) \\ & \times \frac{1}{4\pi^2 v_F r_1^3} \cos(2k_F r_1 - \frac{p_0^3 r_1^3}{12}) \times \frac{1}{4\pi^2 v_F r_2^3} \cos(2k_F r_2 - \frac{p_0^3 r_2^3}{12}) U_{2k_F}^2 u_0^2. \end{aligned} \tag{4.49}$$

In the exponential, the main oscillating term is $2k_F|\mathbf{r}_1-\mathbf{r}_2|\pm 2k_F r_1 \pm 2k_F r_2$. We only need the slowly oscillatory piece. Namely, we want $2k_F|\mathbf{r}_1-\mathbf{r}_2|\pm 2k_F r_1 \pm 2k_F r_2 \simeq 0$. This demands that $\mathbf{0}, \mathbf{r}_1, \mathbf{r}_2$ are aligned in a straight line. For simplicity, we take $\mathbf{r}_1/r_1 \simeq -\mathbf{r}_2/r_2$. Use the expression $|\mathbf{r}_1-\mathbf{r}_2| = |r_1+r_2|\sqrt{1-\frac{2r_1r_2}{|r_1+r_2|}(1+\cos\theta)}$ where θ is the angle bewteen $\mathbf{r}_1$ and $\mathbf{r}_2$. If $\theta \simeq \pi$, then $|\mathbf{r}_1-\mathbf{r}_2| \simeq r_1+r_2+\frac{r_1r_2}{2|r_1+r_2|}(\theta-\pi)^2$. Then the integral over θ introduces extra factor, shown as below

$$\int_{\theta\sim\pi} d\theta \exp(ik_F \frac{r_1r_2}{|r_1+r_2|}(\theta-\pi)^2) \approx e^{i\pi/4}\sqrt{\frac{\pi|r_1+r_2|}{k_F r_1 r_2}}. \tag{4.50}$$

We only trace the field-dependent correction, by considering $\delta P_0^a(B) = P_0^a(B) - P_0^a(0)$. Further we do the following variable change: $x = p_0 r_1$ and $y = p_0 r_2$. Here x and y are both dimensionless. Then δP_0^a is given by $U_{2k_F}^2 u_0^2 v_F^5 k_F^{-1/2} p_0^{-7/2} F_\Gamma(\omega/\epsilon_0)$ and F_Γ is given by

$$\begin{aligned} F_\Gamma \equiv & -i\int_{x,y>\Gamma} dxdy \left[\exp 2i\left(\frac{\omega}{\epsilon_0}(x+y) - \frac{[x^2y+xy^2]}{8}\right) - \exp 2i\left(\frac{\omega}{\epsilon_0}(x+y)\right)\right] \\ & \times \frac{1}{4\pi^2x^2} \times \frac{1}{4\pi^2y^2} \times e^{i\pi/4}\sqrt{\frac{\pi}{xy(x+y)}}, \end{aligned} \tag{4.51}$$

where $\Gamma \ll 1$ is small cut-off with order of p_0/k_F and $\epsilon_0 = v_F p_0$. Numerically, we trace the Γ-independent term, namely $F(\omega/\epsilon_0)$ and find that $F(\omega/\epsilon_0)$ is smooth function of ω/ϵ and has the amplitude that is smaller than 1. Thus, we conclude that the curved trajectory give a correction to the DOS with a coefficient, $\propto B^{7/2}$. Since we consider a weak magnetic field, the $B^{7/2}$ is obviously the high order perturbation relative to B^2. Further, $F(\omega/\epsilon_0)$ is smooth and smaller than 1, while E_F^2/ω^2 is large. Thus the effect of curved trajectory gives the sub-leading corrections.

4.9 Conclusions

Our main finding is that, for two-dimensional Dirac electrons, application of a weak magnetic field enhances significantly the many-body effects. This is unlike the

conventional 2D electron gas. The reason for this is the pseudospin-dependent magnetic correction in Dirac electron propagators, $\sim \hat{\Sigma}_z \varphi(r)$. For many-body effects to unfold, the energy, ω, measured from the Fermi level should exceed $\omega_0 = v_F(k_F l^2)^{-1}$, which is the inter-Landau-level distance at the Fermi level. We have only considered the low-temperature properties of interacting electrons in the doped graphene, so that the interaction with phonons[174, 175] can be neglected.

Our predictions for observables given by Eqs. 4.18-4.22 and by Eq. 4.7 all emerge as a result of evaluation of the Fock diagrams illustrated in Figs. 4.2a, 4.2c. It is nontrivial that, while these diagrams are not leading and even do not belong to the RPA sequence, they are responsible for the sensitivity to a weak magnetic field. Importantly, the higher-order diagrams,while leading to the renormalization of the interaction vertex, do not modify thepredicted ω, T-dependencies.

Other origin of the B-dependence of the interaction effects is either spin via the Zeeman splitting coming from spin or or the orbital effect via the curving of the electron trajectories in magnetic field. We have checked that these two mechanisms lead to the B-dependent corrections which are sub-leading compared to the ones originating from the pseudospin-dependent phase of Dirac propagators.

Finally, we emphasize that our results apply for the doped graphene, where the Fermi energy is far away from the neutrality. The condition $\omega \gg \omega_0$ in the present chapter is automatically violated at neutrality. The question about $\nu = 0$ Landau level is interesting and remains open[176].

CHAPTER 5

BALLISTIC MAGNETOTRANSPORT IN GRAPHENE

The text of this chapter has been adapted from Ref [150].

5.1 Introduction

Two well-established regimes characterize low-temperature magnetoresistance in a two-dimensional metallic system: Weak localization[177, 178] (WL) and Shubnikov–de Haas (SdH) oscillations. WL dominates in the low field limit $\omega_0\tau < (k_F L)^{-1}$. Here ω_0 is the cyclotron-frequency, τ is the impurity scattering time, and $L = v_F\tau$ is the mean free path. This regime is reached when the magnetic flux threading the area $L^2/2$ is smaller than the flux quantum[179, 180]. In the high field limit $\omega_0\tau > 1$, the spectrum is fully quantized into the Landau levels, and SdH oscillations become the dominating effect. The crossover between two limits is $(k_F L)^{-1} < \omega_0\tau < 1$, where the magnetic field B is non-quantizing. In this regime, the electron-electron interaction (EEI) are believed to play a significant role[181]. Namely, the interaction correction to the conductivity induce the B-dependence in the resistivity via the relation,

$$\delta\rho_{int} \simeq \rho_0^2(\omega_0^2\tau^2 - 1)\delta\sigma_{int}. \tag{5.1}$$

Here ρ_0 is the Drude resistivity and $\delta\sigma_{int}$ is the interaction correction to the longitudinal conductivity.

At the non-quantizing regime, magnetoresistance in the doped graphene has been widely studied in experiments[182, 183, 184, 185, 186] in the last decade while theoretical investigations are still absent. One may expect that the B-dependence in $\delta\rho_{int}$

is simply product of $\rho^2\omega_0^2\tau^2$ and zero field performance in $\delta\sigma_{int}$. However, it is not the complete story. We have shown that the non-quantizing field on Dirac electrons has non-trivial effects on FO and many-body physics.

In this chapter, we report that $\delta\sigma_{int}$ itself can carry field-dependent corrections and thus leads to non-trivial magnetoresistance in graphene. In the ballistic regime $T\tau > 1$ of the doped graphene[187, 186], we find

$$\delta\sigma_{int} \simeq \lambda_0 \frac{e^2\tau}{\pi}\Big(tT - p\frac{\omega_0^2}{48T}\Big). \tag{5.2}$$

Here λ_0 is the dimensionless interaction parameter, and t, p are dimensionless parameters determined by the disorder potential. Information about t and p can be extracted from the zero-bias anomaly[164] of tunneling density of states. The correction is present in a wide parameter range, where $\max(\omega_0, \tau^{-1}) < T < E_F$. Here E_F is the Fermi energy. From Eq. 5.1, the field-dependent correction to the resistivity reads,

$$\delta\rho_{int}(B) - \delta\rho_{int}(0) \simeq \lambda_0\omega_0^2 \frac{e^2\tau^2\rho_0^2}{\pi}\left(tT\tau + \frac{p}{48T\tau}\right). \tag{5.3}$$

Temperature dependence of magnetoresistance in Eq. 5.3 highly depends on the ratio, p/t, of two disorder parameters that will be defined below. Generally, the ratio p/t can be any real number larger than $-1/2$. One prominent case is the scalar-like disorder potential, for which p/t is $\to +\infty$. To ensure the second term is not always subleading, we will focus on $p/t > 1$, where the disorder can be regarded as a perturbation around a scalar-like potential. When $1 < T\tau < \sqrt{p/t}$, the temperature dependence in magnetoresistance becomes reciprocal instead of being linear. Therefore, the parabolic curve in magnetoresistance becomes more flattened when T increases. See Fig. 5.1. Below, we present a qualitative explanation of the observed effect.

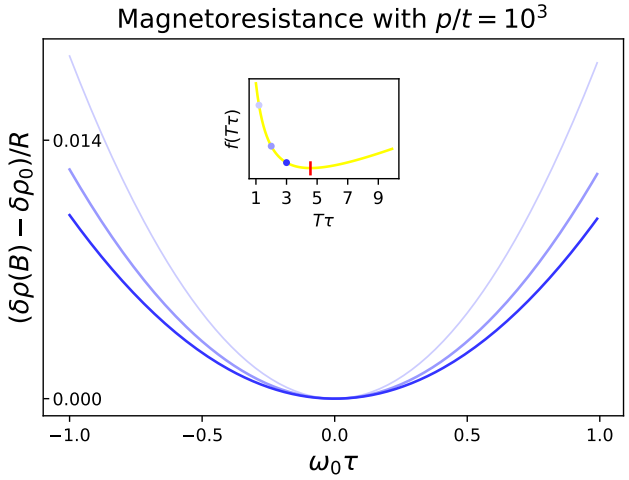

Figure 5.1: Magnetoresistance, $[\delta\rho_{int}(B) - \delta\rho_{int}(0)]/R$, is plotted versus the dimensionless variable $\omega_0\tau$. The sign of $\omega_0\tau$ indicates the direction of the magnetic field and $R \equiv \lambda_0 e^2\rho_0^2/\pi$. Each curve correspond to the resistance plotted at a corresponding temperature shown by (blue) dots in the inset. From light to dark curves, the temperature is increasing while the curvature is decreasing. Values of temperature are pointed out in the inset. The inset depicts the function $f(T\tau) = tT\tau + p/48T\tau$ from Eq. 5.3. The (red) vertical bar locates the minimum of the function.

5.2 Qualitative discussion

Coherent scatterings off Friedel oscillations of electron density at distances $r \gg k_F^{-1}$ from an impurity renormalize the transport relaxation time. The coherent scattering is illustrated in Fig. 5.2. This process, leads to non-trivial temperature dependence[188, 189] in $\delta\sigma_{int}$. In two-dimensional electron gas (2DEG), $\delta\sigma_{int}$ is $\sim T\tau$ in the ballistic limit $T\tau > 1$ and $\sim \ln(T\tau)$ in the diffusive limit $T\tau < 1$.

Dirac nature of electrons in graphene [190, 191, 192, 167, 193, 28, 119, 29, 194, 195, 196, 159, 197, 198, 199, 200, 201, 202] can enrich the process of coherent scatterings because of the Berry phase π and chiral symmetry of Dirac electrons. Note that backscatterings off a single impurity can be classified into two types of Feynman diagrams. The first one is a loop type, giving Friedel oscillations. See inset (a) in Fig. 5.2. Here, the Berry phase π of Dirac electron leads to a faster decaying FO[102]. The second one is a vertex type diagram, yielding the correction to the density matrix.

See inset (b) of Fig. 5.2. Here, the matrix structure of Dirac electron induces sensitivity of the vertex correction to the nature of disorder[164]. Two properties together lead to the well-known result that the temperature dependence in the conductivity in the ballistic limit is still $\sim T\tau$ but very sensitive to the disorder[102]. Importantly, if the disorder is scalar-like, the leading temperature behavior $\sim T\tau$ vanishes.

The presence of a weak magnetic field changes the scenario for both backscatterings in (a) and (b) from the inset of Fig. 5.2. The persistent FO emerges from loop correction,

$$\delta n(r) = \frac{g k_F}{2\pi^2 v_F r^2}\left[\frac{1}{k_F r}\cos\Big(2k_F r - \frac{r^3}{12 k_F l^4}\Big) + 2\varphi^2(r)\sin\Big(2k_F r - \frac{r^3}{12 k_F l^4}\Big)\right]. \quad (5.4)$$

Here the parameter g is defined in terms of the impurity potential, $\hat{V}_{\mathbf{r}}$, as $g = \mathrm{tr}\int d^2 r \hat{V}_{\mathbf{r}}/4$, $\varphi(r) = \omega_0 r/2v_F$ and l is the magnetic length. The $\varphi(r)$ is the half of the angle of the arc, corresponding to the Dirac electron traveling from $\mathbf{0}$ to $\mathbf{r}$ in a weak magnetic field. See Fig. 5.2. The value $\varphi(r)$ reflects the strength of chiral symmetry breaking semi-classically[120]. A similar correction also emerges for the vertex correction. To evaluate the effect of the magnetic field on other physical processes[203] for Dirac electrons, employing the chiral-symmetry breaking phase $\varphi(r)$ could be essential as it could lead to novel observable effects.

As the next step, we will consider the transport relaxation time and see that the incorporation of $\varphi^2(r)$ into the estimate of the relaxation time can generate the correction in Eq. 5.2. It will help us to qualitatively extract the temperature behavior of magnetoconductivity from its relation to the transport time[204].

At first, let us estimate the relaxation time at zero-field, where a linear temperature dependence emerges:

$$\frac{1}{\tau} = \int \frac{d\theta}{2\pi}(1-\cos\theta)|f_0 + f_1(\theta)|^2. \quad (5.5)$$

Here f_0 and f_1 are respectively the scattering amplitudes off impurities and impurity-induced potentials. In the absence of the magnetic field, according to Refs. [189] and [147], the function f_1 can be cast as an integral $f_1(\theta) = \int drF(r)$ and

$$F(r) = -\lambda_0 g \int_0^{+\infty} dr \frac{r_T}{\sinh r/r_T} \sin(2k_F r) J_0(qr). \tag{5.6}$$

Here $r_T = v_F/(2\pi T)$ is the thermal length, $|q| = 2k_F \sin\theta/2$ and J_0 is the zero Bessel function. The coefficient λ_0 is the dimensionless interaction parameter and the main contribution to Eq. 5.5 comes from the region $\theta \sim \pi$. One can expand $\theta = \pi + \delta\theta$ and $q \simeq 2k_F - k_F\delta\theta^2$. The condition $k_F\delta\theta^2 r_T \sim 1$ translates into $\delta\theta \sim (k_F r_T)^{-1/2}$. With the asymptotic expression of Bessel function, the power counting in the integral becomes $r^{-3/2}$ when $r < r_T$. When $\delta\theta < (k_F r_T)^{-1/2}$, the integral in Eq. 5.6, gives $\sim (k_F r_T)^{-1/2}$. Thus the integral in Eq. 5.5 is estimated by $(k_F r_T)^{-1}$. This indicates that the interaction correction to τ is proportional to T and the corresponding correction to $\delta\sigma_{int}$ is also linear in T.

In the presence of a magnetic field, the trajectories of electrons are curved, and the chiral symmetry of Dirac electrons is broken. Thus the suppressed backscattering is enhanced by the magnetic field. The incorporation of the symmetry-breaking effect leads to field-dependent correction to the scattering amplitude. Namely, $f_1 \to f_1 + \delta f_1$ and δf_1 is given by $\int drF(r)\varphi^2(r)$. Here $\varphi^2(r)$ changes power counting to $r^{1/2}$ and the integral gives $\sim \omega_0^2 (k_F r_T)^{3/2}$. The θ-integral remains the same. Thus the field-dependent corrections to τ and $\delta\sigma_{int}$ are proportional to $\omega_0^2 T^{-1}$.

Below, we rigorously trace the current-current correlation function to derive the temperature-dependence in $\delta\sigma_{int}$.

5.3 Magnetoconductivity from Kubo formula

The static conductivity can be evaluated from the current-current correlation function[204]. Namely, $\sigma_{\alpha,\beta} = \lim_{\omega\to 0} \frac{i}{\omega}\Pi_{\alpha,\beta}(\omega)$. Here the $\Pi_{\alpha,\beta}(\omega)$ is obtained by

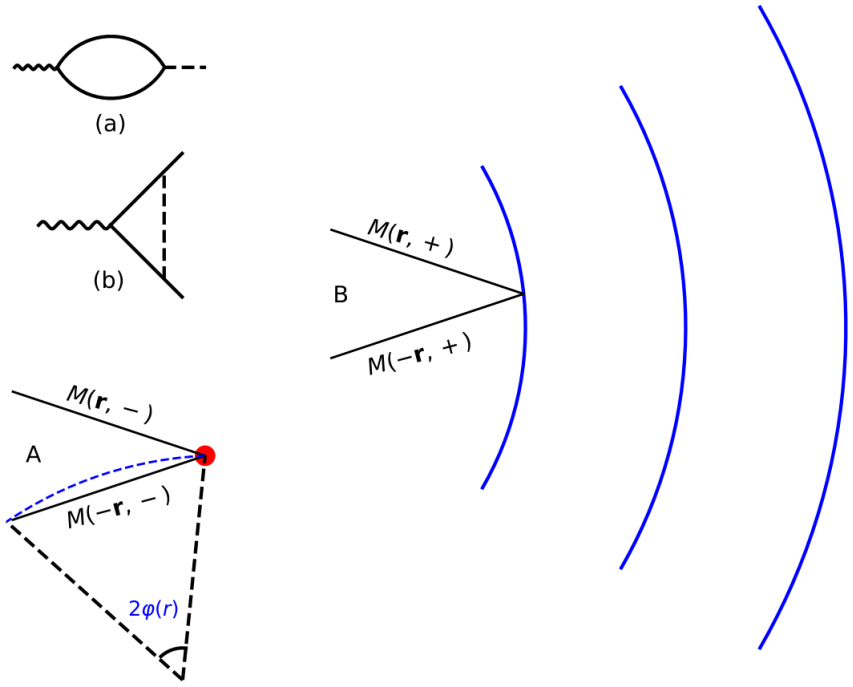

Figure 5.2: Coherent scatterings between A and B paths: A is the path of backscattering off an impurity while B is the path when electrons hit the Friedel oscillations (or modulation of density matrix introduced by impurities), presented by blue curves. In the presence of a magnetic field, the path is curved, shown by the dashed arc. The angle of the arc is $2\varphi(r) = \omega_0 r/v_F$. Due to the Dirac nature of electrons, each propagator carries a matrix M. The inset plots two types of backscatterings off an impurity : (a) the loop type that creates Friedel oscillations. (b) the vertex type that creates correction to the density matrix.

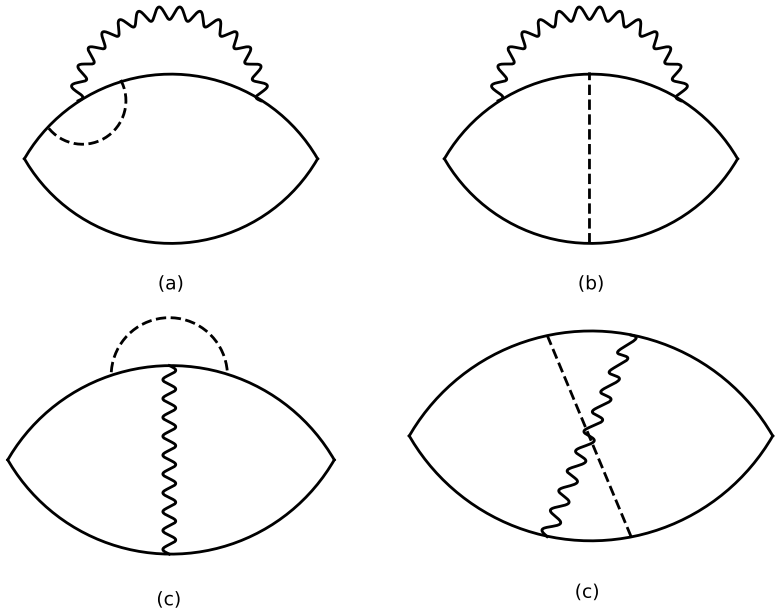

Figure 5.3: Feynman diagrams giving leading field-dependent corrections to the longitudinal static conductivity. Solid lines represent the Feynman propagators. Dashed lines are the static impurities, while the wavy lines represent the electron-electron interactions.

taking analytic continuation of current-current correlation function $\Pi_{\alpha,\beta}(i\Omega_n)$ via $i\Omega_n \to \omega$, $\Pi_{\alpha,\beta}(i\Omega_n) = \int_0^{1/T} d\tau \langle T_\tau \hat{j}_\alpha(\tau)\hat{j}_\beta(0)\rangle e^{i\Omega_n\tau}$ Here $\hat{j}_\alpha(\tau)$, $\alpha = 1, 2$, is the current operator at imaginary time τ, $\omega_n = 2\pi Tn$ is the bosonic Matsubara frequency and $i\Omega_n \to \omega$ represents the analytic continuation.

At finite doping, one can treat impurity and interaction potential as the perturbation to $\hat{H}_0$. Here H_0 is the Dirac Hamiltonian coupled to $U(1)$ gauge field,

$$\hat{H}_0 = v_F \int d^2\mathbf{r}\hat{\Psi}^\dagger(\mathbf{r})[\hat{\Sigma}_\alpha(-i\partial^\alpha + eA^\alpha)]\hat{\Psi}(\mathbf{r}). \tag{5.7}$$

Here α is summed in x and y, v_F is the Fermi velocity, $\hat{\Psi} = (\hat{\psi}_{AK}, \hat{\psi}_{BK}, \hat{\psi}_{BK'}, \hat{\psi}_{AK'})$ is the 4-component fermion operator and $\hat{\Sigma}_{x,y} = \hat{\tau}_z \otimes \hat{\sigma}_{x,y}$, where $\hat{\tau}_z$ is the third Pauli matrix acting in K, K' space and $\hat{\sigma}_{x,y}$ are Pauli matrices acting in the space of A, B sublattices. The gauge field is adopted by $\mathbf{A} = (-eBy, 0)$.

Now, we consider the Gaussian-correlated potential. Meanwhile, the symmetry-allowed disorder potential is described by five parameters[103, 101, 205], namely,

$$\langle \hat{V}_{\mathbf{r}} \otimes \hat{V}_{\mathbf{r}'} \rangle = \delta_{\mathbf{r},\mathbf{r}'} \Big[\gamma_0 \hat{I} \otimes \hat{I} + g_i^m \hat{Q}_m^i \otimes \hat{Q}_m^i \Big] \tag{5.8}$$

Here $\hat{V}_{\mathbf{r}}$ is the impurity potential and the bracket $\langle ... \rangle$ is the average over impurity distributions. $\hat{I}$ is the identity matrix. Here $\hat{Q}_m^i = \hat{\Sigma}_m \hat{\Lambda}_i$ and $\hat{\Sigma}_z = \hat{\tau}_0 \otimes \hat{\sigma}_z, \hat{\Lambda}_x = \hat{\tau}_x \otimes \hat{\sigma}_z, \hat{\Lambda}_y = \hat{\tau}_y \otimes \hat{\sigma}_z, \hat{\Lambda}_z = \hat{\tau}_z \otimes \hat{\sigma}_0$. We adpot the notation from Ref. [103], $g_z^z = \gamma_z$, $g_z^{x,y} = \gamma_\perp$, $g_{x,y}^z = \beta_z$ and $g_{x,y}^{x,y} = \beta_\perp$. Effectively, γ_0 represents the square of the strength of static electric potential averaged over the A/B sublattice. Parameters β_z and $\beta_\perp$ introduce the intervalley scatterings while $\gamma_\perp$ introduces the hopping between A and B sublattices. The parameter γ_z creates a chemical potential difference between the A/B sublattices. To clarify terminology, we refer to the impurity potential from γ_0 term as the scalar potential while all other terms in the potential as non-diagonal.

To illustrate coherent scattering quantitatively, we use the semiclassical expression of Dirac propagators in the real space $\langle G(\mathbf{r}, \omega) \rangle \sim e^{i\mathrm{sgn}(\omega)\Phi_0(r) - r/(2\tau v_F)} M(r, \mathrm{sgn}(\omega))/k_F r$. Here $\Phi_0(r)$ is the phase including both $k_F r$ and the magnetic phase[134, 206]. The form of matrix M shows that chiral-symmetry is broken in each valley but it is preserved in the Brillouin zone. The field-dependent part in M reads, $M - M_0 \simeq -\varphi^2(r)\hat{I}/2 - i\mathrm{sgn}(\omega)\varphi(r)\hat{\Sigma}_z$. Here M_0 is the value of matrix M in the absence of field and $\hat{I}$ is the identity matrix.

Applying perturbations, one finds that a series of Feynman diagrams led to dominant contributions to the conductivity. Up to the lowest orders of the impurity potential and interactions, we find that the diagrams in Fig. 5.3 give the leading field-dependent corrections to the longitudinal and static conductivity, $\delta\sigma_{xx}$. Namely, these are diagrams that contain vertex corrections, while others in the same order of perturbation theory are subleading.

The exact expression corresponding diagrams in Fig. 5.3 can be simplified. In the leading in $(T\tau)^{-1}$ order, and upon neglecting highly-oscillatory $\sim \exp i2k_F r$ terms, one arrives at a short expression for the conductivity correction,

$$\delta\sigma_{xx} \simeq -\lambda_0 \frac{e^2\tau}{\pi^2\alpha_{\rm tr}} \int_0^{E_F} d\Omega \frac{d}{d\Omega}\Big(\Omega \coth\frac{\Omega}{2T}\Big) {\rm Im} I(\Omega). \tag{5.9}$$

Here the function $I(\Omega)$ is expressed by the integral, $I(\Omega) = \int y^{-1} dy \Big(2p'\varphi^2(y) + t'\Big) e^{2i(\Omega+i\tau)y/v_F}$, $\lambda_0 = k_F U_0/2\pi v_F$ is the dimensionless interaction constant at zero momentum. Parameters p' and t' are defined by $p' = \gamma_0 - \beta_z - \gamma_z$ and $t' = 2\gamma_z + 2\beta_z + \beta_\perp + \gamma_\perp$. The expression of $I(\Omega)$ originates from the coherent scatterings in Fig. 5.2. Notice the constant t' does not contain γ_0, while p', representing the enhancement of backscattering, depends on γ_0. For short-ranged and weak scatterers, the parameter $\alpha_{\rm tr}$ is found to be $\alpha_{\rm tr} = \gamma_0 + 4\beta_\perp + 2\gamma_\perp + 2\beta_z + \gamma_z$, determining the Drude conducitivty in graphene[205].

The integration in the expression of ${\rm Im}I(\Omega)$ can be analytically performed, giving

$${\rm Im} I(\Omega) = \frac{\pi t}{2} + p\frac{(\omega_0\tau)^2}{4}\frac{\Omega\tau}{(1+\Omega^2\tau^2)^2}. \tag{5.10}$$

The zero-field part shares the same integration as in Ref. [189]. The linear T-dependence in $\delta\sigma_{xx}$ at the zero-field is obtained from the property, $\lim_{\Omega\to 0} \Omega\coth\Omega/2T \simeq 2T$. The sensitivity to the disorder potential in the zero-field limit, namely the sensitivity to parameter t, agrees well with the result in Ref. [102].

The field-dependent correction in Eq. 5.9 mainly originates from the region $0 < \Omega < 2T$. In this region, one can linearize $\frac{d}{d\Omega}\Big(\Omega\coth\frac{\Omega}{2T}\Big) \simeq \Omega/3T$. Notice that the charateristic scale for Ω in Eq. 5.10 is $\sim \tau^{-1}$. The integral over Ω does not introduce extra temperature dependence. Thus the field-dependnet correction $\delta\sigma_{xx}$ is $\sim \omega_0^2 T^{-1}$. Tracing the integral rigorously, one can obtain Eq. 5.2, where we define $t = t'/\alpha_{\rm tr}$ and $p = p'/\alpha_{\rm tr}$. Inverting the magnetoconductivity tensor gives us

Eq. 5.3, which is the main result of the present work. The result is specific for Dirac electron and valid in a large parameter space when $\omega_0 < T < E_F$. We provide the comparison between the mechanism reported here and the hydrodynamics description[207, 208, 209, 210, 211, 212, 213, 214, 31], which is the recent focus of studies on the transport of graphene. We show that for the doped and ultra-clean sample, the reported ballistic magnetotransport mechanism is the dominating effect when the temperature, T, within the logarithmic accuracy, lies in a parametrically large interval $\left(\frac{k_B}{\hbar\tau}\right) \lesssim T \lesssim \left(\frac{k_B}{\hbar\tau}\right)\left[\frac{\hbar E_F\tau}{k_B \ln(\hbar E_F\tau/k_B)}\right]^{1/2}$ (from now on we restore $k_B/\hbar$ prefactor in the expression for T).

The present technological capabilities do not allow one to engineer the graphene samples with a given impurity type to the best of our knowledge. Therefore, the present theory allows extracting the information about the impurity in the sample from the magnetotransport measurement. Namely, upon fitting the temperature dependence of observed magnetoresistance with Eq. 5.3, one can extract the ratio of p/t. This helps to understand if the impurity in the given sample is mostly scalar type ($p/t \gg 1$) or mostly non-diagonal ($p/t \lesssim 1$).

5.4 Evaluation of the conductivity

5.4.1 Basic formulas for static conductivity

In this section, we present the definitions and the main formulas for static conductivity. The Dirac electron in graphene, coupled to $U(1)$ gauge field, is described by the Hamiltonian,

$$\hat{H}_0 = v_F \int d^2\mathbf{r}\hat{\Psi}^\dagger(\mathbf{r})[\Sigma_\alpha(-i\partial^\alpha + eA^\alpha)]\hat{\Psi}(\mathbf{r}). \tag{5.11}$$

Here a summation is assumed over the repeating index, α, with $\alpha = x, y$, v_F is the Fermi velocity, $\hat{\Psi} = (\hat{\psi}_{AK}, \hat{\psi}_{BK}, \hat{\psi}_{BK'}, \hat{\psi}_{AK'})$ is the 4-component fermion operator.

The four-dimensional matrix $\Sigma_{x,y} = \tau_z \otimes \sigma_{x,y}$, where τ_z is the third Pauli matrix acting on K, K' space and $\sigma_{x,y}$ are Pauli matrices acting on the space of A, B sublattices. Then the current operator for Dirac electrons is given by $ev_F \hat{\Psi}^\dagger(\mathbf{r}) \Sigma_\alpha \hat{\Psi}(\mathbf{r})$.

Now consider the system with the disorder potential $V_{\rm imp}(\mathbf{r})$ and the interaction potential $U(\mathbf{r})$. We assume the correlation of the disorder potential is point-like. Namely,

$$\begin{aligned}\langle V_{\rm imp}(\mathbf{r}) \otimes V_{\rm imp}(\mathbf{r}')\rangle_I = \delta_{\mathbf{r},\mathbf{r}'} \Big[& \gamma_0 1_4 \otimes 1_4 + \beta_\perp \Sigma_{x,y}\Lambda_{x,y} \otimes \Sigma_{x,y}\Lambda_{x,y} \\ & + \gamma_\perp \Sigma_{x,y}\Lambda_z \otimes \Sigma_{x,y}\Lambda_z + \beta_z \Sigma_z \Lambda_{x,y} \otimes \Sigma_z \Lambda_{x,y} + \gamma_z \Sigma_z \Lambda_z \otimes \Sigma_z \Lambda_z \Big] \end{aligned} \tag{5.12}$$

The bracket $\langle ... \rangle_I$ is the average over impurity distributions. Matrices above are defined by $\Sigma_z = \tau_0 \otimes \sigma_z, \Lambda_x = \tau_x \otimes \sigma_z, \Lambda_y = \tau_y \otimes \sigma_z, \Lambda_z = \tau_z \otimes \sigma_0$.. The γ_0, $\beta_\perp$, $\gamma_\perp, \beta_z$ and γ_z describe the strength of disorder potential.

According to the Kubo formula, the static conductivity is estimated by the current-current correlation function, $\sigma_{\alpha,\beta} = \lim_{\omega \to 0} \frac{i}{\omega} \Pi_{\alpha,\beta}(\omega)$. Here the $\Pi_{\alpha,\beta}(\omega)$ is obtained by taking analytic continuation of $\Pi_{\alpha,\beta}(i\Omega_n)$ via $i\Omega_n \to \omega$,

$$\Pi_{\alpha,\beta}(i\Omega_n) = \int_0^{1/T} d\tau \langle T_\tau \hat{j}_\alpha(\tau) \hat{j}_\beta(0) \rangle e^{i\Omega_n \tau} \tag{5.13}$$

Here $\hat{j}_\alpha(\tau)$, $\alpha = 1, 2$, is the current operator at imaginary time τ, $\omega_n = 2\pi T n$ is the bosonic Matsubara frequency and $i\Omega_n \to \omega$ represents the analytic continuation.

We treat the electron-electron interaction as the perturbation to H_0. The current-current correlation function can be generally expressed by

$$\begin{aligned}\Pi_{\alpha,\beta}(i\Omega_n) &= -T \sum_{i\omega_m} J_\alpha G(i\omega_m) J_\beta G(i\omega_m - i\Omega_n) \\ &- T \sum_{i\omega_m} J_\alpha G(i\omega_m) \Gamma_\beta(i\omega, i\omega - i\Omega_n) G(i\omega_m - i\Omega_n) \end{aligned} \tag{5.14}$$

where $\omega_m = (2\pi m + 1)T$ is the fermionic Matsubara frequency and Γ is the vertex correction. The current operator of Dirac electrons J_α above reads $J_\alpha = ev_F\Sigma_\alpha$. Here G is the exact green function for the interacting system. The first term in the RHS is of the self-energy type and the second term contains the vertex correction. Below we refer to the self-energy/vertex-type contributions to $\sigma_{\alpha,\beta}$ as to $\sigma^{S/V}_{\alpha,\beta}$.

The standard analytic continuation procedure transform the summation over Matsubara frequency in $\sigma^S_{\alpha,\beta}$ into a single variable integral,

$$\sigma^S_{\alpha,\beta} = \frac{1}{4\pi}\mathrm{Re}\int_{-\infty}^{+\infty} d\epsilon\partial_\epsilon\left[\tanh\frac{\epsilon}{2T}\right]\Big[J_\alpha G_R(\epsilon)J_\beta G_A(\epsilon) - J_\alpha G_R(\epsilon)J_\beta G_R(\epsilon)\Big] \quad (5.15)$$

Here $G_{R/A}$ is the retarded/advanced Green's function. Consider the first order perturbation over the interactions. There are two types of diagrams, Hartree and Fock. The diagrams a and b in Fig. 5.3 of maintext are of the Fock type. Here, we only focus on the calculation of Fock self energy, $\Sigma_F(i\omega_m) = T\sum_{i\nu_l} G_0(i\omega_m - i\nu_l)V(i\nu_l)$. Here ν_l is the bosonic Matsubara frequency, G_0 is the Green's function for non-interacting Hamiltonian H_0 and $V(i\nu_l)$ is the interaction potential in the frequency space (up to first order in perturbation, $V(i\nu_l)$ is simply constant V, not depending on frequencies). Inserting the self-energy Σ_F into Eq. 5.15 and performing analytic continuation, one obtains

$$\begin{aligned}\sigma^S_{\alpha,\beta} \simeq \frac{V}{4\pi^2}\ \mathrm{Im}\int d\Omega\frac{d}{d\Omega}\Big(\Omega\coth\frac{\Omega}{2T}\Big)\Big[&J_\alpha G_R(\epsilon)V(\Omega)G_A(\epsilon-\Omega)G_R(\epsilon)J_\beta G_A(\epsilon) \\ &-J_\alpha G_R(\epsilon)V(\Omega)G_R(\epsilon-\Omega)G_R(\epsilon)J_\beta G_A(\epsilon) - J_\alpha G_R(\epsilon)V(\Omega)G_A(\epsilon-\Omega)G_R(\epsilon)J_\beta G_R(\epsilon)\Big].\end{aligned} \quad (5.16)$$

Similarly, one could perform the analytic continuation in the vertex correction and find

$$\sigma^V_{\alpha,\beta} = \frac{T}{4\pi}\mathrm{Re}\int d\epsilon\Big[\partial_\epsilon\tanh\frac{\epsilon}{2T}\Big]J_\alpha\Big[G_R(\epsilon)\Gamma_\beta(\epsilon+i\delta,\epsilon-i\delta)G_A(\epsilon) - G_R(\epsilon)\Gamma_\beta(\epsilon+i\delta,\epsilon+i\delta)G_R(\epsilon)\Big],$$

where δ is an arbitrary small positive number. Diagrams c and d in Fig. 5.3 of the maintext are of the vertex type. The first order vertex correction reads $\Gamma_\beta(i\omega_m, i\omega_m - i\nu_n) = VT\sum_{i\nu_l} G_0(i\omega_m - i\nu_l)J_\beta G_0(i\omega_m - i\nu_l - i\nu_n)$. Performing the analytic continuation for $i\omega$, $i\nu$ and inserting the expression of Γ , one finds

$$\sigma^V_{\alpha,\beta} \simeq \frac{1}{8\pi^2}\,\mathrm{Im}\int d\Omega \frac{d}{d\Omega}\Big(\Omega\coth\frac{\Omega}{2T}\Big)\times J_\alpha\Big[2G_R(\epsilon)V(\Omega)G_A(\epsilon-\Omega)J_\beta G_A(\epsilon-\Omega)G_A(\epsilon) - G_R(\epsilon)V(\Omega)G_A(\epsilon-\Omega)J_\beta G_A(\epsilon-\Omega)G_R(\epsilon)\Big]. \tag{5.17}$$

5.4.2 Interaction corrections to static longitudinal conducitivity

This section provides a detailed calculation to derive the main temperature dependence in the static longitudinal conductivity, $\delta\sigma$. Taking all four diagrams into consideration, we find that the leading correction to σ in the ballistic regime ($T\tau \gg 1$) is given by

$$\delta\sigma \simeq \frac{V}{2\pi^2}\,\mathrm{Im}\int d\Omega \frac{d}{d\Omega}\Big(\Omega\coth\frac{\Omega}{2T}\Big)\mathrm{tr}\Big[J_\alpha G_R(\epsilon) V_{\mathrm{imp}}G_R(\epsilon)V(\Omega)G_A(\epsilon-\Omega)V_{\mathrm{imp}}G_A(\epsilon-\Omega)G_R(\epsilon)J_\beta G_A(\epsilon)\Big]. \tag{5.18}$$

Here V_{imp} represents the impurity potential. Thus the main task is to evaluate the Eq. 5.18. Here we adopt the semiclassical limit to estimate Eq. 5.18. In the semiclassical limit, the interaction potential acts as a touching potential. The real space Green's function averaged over impurities, reads

$$\langle G(\mathbf{r},\omega)\rangle_I = \frac{k_F}{2v_F}\sqrt{\frac{1}{2k_F r}}e^{i\mathrm{sgn}(\omega)\Phi_0(r)-r/(2\tau v_F)}M, \tag{5.19}$$

where the phase $\Phi_0(r) = k_F r + \omega r/v_F + \pi/4 - r^3/(24k_F l^4)$ and the matrix M is given by

$$M(\mathbf{r},\mathrm{sgn}(\omega)) \simeq \big(\mathrm{sgn}(\omega) + i(2k_F r)^{-1}\big)\,\hat{r}\cdot\mathbf{\Sigma} + \hat{I} - i\mathrm{sgn}(\omega)\varphi(r)\hat{\Sigma}_z - \frac{\varphi(r)^2}{2}\hat{I}, \tag{5.20}$$

where $\mathbf{\Sigma} = (\Sigma_x, \Sigma_y)$ and $\hat{I}$ is the identity matrix. Here $\varphi(r) = \omega_0 r/(2v_F)$ is the half of the angle corresponding to the arc of the Larmour circle with length r. The angle $\varphi(r)$ represents the extent of the chiral symmetry breaking, since Σ_z anti-commutes with $\Sigma_{x,y}$.

To perform real space integration in the expression for the conductivity, one may make use of the following identity

$$\int d^2x G_R(\mathbf{x}', \mathbf{x}; \epsilon)\hat{\Sigma}_\alpha G_A(\mathbf{x}, \mathbf{y}; \epsilon) = -\frac{i\tau}{k_F}\frac{\partial}{\partial x'_\alpha}\Big[G_A - G_R\Big](\mathbf{x}', \mathbf{y}; \epsilon), \tag{5.21}$$

where $\alpha = 1, 2$. This identity helps us in Eq. 5.18 bringing the convolution of two propagators into one around the vertex. Applying Eq. 5.21 twice (once for J_α and once for J_β), one arrives at

$$\begin{aligned}\delta\sigma \;&\simeq\; -\frac{e^2\tau^2 k_F^2}{64\pi^2 v_F^2 y^2}\frac{1}{2\pi^2}\;\mathrm{Im}\int d\Omega \frac{d}{d\Omega}\Big(\Omega\coth\frac{\Omega}{2T}\Big)\\ &\times\; \mathrm{tr}\int d^2y \hat{u}M(-\mathbf{y};+)M(y;-)\hat{u}M(-\mathbf{y};-)M(\mathbf{y};+)e^{2i(\Omega+i/\tau)y/v_F}.\end{aligned} \tag{5.22}$$

Here $\hat{u}$ is a 4×4 matrix and $\hat{u}\otimes\hat{u}$ inherits the matrix structure from Eq. 5.12. Namely, it corresponds to the part contained in the square bracket of Eq. 5.12. To further evaluate $\delta\sigma$, one needs to perform angular integration yielding

$$\mathrm{tr}\int d\theta \hat{u}M(-\mathbf{y};+)M(\mathbf{y};-)\hat{u}M(-\mathbf{y};-)M(\mathbf{y};+) = 32\pi\Big(2p\sin^2\varphi(y) + t\Big). \tag{5.23}$$

Here θ is the angular coordinate of $\mathbf{y}$. Parameters are defined as $p' = \gamma_0 - \beta_z - \gamma_z$ and $t' = 2\gamma_z + 2\beta_z + \beta_\perp + \gamma_\perp$. Linearly expanding $\sin\varphi$, one can write $\delta\sigma$ as the following single variable integral

$$\delta\sigma \simeq -\frac{e^2\tau^2 k_F^2}{4\pi^3 v_F^2}\int d\Omega\frac{d}{d\Omega}\Big(\Omega\coth\frac{\Omega}{2T}\Big)\mathrm{Im}\int\frac{dy}{y}\Big(p'\frac{y^2}{2k_F^2 l^4} + t'\Big)e^{2i(\Omega+i\tau)y/v_F}. \tag{5.24}$$

Now we handle the integral over y firstly and define

$$I(B) = \mathrm{Im} \int \frac{dy}{y} \Big(p' \frac{y^2}{2k_F^2 l^4} + t' \Big) e^{2i(\Omega + i\tau)y/v_F}. \tag{5.25}$$

The zero field result is simply given by

$$I(0) \simeq t' \int_{1/k_F}^{\infty} dy \frac{1}{y} \sin \frac{2\Omega y}{v_F} = \frac{\pi t'}{2} + O(\Omega/E_F). \tag{5.26}$$

Note that the scalar part α_0 of impurity potential does not contribute to t, i.e., the zero field conductivity. The field-dependent contribution reads

$$I(B) - I(0) = \frac{p'}{2k_F^2 l^4} \int_{1/k_F}^{v_F/\omega_0} y \sin \frac{2\Omega y}{v_F} e^{-\frac{2y}{v_F \tau}} dy. \tag{5.27}$$

We limit our attention to the limit $\omega_0 \tau \ll 1$ so that $\exp(-(\omega_0 \tau)^{-1}) \simeq 0$. This ensures the convergence of the integral. Also $E_F \tau \gg 1$ is assumed. Then we define $x = 2y/v_F \tau$ and rewrite the integral as

$$I(B) - I(0) \simeq \frac{p'}{8k_F^2 l^4} (v_F \tau)^2 \int_0^{+\infty} x \sin \Big(\Omega \tau x \Big) e^{-x} dx. \tag{5.28}$$

Here the lower cut-off is set as zero and the upper cut-off is set to be infinity, since $1/(E_F \tau) \ll 1$ and $1/(\omega_0 \tau) \gg 1$. Performing the integral, one obtains

$$I(B) - I(0) = p' \frac{(v_F \tau)^2}{8k_F^2 l^4} \frac{2\Omega\tau}{(1 + \Omega^2 \tau^2)^2}. \tag{5.29}$$

Thus, with the help of Eqs. 5.26 and 5.29, one can write the conductivity as a single variable integral

$$\delta\sigma \simeq -\frac{e^2 \tau^2 k_F^2}{4\pi^3 v_F^2} \int d\Omega \frac{d}{d\Omega} \Big(\Omega \coth \frac{\Omega}{2T} \Big) \Big[\frac{\pi t'}{2} + p' \frac{(v_F \tau)^2}{4k_F^2 l^4} \frac{\Omega\tau}{(1 + \Omega^2 \tau^2)^2} \Big]. \tag{5.30}$$

The remaining task is to simply evaluate the integral above. Now we treat the zero-field and field-dependent contributions separately

- Zero-field contribution. At $B = 0$, the integral involved is

$$\int_0^{E_F} d\Omega \frac{d}{d\Omega}\Big(\Omega \coth \frac{\Omega}{2T}\Big) = \Big[E_F \coth(E_F/2T) - 2T\Big]. \tag{5.31}$$

  Here we set the upper bound for Ω to be the Fermi energy, E_F. This integral leads to the well-known linear temperature dependence in the longtudinal conductivity. Since $E_F/T \gg 1$, the temperature dependence in $\coth(E_F/2T)$function is exponentially weak. The main temperature dependence comes from the latter,the linear one $-2T$.

- Field-dependent contribution. The field-dependent contribution is given by the integral

$$\int d\Omega \frac{d}{d\Omega}\Big(\Omega \coth \frac{\Omega}{2T}\Big) \frac{\Omega\tau}{(1+\Omega^2\tau^2)^2} = 2T \int_0^{\infty} dz \frac{d}{dz}\Big(z \coth z\Big) \frac{2z \times T\tau}{(1+4z^2(T\tau)^2)^2}. \tag{5.32}$$

  Here we define the variable $z = \Omega/2T$. Since we consider the ballistic regime, we only need the asymptotic behavior of the integral at $T\tau \gg 1$. We find that Eq. 5.32 has the asymptotic behavior, $\alpha 2T(T\tau)^{-2}$ when $T\tau \gg 1$. Here α is analytically found to be $\alpha = \pi/24$. The functional dependence $\propto (T\tau)^{-2}$ and α are derived below.

  For the integrand in the Eq. 5.32, one can separate the integral domain into two parts. They are $(0, \kappa)$ and (κ, ∞) for variable z with $\kappa \sim 1$. We call each region's contribution to the integral as J_1, J_2 in a sequence. At the first region, $\partial_z(z/\tanh z) \simeq 2z/3$. Then one defines $x = 2zT\tau$ and gets

$$J_1 = 2T\frac{(T\tau)^{-2}}{6} \int_0^{+\infty} dx \frac{x^2}{(1+x^2)^2} = \frac{\pi}{24} 2T(T\tau)^{-2}. \tag{5.33}$$

Here we extend the upper bound of integral $2T\tau$ to ∞, since $T\tau \gg 1$ and we are looking for the leading order. In second region, $\partial_z(z/\tanh z) \simeq 1$. One similarly obtains

$$J_2 \simeq 2T \int_{\kappa}^{\infty} dz (2zT\tau)^{-3} \propto (T\tau)^{-3}. \tag{5.34}$$

From the analysis, one can clearly see that J_1 and J_2 give the leading contributions and the asymptotic behavior of Eq. 5.32 is $\sim (T\tau)^{-2}$.

Now we assume the weak and short-ranged scatterer and identity the expression of τ in the Born-approximation[205],

$$\frac{1}{\tau} = \frac{k_F}{2v_F}(\gamma_0 + 4\beta_\perp + 2\gamma_\perp + 2\beta_z + \gamma_z). \tag{5.35}$$

Thus $\delta\sigma$ can be simplified to be

$$\delta\sigma \simeq \lambda \frac{e^2\tau}{\pi}\Big(\tilde{t}T - \tilde{p}\frac{\omega_0^2}{48T}\Big). \tag{5.36}$$

Here λ is the dimensionless interaction parameter $\lambda = U_0 k_F (2\pi v_F)^{-1}$. Parameters $\tilde{t}$ and $\tilde{p}$ are dimensionless and describe the strength of disorder potential. They are defined by

$$\tilde{t} = \frac{2\gamma_z + 2\beta_z + \beta_\perp + \gamma_\perp}{\gamma_0 + 4\beta_\perp + 2\gamma_\perp + 2\beta_z + \gamma_z}, \quad \tilde{p} = \frac{\gamma_0 - \beta_z - \gamma_z}{\gamma_0 + 4\beta_\perp + 2\gamma_\perp + 2\beta_z + \gamma_z}. \tag{5.37}$$

Eq. 5.36 is the main conclusion in this note. (i) The zero-field contribution linearly depends on the temperature, and this linear dependence is highly sensitive to the nature of the disorder. Once the impurity potential is scalar-like, i.e., only $\alpha_0 \neq 0$ while $\gamma_z = \beta_z = \beta_\perp = \gamma_\perp = 0$, the linear in temperature term vanishes. (ii)

The field-dependent correction is inversely dependent on the temperature. If the impurity potential is scalar-like, the ω_0^2/T gives the leading interaction correction to the conductivity.

5.5 Comparison of the ballistic magnetotransport with the hydrodynamics description

Here, we present a comparison between the mechanism in this chapter and the hydrodynamics, which has been the main focus of studies recently. We also argue that the mechanism in this chapter is the dominating effect when temperature lies in a parametrically large interval.

It is well established that clean many-body quantum systems may exhibit the hydrodynamic limit[31]. To observe hydrodynamics, the many-body system shall have the condition on scales, $l_{ee} \ll L$. Here l_{ee} is the mean free path due to the interaction while L is the one due to disorder/impurity potential. In other words, the length scale from interactions shall be the smallest.

We mainly focus on the effects of interactions on magnetotransport of doped graphene. This implies that the Femi energy is the largest energy scale, $\hbar E_F \tau/k_B \gg 1$, so the quasiparticles are long-lived and weakly interacting. This indicates that l_{ee} is very large. Moreover, even in the ultra-clean sample, One can show that $l_{ee} > L$ in a parametrically large temperature interval. Consider a temperature scale corresponding to ballistic transport given in terms of the impurity scattering time, τ,

$$T_0 = \hbar L/v_F k_B. \tag{5.38}$$

In doped graphene the scattering rate of quasi-particles, $1/\tau_{ee}$, due to the interaction is determined by the Fermi-liquid processes to be [6, 167, 163]

$$\hbar\tau_{ee}^{-1} \sim \frac{k_B^2 T^2}{E_F} \ln \frac{E_F}{T}. \tag{5.39}$$

The condition $l_{ee} \gg L$ is then satisfied at temperstures, T, such that

$$\frac{k_B^2 T^2}{E_F} \ln \frac{E_F}{k_B T} < k_B T_0. \tag{5.40}$$

This condition implies that within the logarithmic accuracy $T \lesssim \left(\frac{k_B}{\hbar\tau}\right) \left[\frac{\hbar E_F \tau}{k_B \ln(\hbar E_F \tau / k_B)}\right]^{1/2}$. The estimate for the temperature can be obtained from Eq. (5.40) more accurately. It yields

$$\frac{\alpha^2}{\alpha_0} \ln(1/\alpha) < 1, \quad \text{with } \alpha = \frac{k_B T}{E_F}, \quad \alpha_0 = \frac{k_B T_0}{E_F} \tag{5.41}$$

Under this condition, the ballistic magnetotramsport reported in the present chapter is dominating over the hydrodynamics mechanism. Note the condition can be applied to any sample, for given disorder-related parameter, α_0, of the sample.

For samples studied in Refs. [215],, one has

$$E_F \simeq 0.4eV, \quad T_0 = \hbar L / v_F k_B \simeq 1.7K \tag{5.42}$$

where E_F is the Fermi energy, v_F is the Fermi velocity and k_B is the Boltzman constant. Given the data, one can evaluate the corresponding $\alpha_0 \simeq 3.6 \times 10^{-4}$. Then the condition (5.42) on the temperature acquires the form

$$f(\alpha) \equiv \alpha^2 \times \ln(1/\alpha) < \alpha_0 \simeq 3.6 \times 10^{-4}. \tag{5.43}$$

Fig. 3.3 depicts the parameter range for temperature under which the condition is satisfied, namely when $\alpha < 8.7 \times 10^{-3}$. This means for samples under consideration $T < 40K$. Thus the main result of the present chapter is dominating for the ultra-clean and doped sample in Eq. 5.42 , when the temperature lies in a parametrically large interval, $1.7K < T < 40K$. Here the lower bound is set by the ballistic regime.

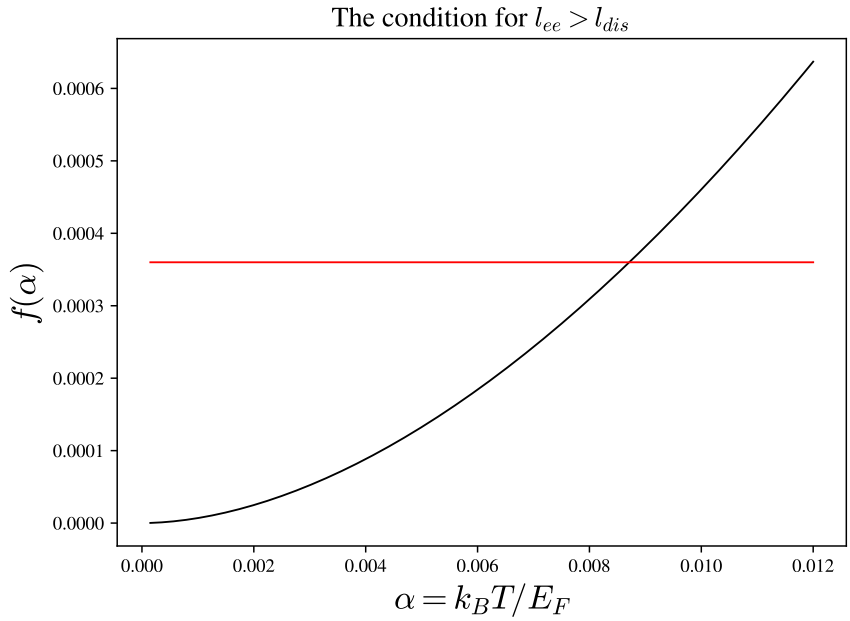

Figure 5.4: (color online) The plot of $f(\alpha)$ defined in Eq. 5.43. The red line locates the value of α_0. The intersection of two curves is around $\alpha \simeq 8.7 \times 10^{-3}$.

5.6 Implications for the experiments.

The new magnetoresistance behavior can be observed in experiments, provided with two conditions on disorder: (1). the disorder in the sample should ensure the inequality, $p/t \gg 1$. (2). The sample should be clean enough so that the ballistic transport can be observed.

To ensure $p/t \gg 1$, the type of disorder in a sample needs to be primarily scalar-like. Namely, only a small portion of disorder potentials create intra-valley scatterings $A \leftrightarrows B$, intervalley scatterings $K \leftrightarrows K'$, and different on-site chemical potentials on sub-lattices.

The ballistic transport sets a lower bound for temperature, $T > T_0 \equiv k_B/\hbar\tau$. Meanwhile, the temperature should be low enough so that the thermal effects and phonon effects do not defeat the quantum effects of electrons. Thus sample should be clean enough for T_0 to represent a low temperature. In the previous *magnetotransport* experiments, samples under consideration were not clean enough for the ballistic

transport to be observed. For example, in Refs. [183] and [184], the mobility of sample is $\mu \sim 2 \times 10^3$ cm/Vs and the transport time is $\tau \sim 100$ fs. The temperature T_0 is $T_0 \sim 500K$. This is a high temperature where thermal, and phonon effects[216, 217, 218, 219, 220, 221] are strong and dominating. Nowadays, a clean sample with highly mobile electrons can be fabricated. According to Ref. [215], the method of chemical vapor deposition on reusable copper can be used to fabricate the graphene device with a high mobility, $\mu \sim 3.5 \times 10^5$ cm/Vs. The subsequent work[187] shows that the electron mobility can be enhanced to be $\mu \sim 3 \times 10^6$ cm/Vs together with the observation of ballistic transport at $1.7K$. These recent techniques may allow one to study the magnetoresistance of the doped graphene in the ballistic regime[222, 223]. In this regard, the predicted phenomenon in this chapter can be observed.

CONCLUSIONS

In the first part of the thesis, we obtained the universal features including finite-size amplitude and entanglement entropy to characterize two novel types of quantum criticalities in one spatial dimension.

We obtained a non-monototic finite-size scaling function around the tricriticality separating topologically ordered, SPT, and trivial phases in Majorana chains. The finite size correction to the ground state energy is a universal function of a new dimensionless scale, $g \sim \sqrt{N}B$, where N is the system size in Chapter 1 of Part I and B is the symmetry-breaking field. We derive the effective low-energy theory corresponding to these models and show the emergence of the scale g that describes the evolution of the low-energy spectrum with B. We analytically calculate the asymptotes of the universal finite-size scaling function, $f(w, g)$. Finally, we show that the scale g emerges in the boundary entropy, which is shown to be universal for three models.

We also found an anomalously large finite-size amplitude at the non-CFT criticality Π, which separates two topologically-distinct CFTs. The universal finite-size amplitude J emerges as the coefficient in front of L^{-2} term in the ground state energy of the system. Here L is the system size in Chapter 2 of Part I. The magnitude of J is anomalously large as it is of the order of one. The entanglement of the ground state is also found to be non-trivial, carrying a non-logarithmic entropy. This originates from the zero modes at the Fermi surface. Compared to CFTs, zero modes play a more crucial role at the criticality Π.

In the second part of the thesis, we systematically studied the effect of a weak magnetic field in the doped graphene. We established the mechanism of chiral symmetry breaking and have found various many-body consequences.

We obtained a new and anomalous form of Friedel oscillations (FO) in graphene induced by a weak magnetic field. The new FO carries the constant magnitude of the oscillation in a parametrically large interval. The origin of this effect is an emerging spin-dependent phase in electron propagators, $\sim \exp(-i\hat{\Sigma}_z\theta(r)/2)$. The emergence of Σ_z in the semi-classical propagator characterizes the chiral symmetry breaking effect.

We found that, for two-dimensional Dirac electrons, the application of a weak magnetic field enhances significantly the many-body effects. This is in contrast to the conventional 2D electron gas. The reason for this is the pseudospin-dependent magnetic correction in Dirac electron propagators, $\sim \hat{\Sigma}_z\theta(r)$. Many-body characteristics including quasi-particle lifetime, quasi-particle velocity and thermodynamics acquire novel field-dependent corrections from the CSB effect.

We also discovered that the pseudospin-dependent phase generates an anomalous interaction correction to the static conductivity in the ballistic regime. The correction implies that the magnetoresistance, $\delta\rho_{xx}$ scales inversely with temperature $\propto 1/T$ in a parametrically large interval. When the disorder is scalarlike, the $\propto 1/T$ behavior is the leading contribution in the crossover between diffusive regime exhibiting weak localization and quantum magnetooscillations.

To conclude, we showed in the present thesis that breaking of conventional symmetries such as the time-reversal symmetry, conformal symmetry, and the chiral symmetry leads to significant physical consequences including universal finite-size scaling and enhanced interaction effects in low-dimensional electronic systems.

BIBLIOGRAPHY

[1] A. Belavin, A. Polyakov, and A. Zamolodchikov, "Infinite conformal symmetry in two-dimensional quantum field theory," *Nuclear Physics B* **241** no. 2, (1984) 333.

[2] H. W. J. Blöte, J. L. Cardy, and M. P. Nightingale, "Conformal invariance, the central charge, and universal finite-size amplitudes at criticality," *Phys. Rev. Lett.* **56** (Feb, 1986) 742.

[3] I. Affleck, "Universal term in the free energy at a critical point and the conformal anomaly," *Phys. Rev. Lett.* **56** (Feb, 1986) 746.

[4] J. M. Luttinger, "An exactly soluble model of a many-fermion system," *Journal of Mathematical Physics* **4** no. 9, (1963) 1154–1162.

[5] A. Imambekov, T. L. Schmidt, and L. I. Glazman, "One-dimensional quantum liquids: Beyond the luttinger liquid paradigm," *Rev. Mod. Phys.* **84** (Sep, 2012) 1253–1306.

[6] G. F. Giuliani and J. J. Quinn, "Lifetime of a quasiparticle in a two-dimensional electron gas," *Phys. Rev. B* **26** (Oct, 1982) 4421–4428.

[7] T. Jungwirth and A. H. MacDonald, "Electron-electron interactions and two-dimensional–two-dimensional tunneling," *Phys. Rev. B* **53** (Mar, 1996) 7403.

[8] L. Zheng and S. Das Sarma, "Coulomb scattering lifetime of a two-dimensional electron gas," *Phys. Rev. B* **53** (Apr, 1996) 9964–9967.

[9] A. V. Chubukov and D. L. Maslov, "Nonanalytic corrections to the fermi-liquid behavior," *Phys. Rev. B* **68** (Oct, 2003) 155113.

[10] J. M. Kosterlitz and D. J. Thouless, "Ordering, metastability and phase transitions in two-dimensional systems," *Journal of Physics C: Solid State Physics* **6** no. 7, (Apr, 1973) 1181–1203.

[11] K. v. Klitzing, G. Dorda, and M. Pepper, "New method for high-accuracy determination of the fine-structure constant based on quantized hall resistance," *Phys. Rev. Lett.* **45** (Aug, 1980) 494–497.

[12] D. J. Thouless, M. Kohmoto, M. P. Nightingale, and M. den Nijs, "Quantized hall conductance in a two-dimensional periodic potential," *Phys. Rev. Lett.* **49** (Aug, 1982) 405–408.

[13] F. D. M. Haldane, "Model for a quantum hall effect without landau levels: Condensed-matter realization of the "parity anomaly"," *Phys. Rev. Lett.* **61** (Oct, 1988) 2015–2018.

[14] A. Y. Kitaev, "Unpaired Majorana fermions in quantum wires," *Physics-Uspekhi* **44** no. 10S, (2001) 131.

[15] X. Chen, Z.-C. Gu, Z.-X. Liu, and X.-G. Wen, "Symmetry protected topological orders and the group cohomology of their symmetry group," *Phys. Rev. B* **87** (Apr, 2013) 155114.

[16] A. M. Turner, F. Pollmann, and E. Berg, "Topological phases of one-dimensional fermions: An entanglement point of view," *Phys. Rev. B* **83** (Feb, 2011) 075102.

[17] L. Fidkowski and A. Kitaev, "Topological phases of fermions in one dimension," *Phys. Rev. B* **83** (Feb, 2011) 075103.

[18] F. Pollmann and A. M. Turner, "Detection of symmetry-protected topological phases in one dimension," *Phys. Rev. B* **86** (Sep, 2012) 125441.

[19] L. Fidkowski and A. Kitaev, "Effects of interactions on the topological classification of free fermion systems," *Phys. Rev. B* **81** (Apr, 2010) 134509.

[20] C. L. Kane and E. J. Mele, "Z_2 topological order and the quantum spin hall effect," *Phys. Rev. Lett.* **95** (Sep, 2005) 146802.

[21] J. Moore, "The next generation," *Nature Physics* **5** no. 6, (2009) 378.

[22] T. Senthil, "Symmetry-protected topological phases of quantum matter," *Annual Review of Condensed Matter Physics* **6** no. 1, (2015) 299.

[23] W. P. Su, J. R. Schrieffer, and A. J. Heeger, "Solitons in polyacetylene," *Phys. Rev. Lett.* **42** (Jun, 1979) 1698.

[24] A. Kitaev, "Periodic table for topological insulators and superconductors," *AIP Conference Proceedings* **1134** no. 1, (2009) 22–30.

[25] J. MILNOR, *Introduction to Algebraic K-Theory. (AM-72)*. Princeton University Press, 1971.

[26] M. Atiyah, R. Bott, and A. Shapiro, "Clifford modules," *Topology* **3** (1964) 3–38.

[27] "Symmetries, dimensions and topological insulators: the mechanism behind the face of the bott clock,".

[28] A. H. Castro Neto, F. Guinea, N. M. R. Peres, K. S. Novoselov, and A. K. Geim, "The electronic properties of graphene," *Rev. Mod. Phys.* **81** (Jan, 2009) 109.

[29] V. N. Kotov, B. Uchoa, V. M. Pereira, F. Guinea, and A. H. Castro Neto, "Electron-electron interactions in graphene: Current status and perspectives," *Rev. Mod. Phys.* **84** (Jul, 2012) 1067.

[30] I. S. Tupitsyn and N. V. Prokof'ev, "Stability of dirac liquids with strong coulomb interaction," *Phys. Rev. Lett.* **118** (Jan, 2017) 026403.

[31] A. Lucas and K. C. Fong, "Hydrodynamics of electrons in graphene," *Journal of Physics: Condensed Matter* **30** no. 5, (Jan, 2018) 053001.

[32] K. Wang and T. A. Sedrakyan, "Universal finite-size scaling around tricriticality between topologically ordered, symmetry-protected topological, and trivial phases," *Phys. Rev. B* **101** (Jan, 2020) 035410.

[33] T. Gulden, M. Janas, Y. Wang, and A. Kamenev, "Universal finite-size scaling around topological quantum phase transitions," *Phys. Rev. Lett.* **116** (Jan, 2016) 026402.

[34] A. Altland and M. R. Zirnbauer, "Nonstandard symmetry classes in mesoscopic normal-superconducting hybrid structures," *Phys. Rev. B* **55** (Jan, 1997) 1142.

[35] A. P. Schnyder, S. Ryu, A. Furusaki, and A. W. W. Ludwig, "Classification of topological insulators and superconductors in three spatial dimensions," *Phys. Rev. B* **78** (Nov, 2008) 195125.

[36] C.-K. Chiu, J. C. Y. Teo, A. P. Schnyder, and S. Ryu, "Classification of topological quantum matter with symmetries," *Rev. Mod. Phys.* **88** (Aug, 2016) 035005.

[37] M. Greiter, V. Schnells, and R. Thomale, "The 1D ising model and the topological phase of the kitaev chain," *Annals of Physics* **351** (Dec, 2014) 1026.

[38] E. Lieb, T. Schultz, and D. Mattis, "Two soluble models of an antiferromagnetic chain," *Annals of Physics* **16** no. 3, (1961) 407.

[39] S. D. Sarma, M. Freedman, and C. Nayak, "Majorana zero modes and topological quantum computation," *Npj Quantum Information* **1** (Oct, 2015) 15001. Review Article.

[40] R. M. Lutchyn, J. D. Sau, and S. Das Sarma, "Majorana fermions and a topological phase transition in semiconductor-superconductor heterostructures," *Phys. Rev. Lett.* **105** (Aug, 2010) 077001.

[41] R. Wakatsuki, M. Ezawa, and N. Nagaosa, "Majorana fermions and multiple topological phase transition in Kitaev ladder topological superconductors," *Phys. Rev. B* **89** (May, 2014) 174514.

[42] H. Wang, L. Shao, Y. Pan, R. Shen, L. Sheng, and D. Xing, "Flux-driven quantum phase transitions in two-leg Kitaev ladder topological superconductor systems," *Physics Letters A* **380** no. 46, (2016) 3936.

[43] J. Alicea, "New directions in the pursuit of Majorana fermions in solid state systems," *Reports on Progress in Physics* **75** no. 7, (Jun, 2012) 076501.

[44] M. Leijnse and K. Flensberg, "Introduction to topological superconductivity and Majorana fermions," *Semiconductor Science and Technology* **27** no. 12, (Nov, 2012) 124003.

[45] C. Beenakker, "Search for Majorana fermions in superconductors," *Annual Review of Condensed Matter Physics* **4** no. 1, (2013) 113.

[46] P. Di Francesco, P. Mathieu, and D. Senechal, *Conformal Field Theory*. Graduate Texts in Contemporary Physics. Springer-Verlag, New York, 1997.

[47] I. Affleck and A. W. W. Ludwig, "Universal noninteger "ground-state degeneracy" in critical quantum systems," *Phys. Rev. Lett.* **67** (Jul, 1991) 161.

[48] N. G. J. Ruben Verresen, Ryan Thorngren and F. Pollmann, "Gapless topological phases and symmetry-enriched quantum criticality,".

[49] D. E. Parker, T. Scaffidi, and R. Vasseur, "Topological Luttinger liquids from decorated domain walls," *Phys. Rev. B* **97** (Apr, 2018) 165114.

[50] T. T. Wu, B. M. McCoy, C. A. Tracy, and E. Barouch, "Spin-spin correlation functions for the two-dimensional ising model: Exact theory in the scaling region," *Phys. Rev. B* **13** (Jan, 1976) 316.

[51] E. Cornfeld and E. Sela, "Entanglement entropy and boundary renormalization group flow: Exact results in the Ising universality class," *Phys. Rev. B* **96** (Aug, 2017) 075153.

[52] V. J. Emery and S. Kivelson, "Mapping of the two-channel Kondo problem to a resonant-level model," *Phys. Rev. B* **46** (Nov, 1992) 10812.

[53] J. L. Cardy, "Boundary conditions, fusion rules and the Verlinde formula," *Nuclear Physics B* **324** no. 3, (1989) 581.

[54] J. L. Cardy and D. C. Lewellen, "Bulk and boundary operators in conformal field theory," *Physics Letters B* **259** no. 3, (1991) 274.

[55] P. Calabrese and J. Cardy, "Entanglement entropy and conformal field theory," *Journal of Physics A: Mathematical and Theoretical* **42** no. 50, (Dec, 2009) 504005.

[56] I. Affleck, N. Laflorencie, and E. S. Sørensen, "Entanglement entropy in quantum impurity systems and systems with boundaries," *Journal of Physics A: Mathematical and Theoretical* **42** no. 50, (Dec, 2009) 504009.

[57] H.-Q. Zhou, T. Barthel, J. O. Fjærestad, and U. Schollwöck, "Entanglement and boundary critical phenomena," *Phys. Rev. A* **74** (Nov, 2006) 050305.

[58] T. Sedrakyan, "Staggered anisotropy parameter modification of the anisotropic $t - J$ model," *Nuclear Physics B* **608** no. 3, (2001) 557.

[59] V. V. Mkhitaryan and T. A. Sedrakyan, "Mean-Field theory for Heisenberg zigzag ladder: Ground state energy and Spontaneous Symmetry Breaking," *Annales Henri Poincaré* **7** no. 7, (Dec, 2006) 1579.

[60] H. Katsura, D. Schuricht, and M. Takahashi, "Exact ground states and topological order in interacting Kitaev/Majorana chains," *Phys. Rev. B* **92** (Sep, 2015) 115137.

[61] N. Lang and H. P. Büchler, "Topological states in a microscopic model of interacting fermions," *Phys. Rev. B* **92** (Jul, 2015) 041118.

[62] L. Herviou, C. Mora, and K. Le Hur, "Phase diagram and entanglement of two interacting topological Kitaev chains," *Phys. Rev. B* **93** (Apr, 2016) 165142.

[63] F. Iemini, L. Mazza, D. Rossini, R. Fazio, and S. Diehl, "Localized Majorana-like modes in a number-conserving setting: An exactly solvable model," *Phys. Rev. Lett.* **115** (Oct, 2015) 156402.

[64] K. Wang and T. A. Sedrakyan, "Universal finite-size amplitude and anomalous entangment entropy of $z = 2$ quantum Lifshitz criticalities in topological chains," *SciPost Phys.* **12** (2022) 134.

[65] H. Casini and M. Huerta, "Entanglement entropy in free quantum field theory," *Journal of Physics A: Mathematical and Theoretical* **42** no. 50, (Dec, 2009) 504007.

[66] A. Kitaev, "Periodic table for topological insulators and superconductors," *AIP Conference Proceedings* **1134** no. 1, (2009) 22.

[67] R. Verresen, R. Thorngren, N. G. Jones, and F. Pollmann, "Gapless topological phases and symmetry-enriched quantum criticality," 2019.

[68] W. Ji, S. Shao, and X. Wen, "Topological transition on the conformal manifold," *Phys. Rev. Research* **2** (Aug, 2020) 033317.

[69] M. Cheng and D. J. Williamson, "Relative anomaly in $(1 + 1)$d rational conformal field theory," *Phys. Rev. Research* **2** (Oct, 2020) 043044.

[70] T. Scaffidi, D. E. Parker, and R. Vasseur, "Gapless symmetry-protected topological order," *Phys. Rev. X* **7** (Nov, 2017) 041048.

[71] R. Verresen, N. G. Jones, and F. Pollmann, "Topology and edge modes in quantum critical chains," *Phys. Rev. Lett.* **120** (Jan, 2018) 057001.

[72] R. M. Hornreich, "The lifshitz point: Phase diagrams and critical behavior," *Journal of Magnetism and Magnetic Materials* **15-18** (1980) 387.

[73] V. Popkov and M. Salerno, "Logarithmic divergence of the block entanglement entropy for the ferromagnetic heisenberg model," *Phys. Rev. A* **71** (Jan, 2005) 012301.

[74] P. Hořava, "Quantum gravity at a lifshitz point," *Phys. Rev. D* **79** (Apr, 2009) 084008.

[75] B. Chen and Q. Huang, "Field theory at a lifshitz point," *Physics Letters B* **683** no. 2, (2010) 108–113.

[76] N. Chepiga and F. Mila, "Lifshitz point at commensurate melting of chains of rydberg atoms," *Phys. Rev. Research* **3** (Apr, 2021) 023049.

[77] R. R. Kumar, Y. R. Kartik, S. Rahul, and S. Sarkar, "Multi-critical topological transition at quantum criticality," *Scientific Reports* **11** no. 1, (Jan, 2021) 1004.

[78] C. Boudreault, C. Berthiere, and W. Witczak-Krempa, "Entanglement and correlations in $z = 2$ lifshitz theories under wavefunction renormalization group flow," 2021.

[79] L. Li, Z. Xu, and S. Chen, "Topological phases of generalized su-schrieffer-heeger models," *Phys. Rev. B* **89** (Feb, 2014) 085111.

[80] K. Leung, "Finite-size scaling at critical points with spatial anisotropies," *International Journal of Modern Physics C* **03** no. 02, (1992) 367.

[81] A. Hucht, "On the symmetry of universal finite-size scaling functions in anisotropic systems," *Journal of Physics A: Mathematical and General* **35** no. 31, (Jul, 2002) L481.

[82] N. S. Tonchev, "Finite-size scaling in anisotropic systems," *Phys. Rev. E* **75** (Mar, 2007) 031110.

[83] Y. Wang, H. Zhang, and A. Kamenev, "Finite-size scaling at a topological transition: Bilinear-biquadratic spin-1 chain," *Phys. Rev. B* **101** (Jun, 2020) 235145.

[84] L. M. Veríssimo, M. S. S. Pereira, and M. L. Lyra, "Tangential finite-size scaling at the gaussian topological transition in the quantum spin-1 anisotropic chain," *Phys. Rev. B* **104** (Jul, 2021) 024409.

[85] P. Calabrese and A. Lefevre, "Entanglement spectrum in one-dimensional systems," *Phys. Rev. A* **78** (Sep, 2008) 032329.

[86] F. Pollmann, A. M. Turner, E. Berg, and M. Oshikawa, "Entanglement spectrum of a topological phase in one dimension," *Phys. Rev. B* **81** (Feb, 2010) 064439.

[87] B. Swingle and T. Senthil, "Universal crossovers between entanglement entropy and thermal entropy," *Phys. Rev. B* **87** (Jan, 2013) 045123.

[88] M.-C. Chung and I. Peschel, "Density-matrix spectra of solvable fermionic systems," *Phys. Rev. B* **64** (Jul, 2001) 064412.

[89] I. Peschel, "Calculation of reduced density matrices from correlation functions," *Journal of Physics A: Mathematical and General* **36** no. 14, (Mar, 2003) L205–L208.

[90] H. Huffel and G. Kelnhofer, "Field space entanglement entropy, zero modes and lifshitz models," *Physics Letters B* **775** (2017) 229.

[91] S. M. Chandran and S. Shankaranarayanan, "Divergence of entanglement entropy in quantum systems: Zero-modes," *Phys. Rev. D* **99** (Feb, 2019) 045010.

[92] E. Tjoa and E. Martín-Martínez, "Vacuum entanglement harvesting with a zero mode," *Phys. Rev. D* **101** (Jun, 2020) 125020.

[93] Y. Wang, T. Gulden, and A. Kamenev, "Finite-size scaling of entanglement entropy in one-dimensional topological models," *Phys. Rev. B* **95** (Feb, 2017) 075401.

[94] K. Wang, M. E. Raikh, and T. A. Sedrakyan, "Persistent friedel oscillations in graphene due to a weak magnetic field," *Phys. Rev. B* **103** (Feb, 2021) 085418.

[95] K. S. Novoselov, A. K. Geim, S. V. Morozov, D. Jiang, Y. Zhang, S. V. Dubonos, I. V. Grigorieva, and A. A. Firsov, "Electric field effect in atomically thin carbon films," *Science* **306** no. 5696, (2004) 666.

[96] K. S. Novoselov, A. K. Geim, S. V. Morozov, D. Jiang, M. I. Katsnelson, I. V. Grigorieva, S. V. Dubonos, and A. A. Firsov, "Two-dimensional gas of massless Dirac fermions in graphene," *Nature* **438** no. 7065, (Nov, 2005) 197.

[97] P. Z. Sun, Q. Yang, W. J. Kuang, Y. V. Stebunov, W. Q. Xiong, J. Yu, R. R. Nair, M. I. Katsnelson, S. J. Yuan, I. V. Grigorieva, M. Lozada-Hidalgo, F. C. Wang, and A. K. Geim, "Limits on gas impermeability of graphene," *Nature* **579** no. 7798, (Mar, 2020) 229.

[98] Y. Zhang, Y.-W. Tan, H. L. Stormer, and P. Kim, "Experimental observation of the quantum Hall effect and Berry's phase in graphene," *Nature* **438** no. 7065, (Nov, 2005) 201.

[99] V. P. Gusynin and S. G. Sharapov, "Unconventional Integer Quantum Hall effect in graphene," *Phys. Rev. Lett.* **95** (Sep, 2005) 146801.

[100] B. Wunsch, T. Stauber, F. Sols, and F. Guinea, "Dynamical polarization of graphene at finite doping," *New J. of Phys.* **8** no. 12, (Dec, 2006) 318.

[101] A. Altland, "Low-energy theory of disordered graphene," *Phys. Rev. Lett.* **97** (Dec, 2006) 236802.

[102] V. V. Cheianov and V. I. Fal'ko, "Friedel Oscillations, impurity scattering, and temperature dependence of resistivity in graphene," *Phys. Rev. Lett.* **97** (Nov, 2006) 226801.

[103] I. L. Aleiner and K. B. Efetov, "Effect of disorder on transport in graphene," *Phys. Rev. Lett.* **97** (Dec, 2006) 236801.

[104] J. Tworzydło, B. Trauzettel, M. Titov, A. Rycerz, and C. W. J. Beenakker, "Sub-poissonian shot noise in graphene," *Phys. Rev. Lett.* **96** (Jun, 2006) 246802.

[105] A. Rycerz, J. Tworzydło, and C. W. J. Beenakker, "Valley filter and valley valve in graphene," *Nature Physics* **3** no. 3, (Mar, 2007) 172.

[106] C. W. J. Beenakker, "Colloquium: Andreev reflection and klein tunneling in graphene," *Rev. Mod. Phys.* **80** (Oct, 2008) 1337.

[107] Y.-W. Tan, Y. Zhang, K. Bolotin, Y. Zhao, S. Adam, E. H. Hwang, S. Das Sarma, H. L. Stormer, and P. Kim, "Measurement of scattering rate and minimum conductivity in graphene," *Phys. Rev. Lett.* **99** (Dec, 2007) 246803.

[108] E. Mariani, L. I. Glazman, A. Kamenev, and F. von Oppen, "Zero-bias anomaly in the tunneling density of states of graphene," *Phys. Rev. B* **76** (Oct, 2007) 165402.

[109] W.-K. Tse, B. Y.-K. Hu, and S. Das Sarma, "Chirality-induced dynamic Kohn Anomalies in graphene," *Phys. Rev. Lett.* **101** (Aug, 2008) 066401.

[110] C. Bena, "Effect of a single localized impurity on the local density of states in monolayer and bilayer graphene," *Phys. Rev. Lett.* **100** (Feb, 2008) 076601.

[111] C. Bena, "Green's functions and impurity scattering in graphene," *Phys. Rev. B* **79** (Mar, 2009) 125427.

[112] K. I. Bolotin, F. Ghahari, M. D. Shulman, H. L. Stormer, and P. Kim, "Observation of the fractional quantum Hall effect in graphene," *Nature* **462** no. 7270, (Nov, 2009) 196.

[113] C. Bena, "Local density of states in the presence of impurity scattering in graphene at high magnetic field," *Phys. Rev. B* **81** (Jan, 2010) 045409.

[114] M. A. H. Vozmediano, M. I. Katsnelson, and F. Guinea, "Gauge fields in graphene," *Phys. Rep.* **496** no. 4, (2010) 109.

[115] A. Bácsi and A. Virosztek, "Local density of states and Friedel oscillations in graphene," *Phys. Rev. B* **82** (Nov, 2010) 193405.

[116] G. Gómez-Santos and T. Stauber, "Measurable lattice effects on the charge and magnetic response in graphene," *Phys. Rev. Lett.* **106** (Jan, 2011) 045504.

[117] M. O. Goerbig, "Electronic properties of graphene in a strong magnetic field," *Rev. Mod. Phys.* **83** (Nov, 2011) 1193.

[118] J. Y. Vaishnav, J. Q. Anderson, and J. D. Walls, "Intravalley multiple scattering of quasiparticles in graphene," *Phys. Rev. B* **83** (Apr, 2011) 165437.

[119] S. Das Sarma, S. Adam, E. H. Hwang, and E. Rossi, "Electronic transport in two-dimensional graphene," *Rev. Mod. Phys.* **83** (May, 2011) 407.

[120] G. W. Semenoff, "Chiral symmetry breaking in graphene," *Phys. Scr.* **T146** (Jan, 2012) 014016.

[121] R. Nandkishore, L. S. Levitov, and A. V. Chubukov, "Chiral superconductivity from repulsive interactions in doped graphene," *Nature Physics* **8** no. 2, (Feb, 2012) 158.

[122] C. Dutreix, L. Bilteanu, A. Jagannathan, and C. Bena, "Friedel oscillations at the Dirac cone merging point in anisotropic graphene and graphenelike materials," *Phys. Rev. B* **87** (Jun, 2013) 245413.

[123] J. A. Lawlor, S. R. Power, and M. S. Ferreira, "Friedel oscillations in graphene: Sublattice asymmetry in doping," *Phys. Rev. B* **88** (Nov, 2013) 205416.

[124] B. Amorim, A. Cortijo, F. de Juan, A. G. Grushin, F. Guinea, A. Gutiérrez-Rubio, H. Ochoa, V. Parente, R. Roldán, P. San-Jose, J. Schiefele, M. Sturla, and M. A. H. Vozmediano, "Novel effects of strains in graphene and other two dimensional materials," *Phys. Rep.* **617** (2016) 1.

[125] T. M. Rusin and W. Zawadzki, "Theory of Friedel oscillations in monolayer graphene and group-vi dichalcogenides in a magnetic field," *Phys. Rev. B* **97** (May, 2018) 205410.

[126] C. Dutreix, H. González-Herrero, I. Brihuega, M. I. Katsnelson, C. Chapelier, and V. T. Renard, "Measuring the Berry phase of graphene from wavefront dislocations in Friedel oscillations," *Nature* **574** no. 7777, (Oct, 2019) 219.

[127] M. Agarwal and E. G. Mishchenko, "Dynamic response functions of two-dimensional Dirac fermions with screened coulomb and short-range interactions," *Phys. Rev. B* **102** (Sep, 2020) 125421.

[128] A. Sedrakyan, A. Sinner, and K. Ziegler, "Deformation of graphene sheet: Interaction of fermions with phonons,".

[129] S. Maiti and T. A. Sedrakyan, "Composite fermion state of graphene as a Haldane-Chern insulator," *Phys. Rev. B* **100** (Sep, 2019) 125428.

[130] A. M. Rudin, I. L. Aleiner, and L. I. Glazman, "Tunneling zero-bias anomaly in the quasiballistic regime," *Phys. Rev. B* **55** (Apr, 1997) 9322.

[131] J. Friedel *Phil. Mag.* **43** (1952) 153.

[132] G.-H. Chen and M. E. Raikh, "Small-q anomaly in the dielectric function and high-temperature oscillations of the screening potential in a two-dimensional electron gas with spin-orbit coupling," *Phys. Rev. B* **59** (Feb, 1999) 5090.

[133] C. Bena, "Friedel oscillations: Decoding the hidden physics," *Comptes Rendus Physique* **17** no. 3, (2016) 302.

[134] T. A. Sedrakyan, E. G. Mishchenko, and M. E. Raikh, "Smearing of the two-dimensional Kohn Anomaly in a nonquantizing magnetic field: Implications for interaction effects," *Phys. Rev. Lett.* **99** (Jul, 2007) 036401.

[135] K. Wang, M. E. Raikh, and T. A. Sedrakyan *Unpublished* .

[136] J. González and J. Herrero, "Graphene wormholes: A condensed matter illustration of Dirac fermions in curved space," *Nucl. Phys. B* **825** no. 3, (2010) 426.

[137] S. Capozziello, R. Pincak, and E. Bartoš, "Chern-Simons current of left and right chiral superspace in graphene wormhole," *Symmetry* **12** (05, 2020) 774.

[138] G. Q. Garcia, P. J. Porfírio, D. C. Moreira, and C. Furtado, "Graphene wormhole trapped by external magnetic field," *Nucl. Phys. B* **950** (2020) 114853.

[139] T. Wehling, A. Black-Schaffer, and A. Balatsky, "Dirac materials," *Adv. Phys.* **63** no. 1, (2014) 1.

[140] D. Yue, L. I. Glazman, and K. A. Matveev, "Conduction of a weakly interacting one-dimensional electron gas through a single barrier," *Phys. Rev. B* **49** (Jan, 1994) 1966.

[141] G. Zala, B. N. Narozhny, and I. L. Aleiner, "Interaction corrections at intermediate temperatures: Longitudinal conductivity and kinetic equation," *Phys. Rev. B* **64** (Nov, 2001) 214204.

[142] Y. Adamov, I. V. Gornyi, and A. D. Mirlin, "Interaction effects on magneto-oscillations in a two-dimensional electron gas," *Phys. Rev. B* **73** (Jan, 2006) 045426.

[143] H. Bateman, A. Erdélyi, W. Magnus, F. Oberhettinger, and F. G. Tricomi, *Higher Transcendental Functions*. McGraw-Hill Book Company, 1953.

[144] E. McCann, K. Kechedzhi, V. I. Fal'ko, H. Suzuura, T. Ando, and B. L. Altshuler, "Weak-localization magnetoresistance and valley symmetry in graphene," *Phys. Rev. Lett.* **97** (Oct, 2006) 146805.

[145] T. A. Sedrakyan and M. E. Raikh, "Interaction effects in a two-dimensional electron gas in a random magnetic field: Implications for composite fermions and the quantum critical point," *Phys. Rev. B* **77** (Mar, 2008) 115353.

[146] T. A. Sedrakyan and M. E. Raikh, "Crossover from Weak Localization to Shubnikov–de Haas oscillations in a high-mobility 2D electron gas," *Phys. Rev. Lett.* **100** (Mar, 2008) 106806.

[147] T. A. Sedrakyan and M. E. Raikh, "Magneto-oscillations due to electron-electron interactions in the ac conductivity of a two-dimensional electron gas," *Phys. Rev. Lett.* **100** (Feb, 2008) 086808.

[148] P. T. Sprunger, L. Petersen, E. W. Plummer, E. Lægsgaard, and F. Besenbacher, "Giant Friedel Oscillations on the Beryllium(0001) Surface," *Science* **275** no. 5307, (1997) 1764.

[149] P. Stano, J. Klinovaja, A. Yacoby, and D. Loss, "Local spin susceptibilities of low-dimensional electron systems," *Phys. Rev. B* **88** (Jul, 2013) 045441.

[150] K. Wang, M. E. Raikh, and T. A. Sedrakyan, "Interaction effects in graphene in a weak magnetic field," *Phys. Rev. B* **104** (Oct, 2021) L161102.

[151] G. W. Semenoff, "Condensed-matter simulation of a three-dimensional anomaly," *Phys. Rev. Lett.* **53** (Dec, 1984) 2449.

[152] M. I. Katsnelson, K. S. Novoselov, and A. K. Geim, "Chiral tunnelling and the klein paradox in graphene," *Nature Physics* **2** no. 9, (Sep, 2006) 620.

[153] J. Pack, B. J. Russell, Y. Kapoor, J. Balgley, J. Ahlers, T. Taniguchi, K. Watanabe, and E. A. Henriksen, "Broken symmetries and Kohn's theorem in graphene cyclotron resonance," *Phys. Rev. X* **10** (Oct, 2020) 041006.

[154] V. Leeb, K. Polyudov, S. Mashhadi, S. Biswas, R. Valentí, M. Burghard, and J. Knolle, "Anomalous quantum oscillations in a heterostructure of graphene on a proximate quantum spin liquid," *Phys. Rev. Lett.* **126** (Mar, 2021) 097201.

[155] B. Sbierski, E. J. Dresselhaus, J. E. Moore, and I. A. Gruzberg, "Criticality of two-dimensional disordered Dirac fermions in the unitary class and universality of the integer quantum hall transition," *Phys. Rev. Lett.* **126** (Feb, 2021) 076801.

[156] L. Guo, Y. Yan, R. Xu, J. Li, and C. Zeng, "Zero-bias conductance peaks effectively tuned by gating-controlled Rashba spin-orbit coupling," *Phys. Rev. Lett.* **126** (Feb, 2021) 057701.

[157] J. Bouaziz, H. Ishida, S. Lounis, and S. Blügel, "Transverse transport in two-dimensional relativistic systems with nontrivial spin textures," *Phys. Rev. Lett.* **126** (Apr, 2021) 147203.

[158] H. Rostami and E. Cappelluti, "Many-body effects in third harmonic generation of graphene," *Phys. Rev. B* **103** (Mar, 2021) 125415.

[159] B. N. Narozhny, I. V. Gornyi, and M. Titov, "Hydrodynamic collective modes in graphene," *Phys. Rev. B* **103** (Mar, 2021) 115402.

[160] G. Zala, B. N. Narozhny, and I. L. Aleiner, "Interaction corrections at intermediate temperatures: Magnetoresistance in a parallel field," *Phys. Rev. B* **65** (Dec, 2001) 020201.

[161] G. Zala, B. N. Narozhny, and I. L. Aleiner, "Interaction corrections at intermediate temperatures: Longitudinal conductivity and kinetic equation," *Phys. Rev. B* **64** (Nov, 2001) 214204.

[162] G. Zala, B. N. Narozhny, and I. L. Aleiner, "Interaction corrections to the hall coefficient at intermediate temperatures," *Phys. Rev. B* **64** (Nov, 2001) 201201.

[163] K. Nomura and A. H. MacDonald, "Quantum transport of massless dirac fermions," *Phys. Rev. Lett.* **98** (Feb, 2007) 076602.

[164] E. Mariani, L. I. Glazman, A. Kamenev, and F. von Oppen, "Zero-bias anomaly in the tunneling density of states of graphene," *Phys. Rev. B* **76** (Oct, 2007) 165402.

[165] S. Misawa, "Temperature-squared term in the heat capacity of a two-dimensional fermi liquid," *Journal of the Physical Society of Japan* **68** no. 7, (1999) 2172.

[166] D. Coffey and K. S. Bedell, "Nonanalytic contributions to the self-energy and the thermodynamics of two-dimensional fermi liquids," *Phys. Rev. Lett.* **71** (Aug, 1993) 1043.

[167] S. Das Sarma, E. H. Hwang, and W. K. Tse, "Many-body interaction effects in doped and undoped graphene: Fermi liquid versus non-fermi liquid," *Phys. Rev. B* **75** (Mar, 2007) 121406.

[168] T. A. Sedrakyan and M. E. Raikh, "Magneto-oscillations due to electron-electron interactions in the ac conductivity of a two-dimensional electron gas," *Phys. Rev. Lett.* **100** (Feb, 2008) 086808.

[169] S. Marchini, S. Günther, and J. Wintterlin, "Scanning tunneling microscopy of graphene on ru(0001)," *Phys. Rev. B* **76** (Aug, 2007) 075429.

[170] G. H. Li, A. Luican, and E. Y. Andrei, "Scanning tunneling spectroscopy of graphene on graphite," *Phys. Rev. Lett.* **102** (Apr, 2009) 176804.

[171] B. Lv, T. Qian, and H. Ding, "Angle-resolved photoemission spectroscopy and its application to topological materials," *Nature Reviews Physics* **1** no. 10, (Oct, 2019) 609.

[172] M. Mucha-Kruczyński, O. Tsyplyatyev, A. Grishin, E. McCann, V. I. Fal'ko, A. Bostwick, and E. Rotenberg, "Characterization of graphene through anisotropy of constant-energy maps in angle-resolved photoemission," *Phys. Rev. B* **77** (May, 2008) 195403.

[173] Q. Li, K. Xia, J. Zhang, Y. Zhang, Q. Li, K. Takahashi, and X. Zhang, "Measurement of specific heat and thermal conductivity of supported and suspended graphene by a comprehensive raman optothermal method," *Nanoscale* **9** (2017) 10784.

[174] A. Sedrakyan, A. Sinner, and K. Ziegler, "Deformation of a graphene sheet: Interaction of fermions with phonons," *Phys. Rev. B* **103** (May, 2021) L201104.

[175] C. Faugeras, P. Kossacki, D. M. Basko, M. Amado, M. Sprinkle, C. Berger, W. A. de Heer, and M. Potemski, "Effect of a magnetic field on the two-phonon Raman scattering in graphene," *Phys. Rev. B* **81** (Apr, 2010) 155436.

[176] M. Kharitonov, "Phase diagram for the $\nu = 0$ quantum hall state in monolayer graphene," *Phys. Rev. B* **85** (Apr, 2012) 155439.

[177] S. Hikami, A. I. Larkin, and Y. Nagaoka, "Spin-Orbit Interaction and Magnetoresistance in the Two Dimensional Random System," *Progress of Theoretical Physics* **63** no. 2, (02, 1980) 707.

[178] B. L. Altshuler, D. Khmel'nitzkii, A. I. Larkin, and P. A. Lee, "Magnetoresistance and hall effect in a disordered two-dimensional electron gas," *Phys. Rev. B* **22** (Dec, 1980) 5142.

[179] M. Dyakonov, "Magnetoconductance due to weak localization beyond the diffusion approximation: The high-field limit," *Solid State Communications* **92** no. 8, (1994) 711.

[180] A. Cassam-Chenai and B. Shapiro, "Two dimensional weak localization beyond the diffusion approximation," *J. Phys. I France* **4** no. 10, (1994) 1527.

[181] T. A. Sedrakyan and M. E. Raikh, "Crossover from weak localization to shubnikov–de haas oscillations in a high-mobility 2d electron gas," *Phys. Rev. Lett.* **100** (Mar, 2008) 106806.

[182] A. A. Kozikov, A. K. Savchenko, B. N. Narozhny, and A. V. Shytov, "Electron-electron interactions in the conductivity of graphene," *Phys. Rev. B* **82** (Aug, 2010) 075424.

[183] B. Jouault, B. Jabakhanji, N. Camara, W. Desrat, C. Consejo, and J. Camassel, "Interplay between interferences and electron-electron interactions in epitaxial graphene," *Phys. Rev. B* **83** (May, 2011) 195417.

[184] J. Jobst, D. Waldmann, I. V. Gornyi, A. D. Mirlin, and H. B. Weber, "Electron-electron interaction in the magnetoresistance of graphene," *Phys. Rev. Lett.* **108** (Mar, 2012) 106601.

[185] B. Jabakhanji, D. Kazazis, W. Desrat, A. Michon, M. Portail, and B. Jouault, "Magnetoresistance of disordered graphene: From low to high temperatures," *Phys. Rev. B* **90** (Jul, 2014) 035423.

[186] K. Gopinadhan, Y. J. Shin, R. Jalil, T. Venkatesan, A. K. Geim, A. H. C. Neto, and H. Yang, "Extremely large magnetoresistance in few-layer graphene/boron–nitride heterostructures," *Nature Communications* **6** no. 1, (Sep, 2015) 8337.

[187] L. Banszerus, M. Schmitz, S. Engels, M. Goldsche, K. Watanabe, T. Taniguchi, B. Beschoten, and C. Stampfer, "Ballistic transport exceeding 28 μm in cvd grown graphene," *Nano Letters* **16** no. 2, (Feb, 2016) 1387–1391.

[188] A. Gold and V. T. Dolgopolov, "Temperature dependence of the conductivity for the two-dimensional electron gas: Analytical results for low temperatures," *Phys. Rev. B* **33** (Jan, 1986) 1076.

[189] G. Zala, B. N. Narozhny, and I. L. Aleiner, "Interaction corrections at intermediate temperatures: Longitudinal conductivity and kinetic equation," *Phys. Rev. B* **64** (Nov, 2001) 214204.

[190] Y. W. Tan, Y. Zhang, H. L. Stormer, and P. Kim, "Temperature dependent electron transport in graphene," *The European Physical Journal Special Topics* **148** no. 1, (Sep, 2007) 15.

[191] K. I. Bolotin, K. J. Sikes, Z. Jiang, M. Klima, G. Fudenberg, J. Hone, P. Kim, and H. L. Stormer, "Ultrahigh electron mobility in suspended graphene," *Solid State Communications* **146** no. 9, (2008) 351.

[192] K. Nomura and A. H. MacDonald, "Quantum transport of massless dirac fermions," *Phys. Rev. Lett.* **98** (Feb, 2007) 076602.

[193] K. I. Bolotin, K. J. Sikes, J. Hone, H. L. Stormer, and P. Kim, "Temperature-dependent transport in suspended graphene," *Phys. Rev. Lett.* **101** (Aug, 2008) 096802.

[194] S. Maiti and T. A. Sedrakyan, "Composite fermion state of graphene as a haldane-chern insulator," *Phys. Rev. B* **100** (Sep, 2019) 125428.

[195] C. Dutreix, H. González-Herrero, I. Brihuega, M. I. Katsnelson, C. Chapelier, and V. T. Renard, "Measuring the berry phase of graphene from wavefront dislocations in friedel oscillations," *Nature* **574** no. 7777, (2019) 219–222.

[196] D. Pan, H. Xu, and F. J. García de Abajo, "Anomalous thermodiffusion of electrons in graphene," *Phys. Rev. Lett.* **125** (Oct, 2020) 176802.

[197] G. Wagner, D. X. Nguyen, and S. H. Simon, "Transport properties of multilayer graphene," *Phys. Rev. B* **101** (Jun, 2020) 245438.

[198] S. A. Mikhailov, "Nonperturbative quasiclassical theory of graphene photoconductivity," *Phys. Rev. B* **103** (Jun, 2021) 245406.

[199] T. Zhu, M. Antezza, and J. S. Wang, "Dynamical polarizability of graphene with spatial dispersion," *Phys. Rev. B* **103** (Mar, 2021) 125421.

[200] M. Kamada, V. Gall, J. Sarkar, M. Kumar, A. Laitinen, I. Gornyi, and P. Hakonen, "Strong magnetoresistance in a graphene corbino disk at low magnetic fields," *Phys. Rev. B* Sep115432.

[201] B. Real, O. Jamadi, M. Milićević, N. Pernet, P. St-Jean, T. Ozawa, G. Montambaux, I. Sagnes, A. Lemaître, L. Le Gratiet, A. Harouri, S. Ravets, J. Bloch, and A. Amo, "Semi-dirac transport and anisotropic localization in polariton honeycomb lattices," *Phys. Rev. Lett.* **125** (Oct, 2020) 186601.

[202] P. Sharma, A. Principi, and D. L. Maslov, "Optical conductivity of a dirac-fermi liquid," *Phys. Rev. B* **104** (Jul, 2021) 045142.

[203] C. Faugeras, P. Kossacki, D. M. Basko, M. Amado, M. Sprinkle, C. Berger, W. A. de Heer, and M. Potemski, "Effect of a magnetic field on the two-phonon raman scattering in graphene," *Phys. Rev. B* **81** (Apr, 2010) 155436.

[204] G. D. Mahan, *Many-Particle Physics*. Springer US, Boston, 2000.

[205] P. M. Ostrovsky, I. V. Gornyi, and A. D. Mirlin, "Electron transport in disordered graphene," *Phys. Rev. B* **74** (Dec, 2006) 235443.

[206] T. A. Sedrakyan and M. E. Raikh, "Interaction effects in a two-dimensional electron gas in a random magnetic field: Implications for composite fermions and the quantum critical point," *Phys. Rev. B* **77** (Mar, 2008) 115353.

[207] G. Y. Vasileva, D. Smirnov, Y. L. Ivanov, Y. B. Vasilyev, P. S. Alekseev, A. P. Dmitriev, I. V. Gornyi, V. Y. Kachorovskii, M. Titov, B. N. Narozhny, and R. J. Haug, "Linear magnetoresistance in compensated graphene bilayer," *Phys. Rev. B* **93** (May, 2016) 195430.

[208] P. S. Alekseev, A. P. Dmitriev, I. V. Gornyi, V. Y. Kachorovskii, B. N. Narozhny, and M. Titov, "Counterflows in viscous electron-hole fluid," *Phys. Rev. B* **98** (Sep, 2018) 125111.

[209] B. N. Narozhny, I. V. Gornyi, and M. Titov, "Anti-poiseuille flow in neutral graphene," *Phys. Rev. B* **104** (Aug, 2021) 075443.

[210] P. S. Alekseev, "Negative magnetoresistance in viscous flow of two-dimensional electrons," *Phys. Rev. Lett.* **117** (Oct, 2016) 166601.

[211] P. S. Alekseev, A. P. Dmitriev, I. V. Gornyi, V. Y. Kachorovskii, B. N. Narozhny, and M. Titov, "Nonmonotonic magnetoresistance of a two-dimensional viscous electron-hole fluid in a confined geometry," *Phys. Rev. B* **97** (Feb, 2018) 085109.

[212] G. M. Gusev, A. S. Jaroshevich, A. D. Levin, Z. D. Kvon, and A. K. Bakarov, "Viscous magnetotransport and gurzhi effect in bilayer electron system," *Phys. Rev. B* **103** (Feb, 2021) 075303.

[213] T. Scaffidi, N. Nandi, B. Schmidt, A. P. Mackenzie, and J. E. Moore, "Hydrodynamic Electron Fow and Hall Viscosity," *Phys. Rev. Lett.* **118** (Jun, 2017) 226601.

[214] E. H. Hasdeo, J. Ekström, E. G. Idrisov, and T. L. Schmidt, "Electron hydrodynamics of two-dimensional anomalous hall materials," *Phys. Rev. B* **103** (Mar, 2021) 125106.

[215] L. Banszerus, M. Schmitz, S. Engels, J. Dauber, M. Oellers, F. Haupt, K. Watanabe, T. Taniguchi, B. Beschoten, and C. Stampfer, "Ultrahigh-mobility graphene devices from chemical vapor deposition on reusable copper," *Science Advances* **1** no. 6, (2015) e1500222.

[216] E. H. Hwang and S. Das Sarma, "Acoustic phonon scattering limited carrier mobility in two-dimensional extrinsic graphene," *Phys. Rev. B* **77** (Mar, 2008) 115449.

[217] S. Fratini and F. Guinea, "Substrate-limited electron dynamics in graphene," *Phys. Rev. B* **77** (May, 2008) 195415.

[218] D. L. Nika and A. A. Balandin, "Two-dimensional phonon transport in graphene," *Journal of Physics: Condensed Matter* **24** no. 23, (May, 2012) 233203.

[219] D. K. Efetov and P. Kim, "Controlling electron-phonon interactions in graphene at ultrahigh carrier densities," *Phys. Rev. Lett.* **105** (Dec, 2010) 256805.

[220] J. H. Seol, I. Jo, A. L. Moore, L. Lindsay, Z. H. Aitken, M. T. Pettes, X. Li, Z. Yao, R. Huang, D. Broido, N. Mingo, R. S. Ruoff, and L. Shi, "Two-dimensional phonon transport in supported graphene," *Science* **328** no. 5975, (2010) 213.

[221] A. Sedrakyan, A. Sinner, and K. Ziegler, "Deformation of a graphene sheet: Interaction of fermions with phonons," *Phys. Rev. B* **103** (May, 2021) L201104.

[222] X. Du, I. Skachko, and E. Y. Andrei, "Towards ballistic transport in graphene," *International Journal of Modern Physics B* **22** no. 25n26, (2008) 4579.

[223] X. Du, I. Skachko, A. Barker, and E. Y. Andrei, "Approaching ballistic transport in suspended graphene," *Nature Nanotechnology* **3** no. 8, (Aug, 2008) 491.